Neutral Strange Particle Production in Ultra-Relativistic Heavy Ion Collisions at $\sqrt{s_{NN}}$ = 130 GeV.

by

Matthew Allan Charles Lamont

A thesis submitted to
The University of Birmingham
for the degree of
DOCTOR OF PHILOSOPHY

School of Physics and Astronomy
Faculty of Science
The University of Birmingham
January 2002

Synopsis

The main aim of relativistic heavy ion collisions is to study nuclear matter under the extremes of high temperature and density. It is under these conditions, that it is believed that a phase transition to a deconfined state of quarks and gluons, known as the Quark-Gluon Plasma (QGP), may take place. The existence of this state cannot be determined directly, hence a number of key signatures of the existence of the state have been proposed which can be detected. One of these signatures is an enhancement of strange particles. This thesis represents the first measurement of the spectra of the singly strange K^0_S meson and the Λ and $\overline{\Lambda}$ hyperons in Au+Au collisions at $\sqrt{s_{NN}}$ = 130 GeV, at the Brookhaven National Lab, New York.

These particles, known collectively as V0s, are reconstructed from the daughter particles, whose paths are measured as they traverse the large Time Projection Chamber. This thesis describes the procedures required to obtain the corrected transverse momentum distributions for each particle species, which in turn can be used to obtain an average yield per event. The $\overline{\Lambda}$ /Λ ratio has been measured to be 0.736$\pm$0.008$\pm$0.023 which is an increase from $\sim$ 0.1 measured at lower energies. This means that the number of net baryons at mid-rapidity is much smaller than was measured previously. The inverse slopes of the particles were found to be consistent with a picture of radial flow built up in the collision, and this is dependent upon the centrality of the collision. The yields were found to grow linearly with multiplicity over the measured centrality ranges, which means that an observation of an onset of strangeness enhancement was not observed. The ratios of the yield of the strange particles to the multiplicity ($<\Lambda + \overline{\Lambda} + K^0_S> /h^-$ =0.183$\pm$0.002) was found to be lower than those measured at lower energies. Finally, the yield as a function of transverse momentum showed the interesting result that at high momenta, the baryon yield was greater than the meson yield.

Acknowledgments

I would like to begin by thanking Prof. John Nelson for giving me the opportunity to work in the Nuclear Physics Group at Birmingham, and the E.P.S.R.C for their monetary contributions. I am also indebted to John, whom along with Dr. Peter Jones, acted as my supervisor and provided great support during the last 3 years. Although the summers at BNL were often long and arduous, the trips to the batting cages and the surely World famous 'Thai Gourmet' made it almost worthwhile. I would especially like to thank Peter for his exhaustive reading of this thesis, which is a much better document as a result.

As always, there are too many people I should mention from within the STAR collaboration who have provided great help and assistance along the way. However, I would like to thank (in alphabetical order) : Aihong, Al, Boris, Bum, Chuck, Curtis, Duncan, Eric, Frank, Gene, Helen, Hui, Iwona, Javier, Jeff, Lee, Manuel and Tom.

Thanks must be also given at this point to the other members of the Nuclear Physics group, especially Nobby and Charles, two of life's entertainers (though in different ways). Special mention must go to Mr. Jim Campbell for keeping the NP system always up and running despite Robs (and others) best attempts to take it down. If only Jim was employed at RCF, this thesis may have been completed a lot sooner !! I also would like to thank the former RHI students, Ninja, Lee (again) and Rob, all of whom I have learned a great deal from.

I would like to thank all co-habitors of the E320 zoo (and even the basement) for their friendship over the last few years, and in order of age (and slackness of group), they are : John, Dave, Hazel, Bradley, Phil, Pete, Richard, Nick, Carlos and Saher and of course honorary group member Barry. Unfortunately, I know what most of you still have to go through, so make the most of your free time now (especially Phil !).

Outside of work, I would like to thank the people who have been stupid enough to share a house with me over the last few years, namely Fletch, Trapper, Kerridge, Mart, Mel, Nic, Paul, Andy, Tan, Martin, Patricia and and Ian. I apologise to you now if watching/listening to cricket in the early hours has disturbed you all. Special mention must go here to Ian, Bob, Dave, Pete, Gav, Helen and Nooby, as following the Boro will never be an easy task, but the pain is easier if we bear it together. I have also been lucky enough to play for a few cricket teams the last few years, but special mention must go to the boys from Skolars, who through toil, hard work, persistence and getting a few ringers in, have nearly won a trophy !! I am sure that our time will come.

Finally, I would like to say a big thank you to my family, who have supported me in all aspects throughout my work, and I owe them a great deal of gratitude.

Author's Contribution

The STAR experiment is situated at Brookhaven National Laboratory on Long Island, New York. It is a large collaboration, consisting of approximately 400 physicists. In such a large collaboration, it is not possible for one person to be involved in all the tasks that are required to run the experiment and analyse the data. In this section I will explain the tasks which I performed.

On the operational side of the experiment, I helped in testing the cabling of the TPC as well as performing shifts when the detector was taking data. These shifts also took the form of Quality Assurance, which involved checking the reconstructed data as it was being taken.

On the software side of the experiment, when I started I was part of a small Quality Assurance team which tested the reconstruction software on Monte Carlo data. This involved not only bug-testing the strangeness reconstruction code, but also the track reconstruction code and also consistency of results on different operating systems.

After the data had been taken in 2000, I became involved in the development, testing and running of the embedding framework. The embedding procedure is essential to the majority of the analyses performed in STAR, as it provides a means of determining the corrections that have to be applied to the data. As well as producing the majority of the MicroDSTs of the raw data, I produced all of the embedding for the strangeness working group.

With the K^0_S, Λ and $\overline{\Lambda}$ embedding, I was able to complete the analysis which is presented in this thesis. This took the form of tuning the geometrical cuts, and the application of the corrections obtained from the embedding to obtain the final transverse momentum spectra. The results presented in this thesis represent the first such measurements of the K^0_S, Λ and $\overline{\Lambda}$ in heavy ion collisions at $\sqrt{s_{NN}}$ = 130 GeV.

During my studentship I have attended regular collaboration meetings, giving presentations on my ongoing analysis at each one. I have also been afforded the opportunity to present this work at two major international conferences, the proceedings one of which will be published in the Journal of Physics G (and is presented in Appendix B).

Contents

List of Figures

List of Tables

Chapter 1

Introduction

It is now well established that nucleons are not themselves the fundamental building blocks of matter, but rather contain more elementary particles, known as quarks (q)[1]. It is believed that six quarks, the up (u), down (d), strange (s), charm (c), bottom (b) and top (t), and their corresponding anti-quarks ($\overline{u}$,$\overline{d}$,$\overline{s}$,$\overline{c}$,$\overline{b}$,$\overline{t}$), grouped into three generations, constitute the total number of quarks. Their known properties are outlined in Table 1.1 [2].

Name	Symbol	Mass (MeV)	Charge (e)	Quantum Number
Up	u	$1.5 \rightarrow 5$	$+\frac{2}{3}$	Isospin = $+\frac{1}{2}$
Down	d	$3 \rightarrow 9$	$-\frac{1}{3}$	Isospin = $-\frac{1}{2}$
Strange	s	$60 \rightarrow 170$	$-\frac{1}{3}$	Strangeness = -1
Charm	c	$1100 \rightarrow 1400$	$+\frac{2}{3}$	Charm = +1
Bottom	b	$4100 \rightarrow 4400$	$-\frac{1}{3}$	Bottom = -1
Top	t	$173\,800 \pm 5\,200$	$+\frac{2}{3}$	Top = +1

Table 1.1: The properties of the 6 known quarks

Quarks themselves are never seen in isolation, but always form strongly interacting particles, referred to as hadrons, which are either baryons (qqq) or mesons ($q\overline{q}$). Protons and neutrons, which make up all of the visible stable matter in the Universe, are examples of baryons. Their quark constituents are (uud) and (udd) respectively. An additional quantum number, not listed in Table 1.1, must be introduced to avoid the violation of the Pauli Exclusion Principle, which forbids two fermions from occu-

pying the same quantum state. The need for this is seen when examining particles such as the Δ^{++} (uuu), Δ^- (ddd) and Ω^- (sss). Each particle has a spin of $\frac{3\hbar}{2}$ which means that all three quarks must have parallel spin. This additional quantum number is known as 'colour charge' and it has three degrees of freedom, labelled red (r), green (g) and blue (b). In order to satisfy the Pauli Exclusion Principle in the cases of the Δ^{++}, Δ^- and Ω^-, each quark in the baryon must carry a different colour charge. However, as individual quarks have never been observed in nature, it is postulated that the colour charge itself is confined, and hence all baryons and mesons must be colourless objects. In order for a meson to be colourless therefore, the anti-quark must carry anti 'colour charge', which are labelled $\overline{r}$, $\overline{g}$ and $\overline{b}$.

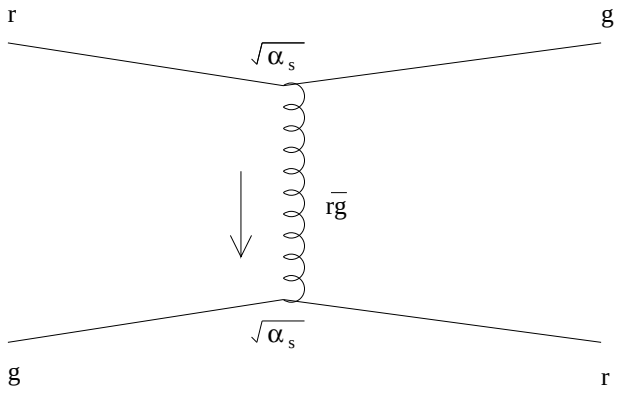

Figure 1.1: Single gluon exchange between a quark with red colour charge and a quark with $green$ colour charge

Gluons are the gauge bosons of the strong interaction which means that quarks interact with each other via the exchange of a gluon, as shown in Figure 1.1. In order for quarks with different colour charges to interact, the gluon must also possess colour charge. To facilitate the total number of possible coloured quark interactions, there must be eight different forms of gluons. Gluons are the QCD analogue of the photon in QED, but unlike photons, which do not carry electric charge, since gluons carry colour, they can self-interact. It is this possibility of gluon self interaction which is ultimately thought to be responsible for quark confinement.

1.1 Quark Confinement

The potential between two quarks may be written as :

$$V(r) = -\frac{4\alpha_s}{3\mathrm{r}} + \mathrm{kr} \tag{1.1}$$

where α_s is the strong coupling constant, k is a constant ($\sim$ 1 GeV/fm) and r is the separation of the quarks [3]. The $\frac{1}{\mathrm{r}}$ term determines the potential at short distances, where the gluon distribution from a quark is radial, as shown in Figure 1.2a. At large separations (r $\geq$ 1 fm), the self coupling of gluons causes the colour field lines between the quarks to form a tube (Figure 1.2b). Therefore, the potential at large distances increases linearly with the separation of the quarks as the density of field lines remains constant. This gives rise to the term linear in r in equation (1.1).

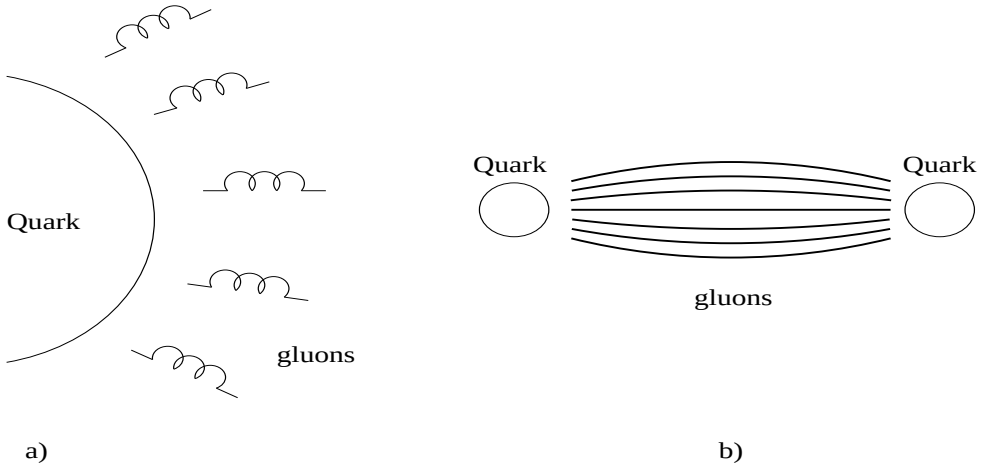

Figure 1.2: The gluon distribution from a quark. a) Near the quark, they form a radial distribution. b) Further from the quark, they form a flux tube.

One implication of equation (1.1) is that an infinite amount of energy is required to separate two colour charges. However, in practice, if the colour flux tube is stretched enough, it becomes energetically favourable to rupture the tube and terminate the field lines with a $q\overline{q}$ pair created out of the QCD vacuum. This therefore means that it is not possible to separate two quarks on a large distance scale.

Equation (1.1) also implies, however, that on the small distance scale which is governed by the term proportional to $\frac{1}{\mathrm{r}}$, deconfinement is possible if α_s tends to 0 faster than r.

1.2 Short Distance Behaviour

There are two phenomena which can lead to quark deconfinement at short distance scales. At very high energies, the bare quark itself can be probed and it is found that its effective colour charge tends to zero as the energy with which it is probed increases. This process is called Asymptotic Freedom. At high hadronic density, quarks can interact with quarks from other hadrons. In this process, they lose their 'memory' as to which hadron they are associated with. This is known as Debye Screening.

1.2.1 Asymptotic Freedom

As the separation of the quarks, r, tends to zero, so does the value of the strong coupling constant, α_s, which in turn leads to a reduction in the potential, given by equation (1.1). This process of the reduction in the force is known as asymptotic freedom. In order to understand this, it is instructive to review the well-known process of vacuum polarisation in QED.

In QED, it is known that an electron constantly emits and re-absorbs virtual photons, which in turn may produce a virtual e^+e^- pair, by borrowing the required energy from the vacuum as allowed by the Heisenberg Uncertainty Principle. This virtual e^+e^- pair (which can live for time $\Delta t \sim \frac{\hbar}{m_e c^2}$) will be polarised by the E-field of the original e^- in such a way that the virtual e^+ is closer to the original electron than the virtual e^-. In this way, it is possible to think of the vacuum as a dielectric medium, which has the effect of reducing the magnitude of the electric field in the vicinity of the original electron. Therefore, as a test charge moves closer to the original electron, the value of the electric charge of the electron it sees increases, until at very small distances, it reaches the full value of the bare charge.

The probability of interaction of electrons is governed by the electro-magnetic coupling constant, α_{em}, which is defined in equation (1.2),

$$\alpha_{em} = \frac{q_1 q_2}{4\pi\epsilon_0\hbar c} \tag{1.2}$$

where q_1 and q_2 represent the charge on the electrons. Rather than discussing the distance dependence of the charge, it is more usual to discuss the distance depen-

dence of α_{em}, which is described in equation (1.3),

$$\alpha_{em}(Q^2) = \frac{\alpha_{em}}{[1 - (\frac{\alpha_{em}}{3\pi} ln(\frac{Q^2}{m_e^2}))]} \tag{1.3}$$

which is valid for $Q^2 \gg m_e^2$, where $Q^2 = -q^2$ (q is the momentum transfer and is inversely proportional to r) and m_e is the mass of the electron. Therefore the more momentum transferred in the process, the closer the test charge is to the electron, the larger the value of α_{em} becomes, which leads to q_1 and q_2 being closer to the bare electron charge, as seen in equation (1.2). Note that for small values of Q^2 which correspond to a large separation of the charges, then $\alpha_{em}(Q^2)$ is just equal to α_{em}, and the electron's charge is equal to the measured value of e.

An analogous process occurs in QCD, where gluons create virtual $q\overline{q}$ pairs which reduce the value of the colour charge of the quark at large distances. As gluons themselves possess a colour charge however, it was found that they can additionally form gluon-loops which have an anti-screening effect as they carry colour charge away from the quark [4] [5], as depicted in Figure 1.3. Crucially therefore, the closer the source of the colour charge is probed, the less the effective colour charge on the quark.

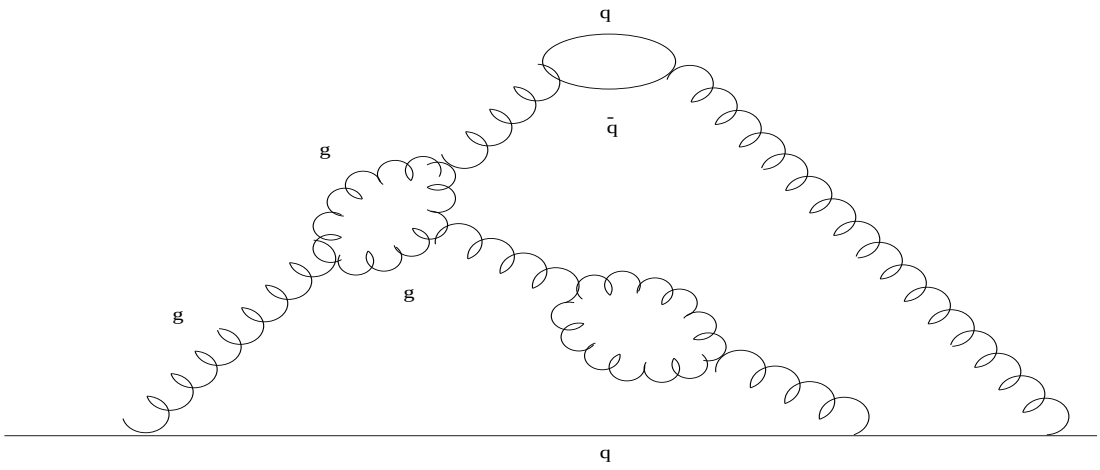

Figure 1.3: Vacuum polarisation in QCD: a contribution including triple-gluon coupling, taken from [6].

The strong coupling constant, which describes the probability of an interaction between a quark and a gluon, is given in equation (1.4),

$$\alpha_s(Q^2) = \frac{12\pi}{(33 - 2n_f)\ln(Q^2/\Lambda^2_{QCD})} \tag{1.4}$$

where n_f is the number of quark flavours and again Q^2 is the square of the momentum transfer, and is only valid for $Q^2 \gg \Lambda^2_{QCD}$. In equation (1.4), the 33 term is determined by the gluon contribution and the n_f term is due to the quark loops. The value of Λ_{QCD} has been determined experimentally to be ~ 200 MeV [7]. At small distances (high Q^2), $\alpha_s(Q^2) \to 0$ more quickly than $r \to 0$, so the interaction potential, given in equation (1.1), also tends to 0 and the quarks and gluons can be thought to be free particles. This behaviour of α_s with Q^2 leads to it being called the $running\ coupling\ constant$, and its dependence on Q^2 has been experimentally determined in the DELPHI experiment at the LEP accelerator at CERN [8].

The Λ_{QCD} variable can be said to represent the scale of the strong interaction, as its value differentiates between a world of confined hadrons ($Q^2 \sim \Lambda^2_{QCD}$) and that of free quarks and gluons ($Q^2 >> \Lambda^2_{QCD}$) and it was this process of asymptotic freedom which first led to the notion that a QGP may exist [9].

1.2.2 Debye Screening

The process of Debye screening occurs at high hadronic densities and is a bulk phenomena. This happens when hadrons are close enough to each other that their 'boundaries' overlap ($r \leq 1$ fm), so that quarks from one hadron can interact with quarks from another hadron, as indicated in Figure 1.4 (taken from [10]). When the hadronic density is large enough, a transition will occur where a quark can interact with quarks in other hadrons so that it will have lost its 'memory' as to which hadron it is associated with and it will be able to propagate freely throughout a volume of deconfined quark and gluon matter.

This method of deconfinement is not peculiar to QCD, it is just a bulk phenomenon. Another example of this is the Mott transition in condensed matter, which governs the transition between an insulator and a metal under compression. In an insulator, the Coulomb force binds electrons to nuclei. The potential here is given by equation (1.5),

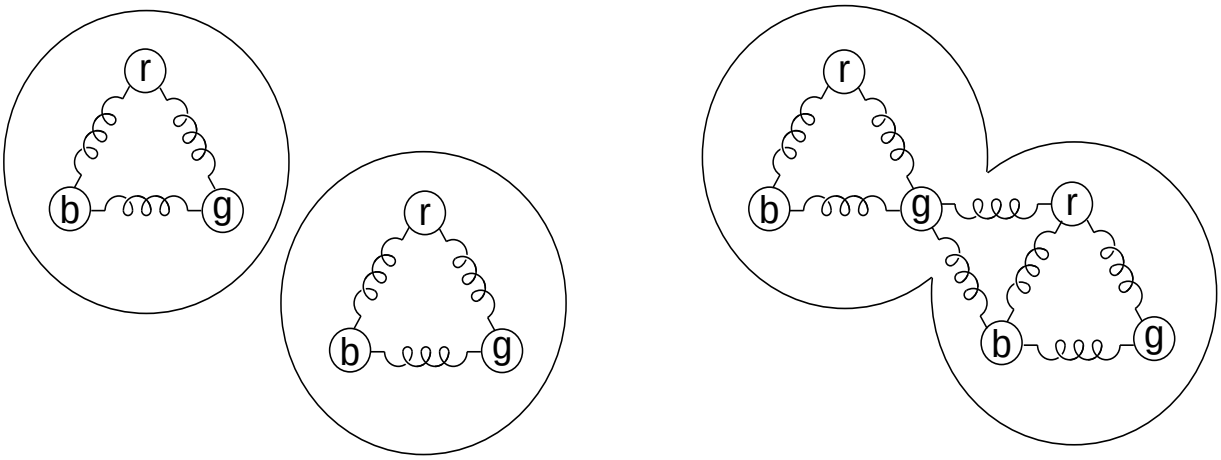

Figure 1.4: Colourless hadrons (left) and dense matter (right) where hadrons overlap and quarks can interact with quarks from other hadrons.

$$V_i(r) = \frac{-\mathrm{Ze}^2}{4r\pi\epsilon_0} \tag{1.5}$$

where -e is the electron charge and +Ze is the charge of the nucleus. As the density is increased, this potential is modified due to the proximity of the neighbouring nuclei, and becomes equation (1.6),

$$V_m(r) = V_i(r).exp(\frac{-r}{R_D}) \tag{1.6}$$

where R_D is the Debye radius and is given by $R_D \sim \frac{1}{\sqrt[3]{\text{charge density}}}$. As the Debye radius becomes smaller than the binding radius, r, electrons become unbound and can move freely throughout the volume. By analogy, the situation in QCD can be thought of as the transition between a colour insulator (hadron degrees of freedom) and a colour conductor (quark and gluon degrees of freedom).

Due to the high energies required for asymptotic freedom to occur, ($Q^2 \gg 10^{26}$ GeV [11]), in heavy ion collisions at relativistic energies in the laboratory, it is hoped that deconfinement can be achieved through the bulk process of Debye screening.

1.3 Estimates of the Critical Parameters

The phase diagram of nuclear matter is shown in Figure 1.5, which plots temperature against net baryon density. The regions shown depict the three possible states : hadronic matter, deconfined matter and a mixed phase. The numbers on the axes are estimates of the parameters.

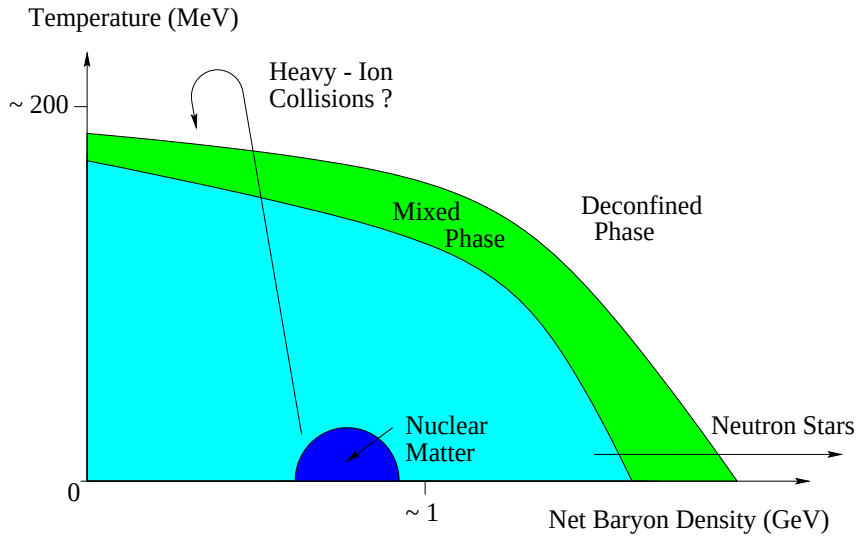

Figure 1.5: The Phase diagram of nuclear matter, plotting the net baryon density (μ_B) against Temperature.

In order to estimate the critical transition temperature, non-perturbative QCD simulations based upon a discrete lattice of Euclidean geometry in four dimensions (3 space and 1 time) can be used [12]. Quarks are placed on each lattice point, with gluons connecting them, and interactions between the quarks are simulated computationally. The lattice spacing represents the separation of quarks, and it has been shown that as the spacing is reduced, the value of α_s decreases, as is expected theoretically. Although Lattice QCD calculations are currently limited by the size and performance of the supercomputers used, results from simulations in the zero net baryon density domain yield results for two light quarks of $\sim$ 150 MeV and $\sim$ 175 MeV for three light quarks [13]. These numbers compare with previous calculations, for the non-physical case of infinite quark masses (so that the gluons were the only degrees of freedom) which predict temperatures of $\sim$ 270 MeV [14]. The energy density can also be calculated from Lattice QCD calculations. Figure 1.6 (taken

from [15]) shows how the energy density behaves as a function of temperature in three systems, for two light quark flavours (2 flavour), two light and one heavy quark flavour (2+1 flavour) and three light quark flavours (3 flavour). The value of the critical energy density required for a phase transition, (ϵ_c), can be extracted from this data and is $\sim$ 0.7 GeV/fm^3, though this has an error of $\sim$ 50 $\%$.

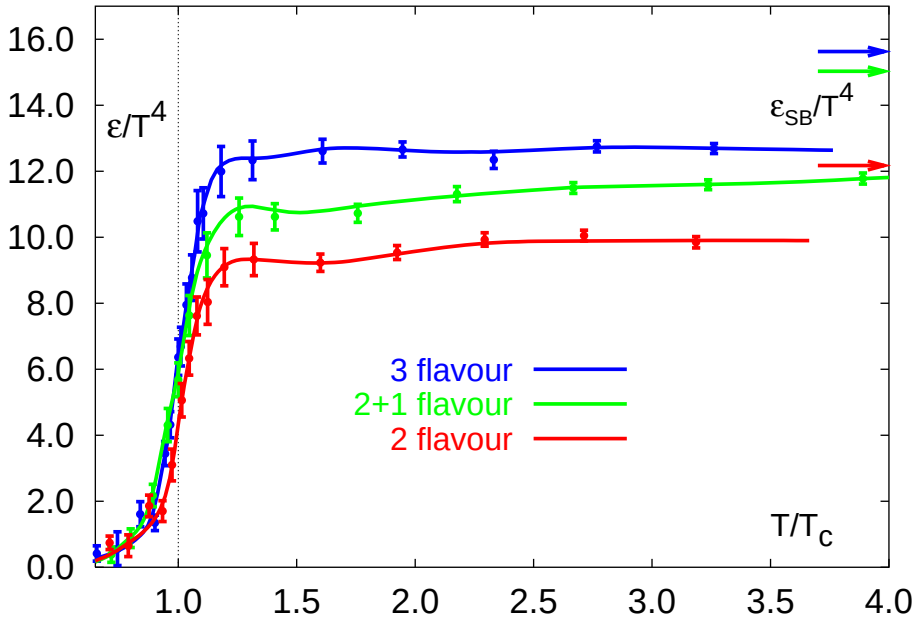

Figure 1.6: The energy density in QCD as a function of temperature (where T_c is the critical temperature). ϵ_{SB}/T^4 represents the Stefan-Boltzmann limit of an ideal gas.

Lattice QCD calculations can also determine the order of the phase transition. Calculations show that this order of the phase transition is dependent on the mass of the quarks in the calculations [16] [17]. For infinite masses, calculations involving only 2 quark flavours (u,d) indicate a first order phase transition, which changes to second order as the masses are reduced. This then returns to being a first order transition for realistic values of the quark masses and when 3 quark flavours (u,d,s) are used in the calculation. A first order phase transition is indicated by a mixed phase, as in the liquid-gas phase transition, while a second order transition (or continuous transition) doesn't have this mixed phase. An example of a continuous transition is that when a paramagnet becomes a ferromagnet as the temperature is reduced.

The critical energy density can also be calculated in phenomenological models from the equation of state, which gives the relationship between the temperature of

the system and the energy density. In the simplified case of a system of massless non-interacting light quarks (i.e. up and down quarks only and α_s = 0), using as a basis the MIT Bag model of a hadron [18], the critical energy density (ϵ_c) is shown to be given by equation (1.7) [19] :

$$\epsilon = (\frac{\mathrm{T}}{160\mathrm{MeV}})^4 (GeV/fm^3) \tag{1.7}$$

where T (in units of MeV) is the temperature of the system. Substituting these temperatures obtained from Lattice QCD into Equation (1.7) leads to critical energy densities for a hadron to parton phase transition of between 0.77 GeV/fm^3 and 1.43 GeV/fm^3 for the two flavour and three flavour cases respectively, which are consistent with the results from Lattice QCD. This has to be compared to normal nuclear matter density (ϵ_{nuc} = 0.125 GeV/fm^3) and the energy density in a hadron ($\epsilon_{had} \sim$ 0.300 GeV/fm^3) [19]. Therefore, these simplified calculations suggest that the density required to form a Quark-Gluon Plasma must be at least twice normal hadronic densities.

1.4 Chiral Symmetry Restoration

It is also predicted that at temperatures approximately the same as those required for a deconfinement transition, a transition into a chirally symmetric phase can occur [20]. Chiral symmetry is related to the helicity of quarks. Quarks whose spin vectors are aligned to their momentum vector are said to be $right\ handed$, while quarks whose spin vectors are anti-parallel to the momentum vectors are referred to as being $left\ handed$. In any interaction with massless particles, the helicity of the particles is conserved exactly.

At temperatures below this transition, quarks are massive particles. As α_s is greater than zero, quarks can interact and these interactions have the effect of increasing their mass so that it is greater than the bare (or $current$) masses listed in Table 1.1. This is known as their $dynamical$ mass and can be calculated intuitively from the hadronic masses. This leads to light quark (u and d) masses of approximately 300 MeV, and a strange quark (s) mass of approximately 500 MeV [21]. It is then easy to see why chiral symmetry is broken at these lower temperatures. As a quark with mass cannot travel at the speed of light, it is always possible to transform

to a frame of reference where, in the case of a right handed particle, the momentum vector is no longer aligned to the spin vector, but anti-parallel to it. This situation, where a quark may appear to be either $left\ handed$ or $right\ handed$ depending on the frame of reference, clearly breaks chiral symmetry.

At temperatures above this phase transition, α_s tends to zero and the interactions between quarks are minimized. Therefore, their effective mass is no longer given by their $dynamical\ mass$, but by their $current\ mass$ value. As these values are still greater than zero[1], chiral symmetry can not be restored completely, but only partially.

The manifestation of a restoration of chiral symmetry in relativistic heavy ion collisions, where quark masses are given by their $current$ value, rather than their $dynamical$ value, may be two-fold. Firstly, the hadronic masses may be lower than expected, which could be visible in the lowering and broadening of resonance masses. Secondly, an increase in production rates of the heavier quarks may be seen. This should be most notable for the strange quark as the temperature of the system becomes comparable to the mass of the $s\overline{s}$ pair.

[1]There is ongoing work to determine whether the up quark is massless, for examples see [22] and [23]

Chapter 2

Relativistic Heavy Ion Collisions

As Asymptotic Freedom only occurs in processes involving very high energies and momentum transfer ($Q^2 \gg 10^{26}$ GeV), it is through the process of Debye screening that it is hoped a dense system of freely interacting quarks and gluons can be created in the laboratory, by colliding heavy ions at relativistic energies.

2.1 Experimental Programs

There are currently many ongoing experiments at three major experimental facilities. These are the Alternating Gradient Synchrotron (AGS) and Relativistic Heavy Ion Collider (RHIC) at Brookhaven National Laboratory, New York, and the Super Proton Synchrotron (SPS) at the European Centre for Nuclear Research (CERN), Switzerland. The experimental programs at the AGS and SPS started in the mid 1980s and operate in fixed target mode, with one heavy ion beam impinging upon a stationary target. The RHIC has just completed its first 'year' of operation and is different to the AGS and SPS in that it is a collider, which means that there are two heavy ion beams accelerated in two concentric rings. The advantage of this method is that higher centre of mass (COM) energies can be achieved. The main features of the different accelerators are given in Table 2.1, which outlines the systems and energies of data referred to in this thesis.

Accelerator	System	Beam Energy (GeV/A)	COM Energy (GeV/A)	Beam Rapidity
AGS	Au+Au	2	2.43	1.50
AGS	Au+Au	4	3.08	2.16
AGS	Au+Au	6	3.63	2.55
AGS	Au+Au	8	4.10	2.84
AGS	Au+Au	10	4.54	3.06
AGS	Au+Au	10.8	4.70	3.14
AGS	Au+Au	11.6	4.86	3.21
SPS	S+S	200	19.41	6.06
SPS	Pb+Pb	40	8.76	4.45
SPS	Pb+Pb	80	12.32	5.14
SPS	Pb+Pb	158	17.27	5.82
RHIC	Au+Au	65	130	$\pm$ 4.93
RHIC	Au+Au	100	200	$\pm$ 5.36

Table 2.1: The main features of the different accelerators used in relativistic heavy ion physics

2.2 The Space-Time Evolution of the Collision

If the temperature and density of the system are large enough, it is believed that the matter created in these collisions could undergo a phase transition to a new, deconfined phase, known as a Quark-Gluon Plasma (QGP). If this is so, it will only last a short time before the system expands, cools and re-hadronises. The different stages of the collision are illustrated in Figure 2.1.

The process is started when the heavy-ion beams collide and a fireball is formed. During this initial stage, many quarks and gluons (known collectively as partons) are created in the collision volume due to inelastic collisions of the original partons. These 'secondary' partons then go on to interact themselves. This is the pre-equilibrium stage, where the relevant degrees of freedom are partonic. As the system of partons becomes more dense, the process of Debye screening means $q\overline{q}$ pairs are created easily due to the high temperatures. When this partonic fireball reaches equilibrium, it is known as a Quark-Gluon Plasma. As the fireball expands due to the internal pressures, it cools down and the system then crosses the phase bound-

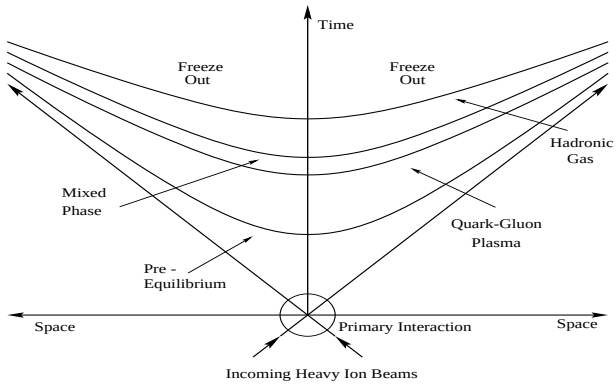

Figure 2.1: The space-time evolution of a heavy-ion collision, which undergoes a phase transition to a QGP.

ary whereupon the partons hadronise. If the crossover of the phase boundary represents a first order phase transition, then there will be a a phase where a mixture of partons and hadrons co-exist. As the system expands and cools, there will come a point when there is no longer enough energy for inelastic collisions to occur. At this time, the distribution of particles amongst the various hadronic states is frozen and there are no flavour changing reactions. This is known as chemical freeze-out, and the temperature denoted by T^{ch}. The system will then expand even further until it is cool enough so that elastic collisions between particles can no longer occur and the particles' momenta are then fixed. The temperature at this stage then represents thermal freeze-out, T^{th}. In general, unless the expansion is rapid, T^{th} is lower than T^{ch}.

2.3 Experimental Determination of the Critical Parameters

In order to determine whether the critical conditions indicated in section 1.3 are met in these collisions, a model has to be used as the energy density can not be measured directly. These models have to make use of variables which are measurable in the collision, the useful variables are defined in Appendix A.

The calculated energy density (ϵ) of the collision depends on the amount of nuclear stopping in the collision. Full stopping is achieved by multiple collisions of the

colliding nucleons, so that they come to rest in the COM reference frame. In the Bjorken scenario [24], the initial nuclei pass through each other so that there is no stopping, which means that after the initial collisions between the projectile partons, they pass through each other and have travelled far enough away so that they cannot undergo any secondary interactions. In its most extreme case, this relates to a deconfined phase with a zero net baryon density, and the fireball is said to be $baryon\ free$. In this scenario, the energy density can be calculated using equation (2.1) [25], which calculates the energy density using the transverse energy per unit pseudo-rapidity ($dE_T/d\eta$), an experimentally determinable quantity[1]. The other factors in equation (2.1) are R, the radius of the participating volume ($1.12\ A^{1/3}$), and τ, the time at which a QGP may have been formed. The value of τ cannot be determined experimentally, though in the literature it is generally assumed to be τ = 1 fm/c (for example, see [25]).

$$\epsilon = \frac{dE_T}{d\eta}\frac{1}{\pi R^2 \tau} \tag{2.1}$$

In contrast to the Bjorken scenario, the Landau model of relativistic heavy ion collisions assumes that there is total stopping in the collision [26]. In this scenario, the initial nucleons have less energy and have secondary and tertiary interactions until they are all stopped in the centre of mass reference frame. This scenario is said to produce a $baryon\ rich$ plasma, as all of the initial baryons are concentrated at mid-rapidity.

The energy density of the ion at rest is given by $\epsilon_0 = E/V$ = 0.125 GeV/fm^3, where E is the energy and V is the volume. As the ion moves relativistically, the energy becomes $E' \simeq E\gamma$ and the volume $V' = V/\gamma$, where γ is the relativistic factor equal to $1/\sqrt{1 - \frac{v^2}{c^2}}$.

As the two ions are completely stopped, they occupy the same physical space, so the critical energy density in the Landau model is given by equation (2.2), which is an upper limit estimate as in reality, the value of γ changes as the ions are brought to rest in the COM reference frame.

[1]Note that equation (2.1) differs with that in the original paper by a factor of 2. The author believes that this is due to a mistake in the original paper

$$\epsilon = 2\gamma^2 \epsilon_0 \tag{2.2}$$

The Bjorken and Landau estimates of the energy density are for very different scenarios, so it is necessary to look at experimental data to determine which one is closer to describing what is happening in the laboratory.

2.3.1 Experimental Determination of Baryon Stopping

A very useful tool for determining the conditions in a RHI collision is the rapidity spectrum (dN/dy as a function of y) of protons, which gives information on the distribution of the protons in momentum space. As protons are contained in the incoming nuclei, initially they are concentrated at the beam and target rapidities. Where these protons then end up determines how much stopping occurs in the collision. In the Landau scenario, the proton rapidity distribution is centred at mid-rapidity, whereas in the Bjorken scenario the proton rapidity distribution is centred at approximately the beam rapidities.

Experiment E802 report that at the top AGS beam energy (11.6 GeV/A) the dN/dy spectra of protons show a greater enhancement at mid-rapidity as a function of increasing collision centrality (decreasing impact parameter), where the centrality is determined experimentally by the measured multiplicity [27]. This is confirmed by experiment E917 for a range of beam energies (6, 8 and 10.8 GeV/A) and centralities [28]. They fit their data with two identical Gaussian distributions centred at equal distances from mid-rapidity, as shown in Figure 2.2. Although the centroids of the two Gaussian functions move in towards mid-rapidity as the collision centrality is increased, even for the most central bin, they are not centred at mid-rapidity. This is interpreted as an indication that at the AGS energies there was substantial stopping, though full stopping is not achieved.

The NA35 collaboration have reported a measurement of the proton rapidity distribution for both peripheral and central collisions in the S+S system at the SPS ($\sqrt{s_{NN}}$ = 19.41 GeV) [29], where the term central collisions is used to describe ion-ion collisions with a small impact parameter, and peripheral collisions refers to large impact parameters, as shown in Figure 2.3. Due to the larger number of interacting particles, and hence the greater the size of the system, it is in the most central col-

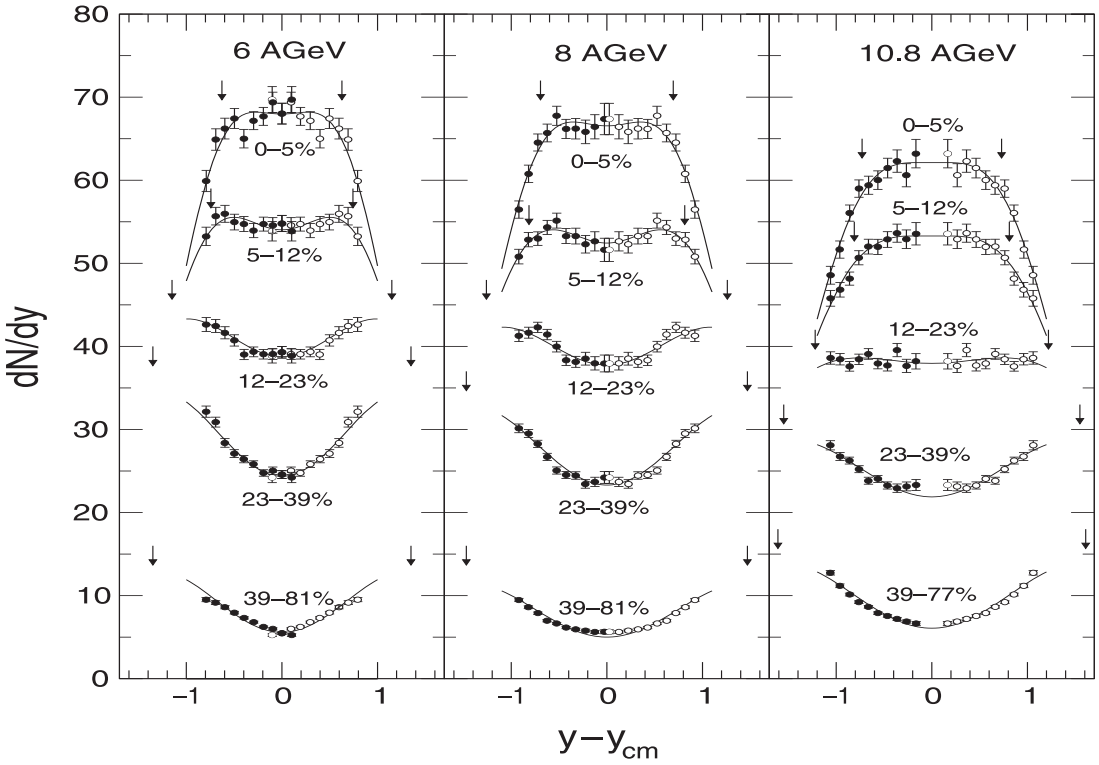

Figure 2.2: Centrality dependence of dN/dy distributions for protons at three different energies, where the centrality is defined as the most central x% of the total hadronic cross-section. Full circles represent measured data, open circles are data reflected about mid-rapidity. Lines represent double Gaussian fits to data, centred at the arrows. Plot taken from [28].

lisions that a QGP could be formed. The most peripheral collisions have an impact parameter which is just smaller than the nuclear radius, and at this extreme, behave as p+p collisions, which explains why the proton spectra peak strongly in the beam rapidity region in [29]. For the central collisions, the proton rapidity distribution is flat, and enhanced relative to the peripheral data. As expected due to the higher energies involved, this indicates that significant but not complete stopping occurs.

The NA49 collaboration have made a measurement of the net proton and net baryon rapidity distributions in the 3% most central Pb+Pb collisions at the SPS ($\sqrt{s_{NN}}$ = 17.27 GeV), shown in Figure 2.4 [30]. These distributions take out the contribution from produced protons and baryons and their shapes compare very well

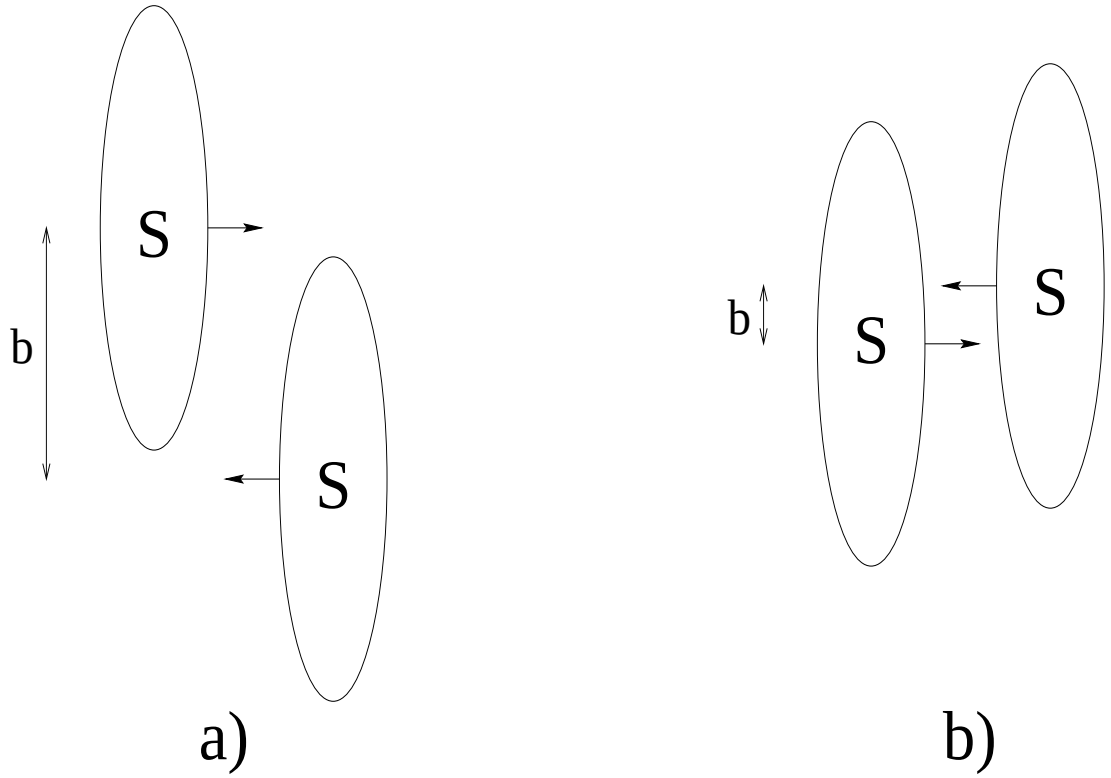

Figure 2.3: A schematic representation of a S+S collision in the centre of mass reference frame: a) A peripheral collision with a large impact parameter (b), b) A central collision with a small impact parameter.

with the top 5% most central S+S collision ($\sqrt{s_{NN}}$ = 19.41 GeV), where the data is scaled by the number of participants to facilitate a fair comparison. The net baryon distribution in Pb+Pb is narrower than that of the S+S system, which indicates a larger degree of stopping in the larger system.

From proton rapidity spectra, it appears that as expected, more stopping occurs in the lower energies at the AGS compared to the SPS. At the SPS energies, the spectra in Figure 2.4 show that the data is closer to the Bjorken stopping scenario than it is to the Landau scenario, though the Bjorken scenario still cannot explain the data exactly.

The energy density has been calculated by the NA49 collaboration for the system sizes and energies measured at the SPS, using a measured value of $dE_T/d\eta$ and substituting this into the Bjorken model (equation (2.1)). The values for the most central collisions are given in Table 2.2.

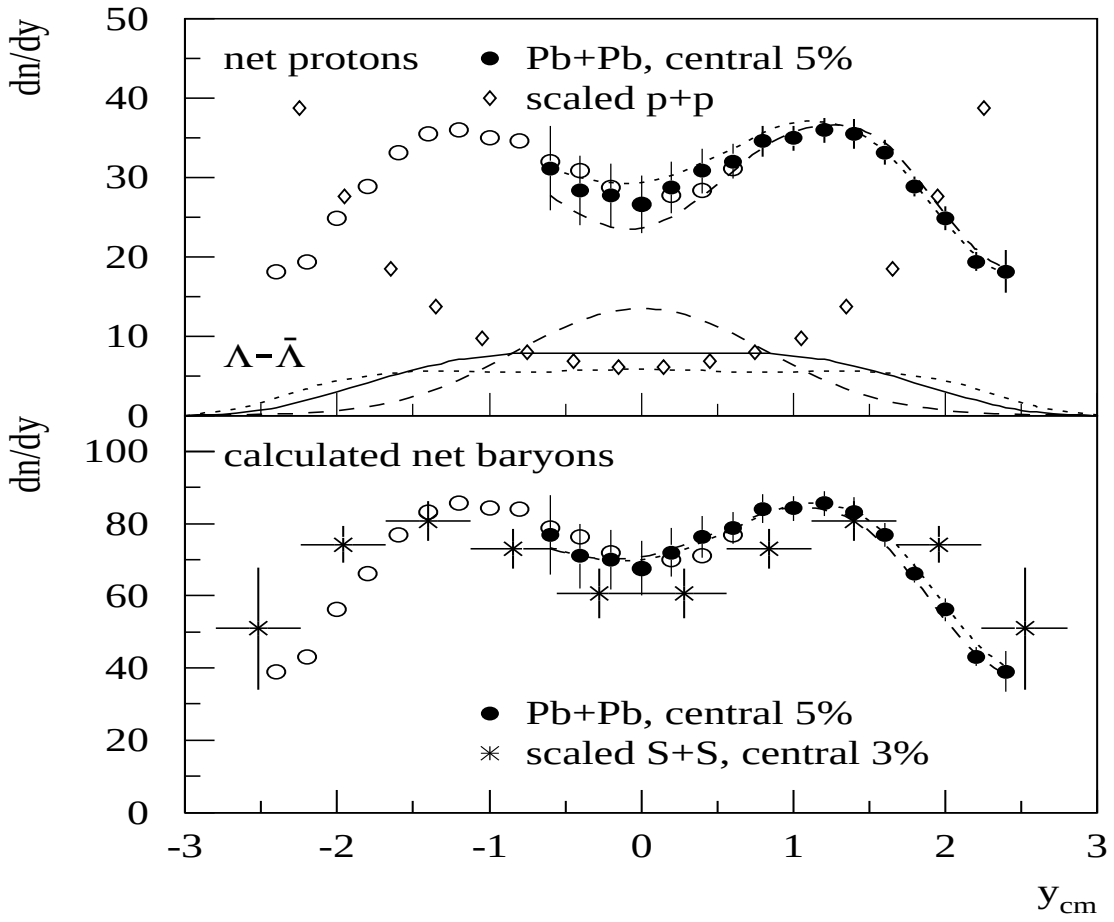

Figure 2.4: The upper plot shows net proton distribution for Pb+Pb collisions and scaled p+p collisions. The lower plot compares the net baryon distribution for Pb+Pb and scaled S+S collisions. The filled circles are measured points and the open circles represent the measured points reflected about mid-rapidity. Plot taken from [30]

Apart from the assumption that no stopping has taken place, there are also other caveats in these calculated values. The first problem is that the value of $dE_T/d\eta$ is measured in an hadronic and electro-magnetic calorimeter, which does not distinguish between primary and secondary particles (for instance weak decays of Λ ($\Lambda \rightarrow p\pi^-$)). Secondly, an assumption has had to be made for the value of τ, which was chosen to be 1 fm/c. Although this value is consistent with the rest of the literature, it may lead to an incorrect calculation of ϵ.

If the assumption is made that the two caveats do not bring much uncertainty to the calculation, then all of the values obtained in Table 2.2 using the Bjorken model,

Accelerator	System	Energy Density (GeV/fm^3)
SPS	S+S	1.3
SPS	S+Au	2.6
SPS	Pb+Pb	3.2

Table 2.2: The calculated energy densities achieved in relativistic heavy ion collisions at the SPS [25]

exceed the critical energy density ($\epsilon_c \sim 0.7$ GeV/fm^3)for a parton - hadron phase transition calculated in section 1.3. However, a fit to the SPS data which uses a 3 dimensional expansion scenario, as opposed to the Bjorken method which is only performed in 1 dimension, gives a much lower value of the energy density achieved, ϵ_{3D} $\simeq 0.6$ GeV/fm^3. This value is below the critical energy density for a phase transition.

As the COM energies increase by a factor of ~ 10 in going to RHIC from the SPS, the stopping should be closer to the Bjorken scenario if the trend from AGS to SPS energies continues. The energy densities involved should also increase, so that they are greater than the calculated critical value.

2.3.2 Extracting the Kinetic Freeze-out Temperature

It was shown by Hagedorn [31] that the temperature of the system at kinetic freeze-out can be extracted from the transverse momentum spectra using equation (2.3), where T corresponds to the temperature at thermal freeze out and m_t is the transverse mass.

$$\frac{1}{m_t}\frac{d^2n}{dm_t d\mathbf{y}} \propto \sqrt{m_t}e^{-m_t/T} \tag{2.3}$$

This temperature is usually referred to as the inverse slope parameter, in reference to equation (2.3), as it is affected by the presence of collective transverse flow within the fireball. In a hydro-dynamical model, flow develops because of pressure gradients which are generated in the nuclear medium, and hence it doesn't reflect the true freeze-out temperature of each particle species. This is illustrated in Figure 2.5 (taken from [32]) which shows the masses of various particles along with their corresponding slope parameter, for data taken at the SPS.

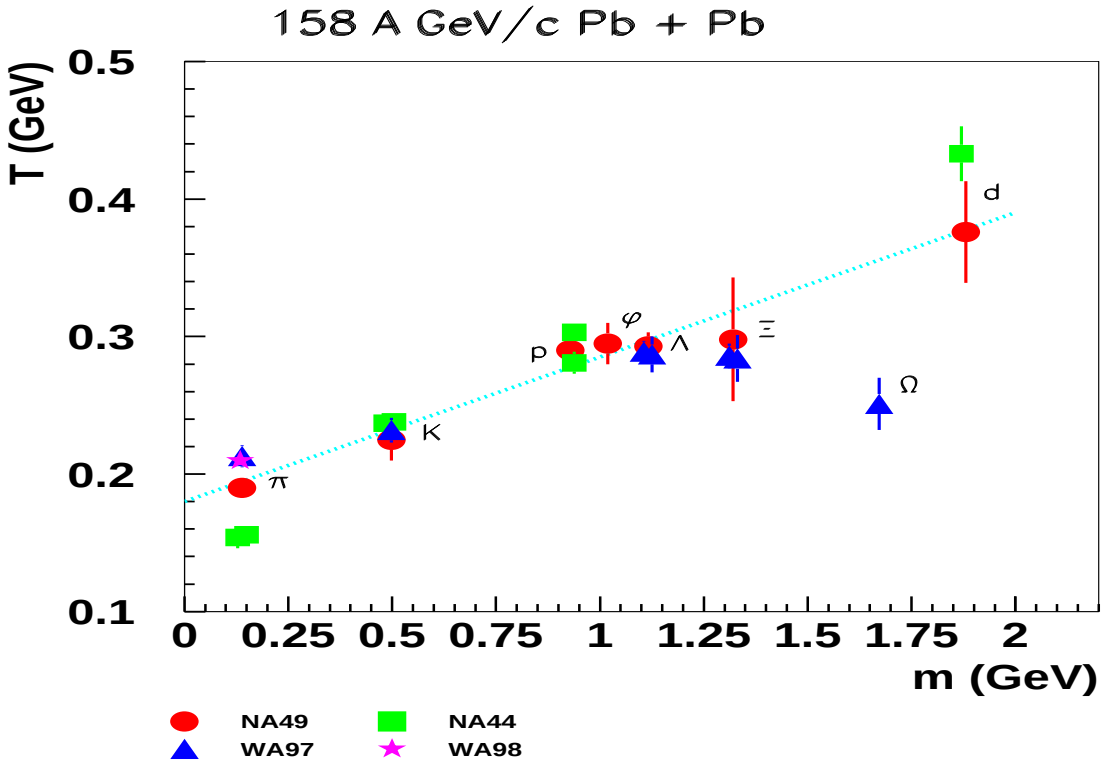

Figure 2.5: Mass dependence of the slope parameters of various particles at thermal freeze-out

The behaviour shown in Figure 2.5 can be explained by the notion that if the fireball is expanding with a certain velocity, and all particles freeze-out at approximately the same temperature, then the slope parameter should increase with the mass of the particle. Therefore, the temperature at thermal freeze out can be obtained by extrapolating to zero mass assuming the parameterisation given in equation (2.4), where T_{fo} is the thermal freeze-out temperature of the fireball, v_T is the mean transverse velocity of the particles in the fireball and m_i is the mass of particle i [33].

$$T = T_{fo} + \frac{v_T^2 . m_i}{2} \tag{2.4}$$

All particles appear to fit a line of constant freeze-out (as shown in Figure 2.5) with one notable exception to this behaviour, the Ω multi-strange baryon. Its slope parameter is much less than the overall trend would suggest and it is believed that Ω's freeze out much earlier than other particles due to their small scattering cross section with other hadrons [34] and hence lack of available resonances with most

notably the pions, which are the most abundant produced particles in the fireball.

It could also be said that the slope obtained for the Ξ^- in Figure 2.5 is also below the shown line, and there are multiple measurements of the pion inverse slope which differ from each other. This is indicative of the general problem which exists when identifying the inverse slope of the pions, as they are dominated by secondary pions from resonance decays. Therefore, depending upon the p_t ranges used, the acceptances for the secondary pions differ which can alter the value of the inverse slope, which can only be a local value. This means therefore that care must be used when using the inverse slopes to extract a common freeze-out temperature.

Chapter 3

Quark Gluon Plasma Signatures

As the deconfined QGP phase is very short-lived, it is impossible to detect directly. Therefore, in order to infer whether the phase transition occurred, the measurement of a quantity that is peculiar to the QGP phase and survives the hadronisation process, is required. Initially, comparing to lattice QCD predictions (e.g. Figure 1.6) it seems intuitive to measure global observables, such as energy density, as a function of temperature. This has problems, however, in that a calculation of the energy density is model dependent, and if the phase transition is continuous rather than first order, then the energy density will increase linearly with increasing temperature in the transition region. In order to avoid these problems, local observables are used to search for a deconfined state of matter. These take the form of electromagnetic probes, which are created throughout the collision and have a large mean free path so that they escape the fireball region before they re-interact, charmonium suppression, where the large densities in the plasma cause weakly bound charmonium states to become unbound, and strangeness enhancement, where the large densities and temperatures in the plasma make it easier to produce strange quarks than a system with only hadronic degrees of freedom.

3.1 Electromagnetic Probes

3.1.1 Direct Photons

Photons are a useful probe of the thermodynamics of the fireball as they only interact electro-magnetically and have a large mean free path compared to the size of the

fireball. However, photons are produced by different interactions throughout the evolution of the fireball. they are produced in the initial hard scattering and in the final hadronic stage, as well as in the QGP phase, and the photons from the QGP phase have to be disentangled from the other 'background' sources.

In a QGP, direct photons are emitted as radiation coming from a thermally equilibrated plasma. Due to the excess of gluons in a QGP, an enhancement in direct photons is expected as they are produced through the gluonic channels outlined in equations (3.1)-(3.3).

$$q + \overline{q} \rightarrow \gamma + g \tag{3.1}$$

$$g + q \rightarrow \gamma + q \tag{3.2}$$

$$g + \overline{q} \rightarrow \gamma + \overline{q} \tag{3.3}$$

These direct photons carry information about the thermodynamics of the QGP phase as their momentum distributions are determined by those of the quarks, antiquarks and gluons in the plasma [17]. As the QGP should be formed at temperatures higher than those present in the hadronic phase, the momentum distributions of the photons should show an excess at higher transverse momentum.

Direct photons are difficult to measure experimentally, due to the large background of photons. These can be thought of as two distinct groups, prompt photons from initial hard collisions, and photons emanating from a hot hadronic gas. The direct photons are produced in the initial hard collisions between the partons in the colliding nuclei, through the same partonic processes that will occur in a QGP, given in equations (3.1)-(3.3). However, as the momentum distributions of the photons will be approximately the same as that of the interacting partons, the prompt photons should also have high momentum values (typically $p_t \gg 1$ GeV) [35].

Photons are also produced in the hot hadronic gas phase, but this time are created via hadronic mechanisms, such as those listed in equations (3.4)-(3.8), where the dominant process is believed to be that given in equation (3.6) [36]. Again, the momentum distributions of the photons should be similar to those of the hadrons, and as the hadronic gas phase occurs at a lower temperature than the QGP phase, it should be possible to look for an excess of photons in a given high momentum range [36].

$$\pi^+ + \pi^- \rightarrow \gamma + \rho^0 \tag{3.4}$$

$$\pi^\pm + \pi^0 \rightarrow \gamma + \rho^\pm \tag{3.5}$$

$$\pi^\pm + \rho \rightarrow \mathrm{a}_1 \rightarrow \gamma + \pi^\pm \tag{3.6}$$

$$\pi^0 \rightarrow \gamma + \gamma \tag{3.7}$$

$$\eta \rightarrow \gamma + \gamma \tag{3.8}$$

Recent results from the WA98 experiment at the SPS show the first tentative evidence of direct photons from a QGP phase in nucleus-nucleus collisions [37]. They measure the transverse momentum spectra of photons in both centrally triggered and peripherally triggered events, and draw comparisons with the calculated background from decay processes and annihilations. Figure 3.1a) shows that no enhancement is observed in peripheral collisions, while Figure 3.1b) shows that at higher transverse momentum in the central data, an enhancement of approximately 20% is seen. Certain care has to be taken with these results however as it has been shown that the measured inclusive photon spectra in p+p and $\overline{\mathrm{p}}$+p collisions (equivalent to the direct photons from hard processes in the A+A case) cannot be reproduced exactly by theoretical models, though the deviations are largest at smaller momenta [38].

It has been shown by different authors that it is not necessary to assume a QGP scenario to be able to reproduce this data [39] [40]. The models independently show that the photon yield presented by WA98 can be reproduced by a model which can assume either a hadronic gas phase, or a QGP phase. However, in the version of these models which assume a hadronic gas phase, the initial temperature required to reproduce the data ($\sim$ 230 MeV) is much greater than that required for a phase transition according to lattice QCD calculations (150 - 175 MeV, as described in section 1.3). If these temperatures given by lattice QCD are correct, then the hadronic gas phase described in these models is unphysical.

3.1.2 Low Mass Dileptons

Dileptons (lepton pairs - e^+e^- and $\mu^+\mu^-$) also carry information about the thermodynamic properties of the fireball when they were produced, as again, they only inter-

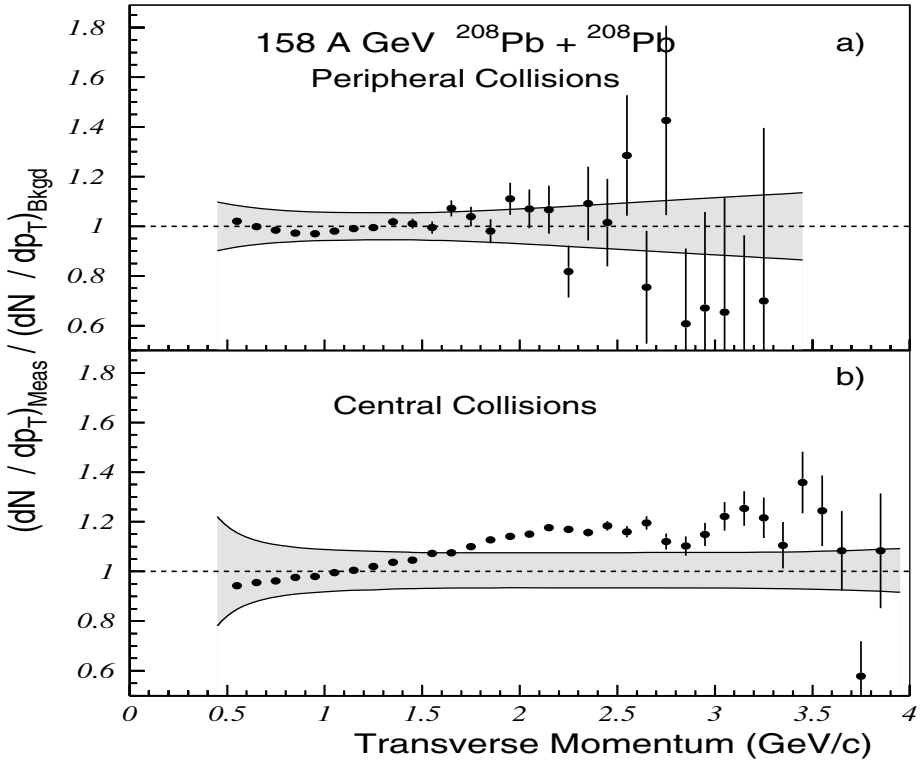

Figure 3.1: The ratio of the measured photon spectra to the calculated background from meson decays for peripheral and central collisions (taken from [37]). The shaded bands represent the systematic errors.

act electromagnetically and can leave the fireball region unaffected. They have an advantage over direct photons, though, in that the mass of the meson which decayed into the lepton pair can be calculated, which means that their production processes may be determined.

In a QGP, lepton pairs are created via the process outlined in equation (3.9), where a γ^* is an off mass shell photon and $l^{\pm}$ represent charged leptons (either $e^{\pm}$, $\mu^{\pm}$ or $\tau^{\pm}$). This is the famous Drell-Yan process. Other processes are allowed, but their contributions are found to be negligible [41].

$$q + \overline{q} \rightarrow \gamma^* \rightarrow l^+ + l^- \tag{3.9}$$

In a hadronic gas scenario, low mass dileptons are produced via the decay of vector mesons, of which the ρ plays a significant role due to its short lifetime ($\sim$ 1-2 fm/c). A large source of dileptons at a low invariant mass ($<$ 200 MeV/c^2) occurs

through the various hadronic decays listed in equations (3.10)-(3.13), though the branching ratios for the meson decays are small. Given these dilepton sources, it was originally calculated by Domokos and Goldman in 1981 that if a QGP phase was present there would be an enhancement of dileptons of approximately an order of magnitude in the mass region between 200 MeV and 600 MeV [41].

$$\gamma \rightarrow e^{+} + e- \tag{3.10}$$

$$\pi^{0} \rightarrow e^{+} + e^{-} + \gamma \tag{3.11}$$

$$\eta \rightarrow e^{+} + e^{-} + \gamma \tag{3.12}$$

$$\omega \rightarrow e^{+} + e- + \pi^{0} \tag{3.13}$$

Dileptons produced only from these hadronic sources should be present for systems where no QGP phase occurs, and it is indeed found that these sources, when modelled with a Monte Carlo (MC) simulation, reproduce the data well for p+Be collisions as measured by the CERES collaboration at the SPS (shown in Figure 3.2).

The CERES collaboration have also measured dilepton spectra in S+Au and Pb+Au collisions at beam energies of 200 GeV/A and 158 GeV/A, respectively, at the SPS. They report tentative evidence for an excess in the low-mass dilepton yield in the mass window starting at 200 MeV/c^2 up to the ρ and ω peaks in the S+Au data [42], whilst a clear excess is then seen in the Pb+Au data [43], which is shown in Figure 3.3. This excess is in comparison to the MC model which described the p+Be data well, scaled for Pb+Au collisions.

The enhancement seen by CERES is in the correct mass region for the enhancement predicted by Domokos and Goldman, but is approximately a factor 4 smaller than their prediction. It is also obvious from Figure 3.3 that there is an excess seen for masses above the ϕ mass, in the so-called intermediate mass range, which was not a prediction of Domokos and Goldman.

The reason for the enhancement below the ρ (770 MeV) and ω (782 MeV) masses is currently an unresolved topic of debate. It has been suggested that it is a product of partial chiral symmetry restoration, where the mass of the ρ decreases, so that the width of the resonance over the whole of the collisions is increased [44] [45]. However, it has also been shown that in-medium broadening of the resonance can occur

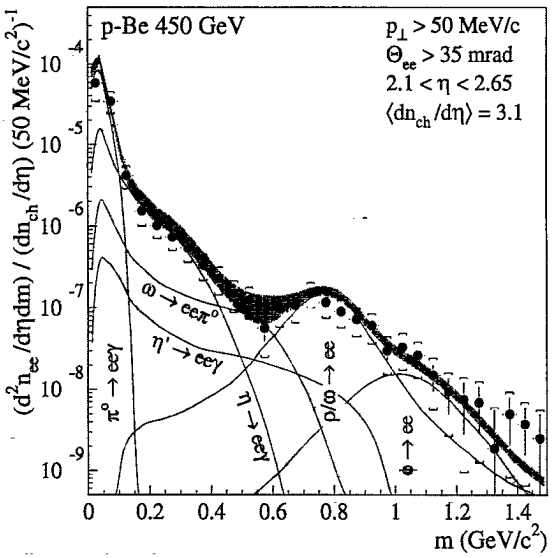

Figure 3.2: Inclusive e^+e^- mass spectrum from the CERES experiment for p+Be collisions at 450 GeV.

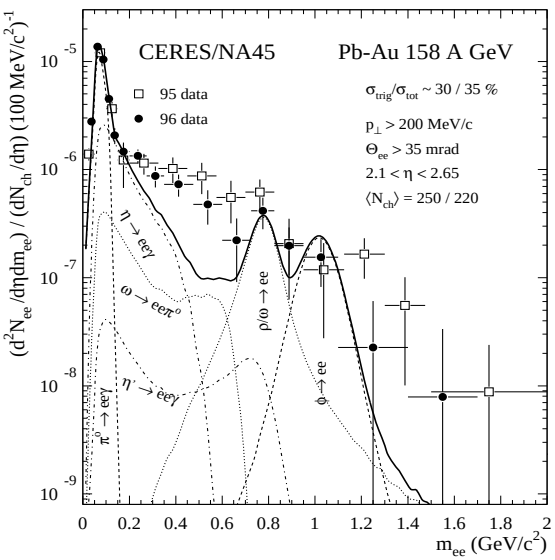

Figure 3.3: Inclusive e^+e^- mass spectrum from the CERES experiment for Pb+Au collisions.

due to hadronic interactions, most notably with pions, which does not invoke a lowering of the mass of the ρ, but rather its spectral density is a function of temperature [46] [47].

Due to the small signal to background ratio in Figure 3.3, more precise data is required to be able to distinguish between the different mechanisms, and to determine whether the enhancement at low and intermediate masses are due to the same phenomena. It has been suggested that the excess of intermediate mass dileptons comes from an enhancement of open charm mesons (e.g. D and $\overline{D}$) which decay in a semi-leptonic mode [48].

3.2 Charmonium Suppression

The J/Ψ meson is a bound $c\overline{c}$ state, the majority of which are formed during the initial stages of the collision, due to the large mass of the c quark (between 1.1 and 1.4 GeV/c^2) compared to the temperatures in the fireball. As the J/Ψ is tightly bound, it is unlikely to become unbound in interactions with hadronic matter, and the dimuons that are the result of its decay leave the fireball region with a low prob-

ability of an interaction, which makes it an excellent probe of the early dynamics of the collision. In a QGP phase, the $c\bar{c}$ pair may become unbound due to the process of Debye-screening, which leads to a suppression in the measured yield of J/Ψs [49]. Experimentally, this suppression must be determined by making a comparison to data where a suppression is not expected, such as in p+p or light A+A collisions.

However, if a QGP is not created, a suppression in the yield of the J/Ψ meson is also observed, which comes from normal hadronic reactions. These come from two different mechanisms, nuclear absorption and absorption with co-moving hadrons, known as comovers. The nuclear absorption can be determined from p+A and light projectile A+B collisions, but the absorption due to comovers, which has a smaller cross-section than nuclear absorption is not well known and has to be inferred from the data, which leads to a systematic uncertainty in this approach.

Experimental data from the NA50 experiment at the SPS[50], in Figure 3.4, exhibits a decrease in the yield of the J/Ψ as the system size and energy increase, where the J/Ψ is measured via its decay channel J/$\Psi \rightarrow \mu^+\mu^-$. The yield is plotted against the variable energy density (ϵ) achieved in the collision, which was estimated from the Bjorken formalism (equation (2.1)) using the measured transverse energy (E_T).

The J/Ψ yield follows the nuclear absorption trend (indicated by a horizontal line at 1 on Figure 3.4) as the system goes from p+A collisions to S+U collisions, where the amount of absorption increases as a function of ϵ, which is just a consequence of increasing the size of the system. However, in the Pb+Pb data, the J/Ψ yield falls off more dramatically, and cannot be explained by absorption alone.

In the deconfinement scenario, the initial fall off at $\epsilon \sim 2.3$ GeV/fm^3 is consistent with a QGP phase. It is thought that this initial drop represents the suppression of the χ_c mesons. The χ_c (3417 MeV) is also a $c\bar{c}$ bound state and is believed to decay into a J/Ψ and a γ. A second drop (or shoulder) is seen at $\epsilon \sim 3.1$ GeV/fm^3 and is thought to represent the suppression of the more tightly bound J/Ψ mesons themselves [50].

One other explanation for this data, which does not invoke a deconfinement scenario, is that the J/Ψ's are broken up as they interact with comovers, which are produced in the fireball and have a similar momentum to the J/Ψ [51]. Models which use this approach have been applied to the experimental data and they can reproduce separately the features present in Figure 3.4. However, none of the models can

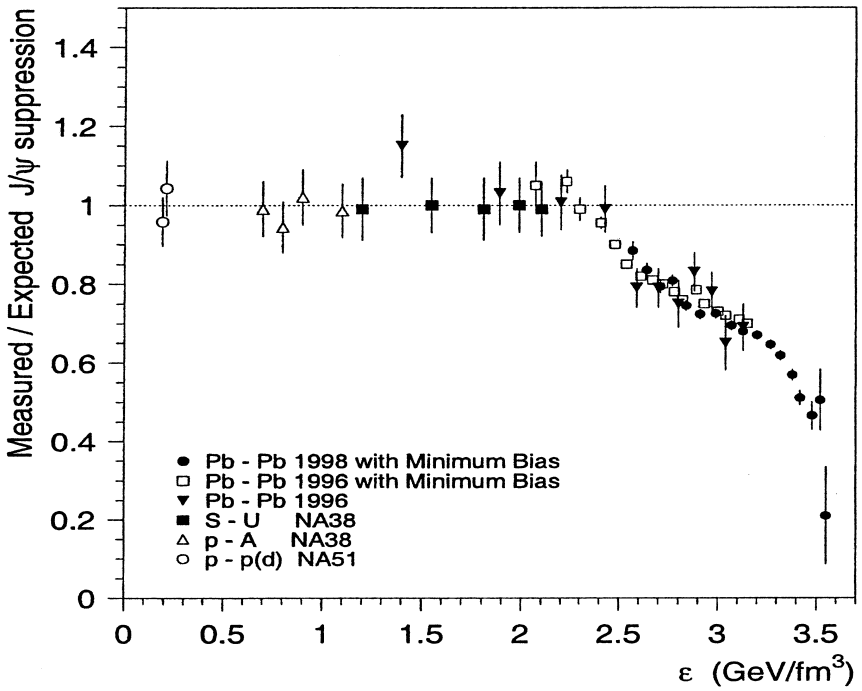

Figure 3.4: Data on J/Ψ yields taken from the NA50 experiment and compared to the expected yield if only ordinary nuclear absorption is present.

simultaneously reproduce the observed decrease in J/Ψ yield at high values of ϵ and also the data at low ϵ which agrees with the expected trend due to normal nuclear absorption [52].

One interesting prediction which has been made, based on the expected production of charm quarks at RHIC, is that there will be an enhancement of J/Ψ mesons at these energies [53]. The means for this is that a large number of J/Ψ, χ_c and D mesons will be produced in the collision and then be suppressed by the Debye-screening mechanism. Once this has happened, the probability for independent c and $\overline{c}$ quarks to combine and form a J/Ψ meson is relatively large, simply due to the large $c\overline{c}$ density. The rates for this process have been calculated and are found to be significant. Indeed, the rates may even be large enough to more than compensate for the suppression of initially formed J/Ψ mesons [53]. This signal has still to be measured at RHIC.

3.3 Strangeness Enhancement

It was proposed by Rafelski in 1982 that if matter went through a phase transition to a QGP, then there would be an enhancement of strange particles in the final state [54]. This enhancement is relative to a collision system where a transition to a QGP phase does not take place, such as p+p or p+A collisions where the system size is very small. The enhancement occurs because different channels are available for the production of strange quarks, as well as a difference in threshold energies due to the fact that in a deconfined state, only the strange quarks have to be produced, rather than the strange hadrons themselves.

3.3.1 Strangeness production in a Hadronic Gas

The hadronic interactions which create strange hadrons have a high energy threshold, which is calculated from the difference in masses between the initial and final state particles. Two such typical reactions involving nucleons (N) are given in equations (3.14) and (3.15). As strangeness is conserved in the strong interaction, a hadron containing an $\overline{s}$ quark must be produced in the same reaction as a hadron consisting of an s quark.

$$N + N \rightarrow \Lambda + K^{+} + N \qquad E_{thresh} \sim 700MeV \tag{3.14}$$

$$N + N \rightarrow N + N + \Lambda + \overline{\Lambda} \qquad E_{thresh} \sim 2200MeV \tag{3.15}$$

These threshold energies are quite large but represent strangeness production in initial collisions of the colliding nuclei. More realistically, the production of strange quarks is dominated by the re-scattering of particles as the fireball is dominated by produced pions, except when the net baryon density is large. The principal channels for strangeness production are given by equations (3.16) - (3.18), which have lower energy thresholds than strangeness production in primary interactions.

$$\pi + \pi \rightarrow K + \overline{K} \qquad E_{thresh} \sim 720MeV \tag{3.16}$$

$$\pi + N \rightarrow \Lambda + K \qquad E_{thresh} \sim 540MeV \tag{3.17}$$

$$\pi + \overline{N} \rightarrow \overline{\Lambda} + \overline{K} \qquad E_{thresh} \sim 540MeV \tag{3.18}$$

Although the threshold energy for production of the Λ and $\overline{\Lambda}$ are the same, (as given by equations (3.17) and (3.18)), dependent upon the amount of stopping, strange baryons are produced more readily due to the absence of anti-nucleons ($\overline{N}$). This is because there are already some protons and neutrons present from the colliding ions, but any anti-nucleons have to be produced. The consequence of this is that the Hadronic Gas phase has to be long lived to enable an equilibration of strangeness.

3.3.2 Strangeness production in a Quark Gluon Plasma

The production mechanisms for strange quarks in a QGP are different to a Hadronic Gas as there are more available production channels for $s\overline{s}$ pairs, due to gluon fusion, as well as the annihilation of light $q\overline{q}$ pairs which are shown in Figure 3.5 [54][55]. As the plasma is expected to be initially gluon rich, and the equilibration of gluons takes time $\tau_g \sim 0.3$ fm/c compared to the quark equilibration time of $\tau_q \sim 2$ fm/c [56] [1], the gluonic channels contribute more than 80 $\%$ to the total production rate for strange quarks [55].

The threshold energy required to create a pair of $s\overline{s}$ quarks in the QGP is just the bare mass of the two strange quarks. This is approximately 1 GeV if the dynamical mass is used, but is between 120 MeV and 340 MeV (the current mass) if a partial restoration of chiral symmetry occurs. This means that due to the high temperatures involved in the QGP phase, the thermal production of $s\overline{s}$ pairs is possible. A further source of enhancement of $s\overline{s}$ pairs comes from the process of Pauli blocking of the light quarks. As all quarks are fermions, they obey the Pauli Exclusion Principle which states that no two fermions can be in the same quantum mechanical state. Therefore, as more and more light quarks are produced in the collision, they fill up the available energy levels and it becomes energetically favourable to create $s\overline{s}$ pairs. It is expected that the extra mechanisms for $s\overline{s}$ production in a QGP should lead to a production rate which is 10 to 30 times greater than in a Hadronic Gas, and this should allow equilibration of strangeness even in the short lifetime of the fireball [55].

It therefore follows that the production of anti-strange and multi-strange baryons

[1] These equilibration times are calculated for full RHIC energies ($\sqrt{s_{NN}}$ = 200 GeV). Although they each depend on the value of $\sqrt{s_{NN}}$, the ratio of $\frac{\tau_g}{\tau_q}$ does not change between $\sqrt{s_{NN}}$ = 200 GeV and $\sqrt{s_{NN}}$ = 130 GeV.

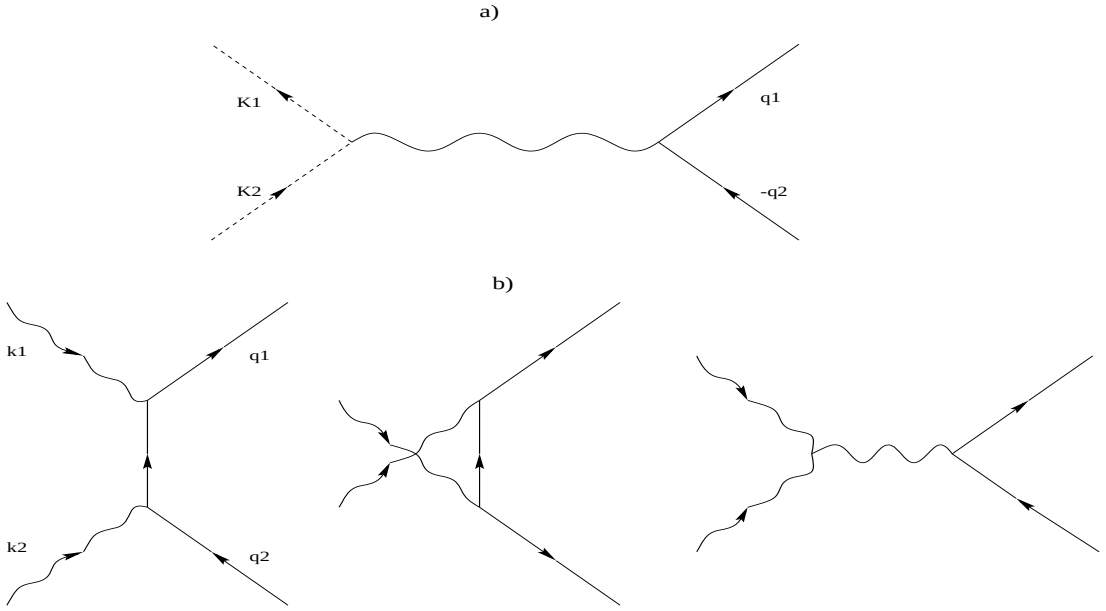

Figure 3.5: Lowest-order QCD diagrams for $s\overline{s}$ production via light quark and gluon annihilation: a) $q\overline{q} \rightarrow s\overline{s}$, b) gg $\rightarrow s\overline{s}$. In both cases, k1 and k2 represent the four-momenta of the incoming particles.

at freeze-out will be enhanced if the system passes through a deconfined phase, than if it remains in the hadronic gas phase only.

Even if an enhancement of strangeness occurs in a QGP, there are still difficulties in quantifying the magnitude of this enhancement. As the lifetime of the QGP phase (or even the fireball in general) is unknown, it is impossible to compute the actual values of particle production in the two different scenarios. An enhancement is expected to occur ordinarily in A+A collisions compared to scaled p+p collisions, as strangeness will be produced in the secondary collisions indicated in equations (3.16)-(3.18). Therefore the unanswered theoretical question is what is the $normal$ enhancement expected in A+A collisions, this can only be inferred from experimental results [57].

3.3.3 Experimental Results

In order to experimentally determine the value of the strangeness enhancement, there have been two basic approaches. The first is to measure the value of the $<K>$ / $<\pi>$ ratio. The second approach is to examine the production of strange and

multi-strange baryons in different systems. The results from these two approaches will now be discussed.

3.3.3.1 $<K> / <\pi>$ ratio

The $<K> / <\pi>$ ratio is an interesting measurement as it links the production of kaons, which carry the majority of the produced strangeness in the collision, with the production of pions, which are the most abundant of the produced particles and can be said to measure the entropy of the collision.[2] An increase in the $<K> / <\pi>$ ratio in A+A collisions compared to p+p or p+A collisions could then indicate an increase in the production of strangeness, where the definitions of $<K>$ and $<\pi>$ are given in equations (3.19) and (3.20).

$$<K> = \frac{K^+ + K^- + 2K_s^0}{4} \tag{3.19}$$

$$<\pi> = \frac{\pi^+ + \pi^-}{2} \tag{3.20}$$

The K^+ / π^+ ratio is often used as a measurement of strangeness enhancement rather than the $<K> / <\pi>$ ratio. The reason is that the production of K^- mesons is suppressed at low AGS energies as the net baryon density is large, and therefore the most probable strangeness production mechanism is of a Λ with a K^+ (equation (3.14)). Figure 3.6 shows the K^+ / π^+ ratio in both A+A and p+p collisions, obtained from an excitation function study of AGS energies [58].

This shows that there is a clear increase in the K^+ / π^+ ratio as a function of $\sqrt{s_{NN}}$ in A+A collisions compared to p+p collisions, though the ratio $\frac{K^+/\pi^+(AA)}{K^+/\pi^+(pp)}$ itself is dependent on $\sqrt{s_{NN}}$, which is demonstrated in Figure 3.7 [59], which also includes a point from the highest energy Pb+Pb collisions at the SPS [60].

The behaviour in Figure 3.7 is very interesting in that it suggests that the observed strangeness enhancement is greatest at the lowest energies and decreases with increasing energy, a trend which is followed up to the highest SPS energy. The interpretation of this is complicated though as at lower energies, the value of the

[2] Pions are easily produced in nucleon-nucleon interactions, but care has to be taken when measuring their yields as the branching ratios are high for the decay of resonances such as the η, ω and ρ, into pionic channels.

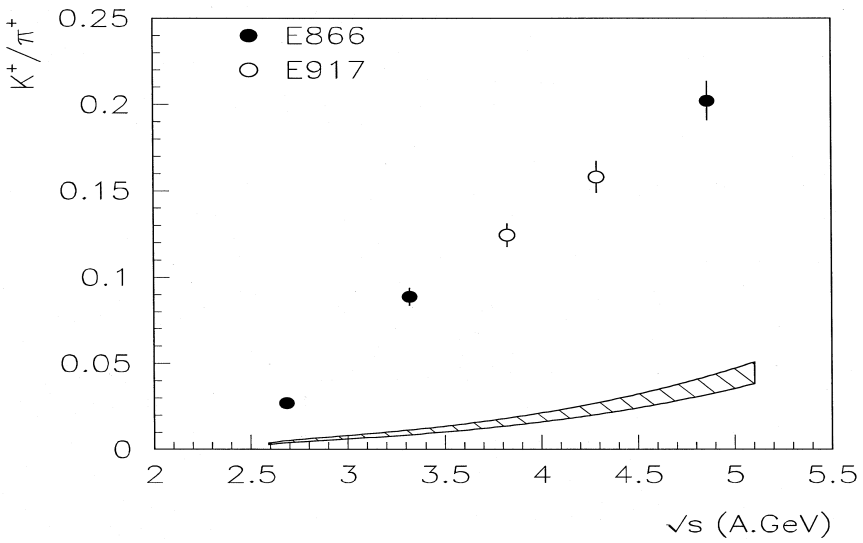

Figure 3.6: K^+/π^+ versus $\sqrt{s_{NN}}$ at the AGS. The circles represent data from Au+Au collisions whilst the hatched regions represent data from p+p collisions.

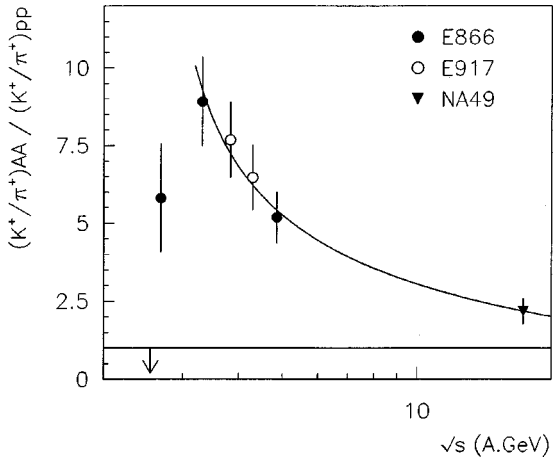

Figure 3.7: K^+/π^+ in A+A versus K^+/π^+ in p+p as a function of energy.

stopping is greater and this leads to an increase in pion absorption (only four fifths of the enhancement at $\sqrt{s_{NN}}$ = 4.7 GeV comes from increased K^+ production [61]). Other problems arise from the fact that at the low energies, the available energy for particle production is below that required for kaons, which will suppress the yield in primary (p+p) collisions, but not necessarily in A+A collisions, due to the amount of secondary collisions. This leads to the point that the enhancement of the K^+/π^+ ratio at the SPS reveals the true extent of the strangeness enhancement, as it is free

from threshold energy constraints. This is also borne out by the measurement of the $<K> / <\pi>$ ratio at SPS energies [62], shown in Figure 3.8, which shows a similar increase in going from p+p to A+A collisions as the K^+/π^+ ratio for the SPS shown in Figure 3.7, a value of approximately 2. This enhancement is independent of energy for the different collision systems at the SPS, S+S, S+Ag and Pb+Pb.

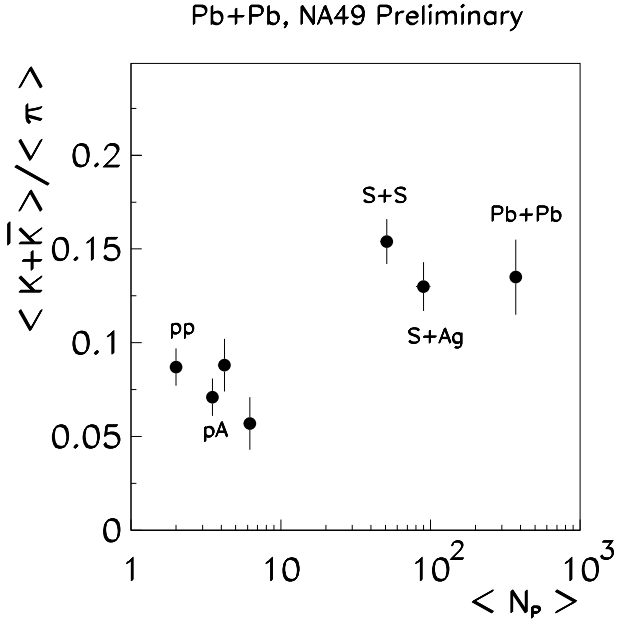

Figure 3.8: Data compiled by the NA49 experiment which shows how the $<$K + $\overline{K}>/<\pi>$ ratio varies as a function of mean number of participants, which is given by the collision system.

As the kaons carry the majority of the produced strangeness, it can be said that there is a global strangeness enhancement of ~ 2 when comparing A+A and p+p collisions at the same energy. This value is confirmed by other experiments at the SPS [63] [64].

3.3.3.2 Strange Baryons

Of particular interest at the SPS is the measurement of the strange and anti-strange baryons, or hyperons. Due to the higher energies available at the SPS compared to the AGS, these particles are more copiously produced. Hyperons are of interest as they not only give information on strangeness enhancement via their total yield,

but by measuring the anti-hyperon to hyperon ratio, they give information on the amount of stopping in the collision.

The WA97 experiment has measured hyperons in p-Be, p+Pb and Pb+Pb collisions with high precision at mid-rapidity [63] [65]. Figure 3.9 shows the relative enhancement at mid-rapidity of hyperons in Pb+Pb collisions, relative to p+Pb data.

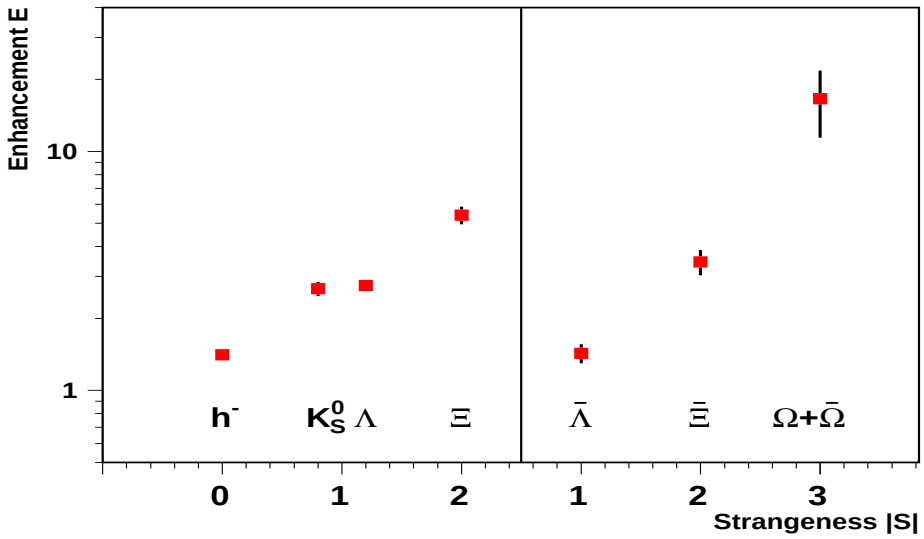

Figure 3.9: Data taken from the WA97 experiment which shows the enhancement of doubly and triply strange baryons in Pb+Pb collisions compared to p+Pb (taken from [63]).

The enhancement factor is calculated relative to p+A data, and as such, it increases with increasing strangeness and is more than an order of magnitude for $\Omega + \overline{\Omega}$, where lack of statistics means that the particle and anti-particle data are summed. Although it is expected that the enhancement of anti-strange baryons would be greater than that for baryons if the collision went through a deconfined phase, the amount of stopping at the SPS means that the strange baryons can still be enhanced by a greater amount than strange anti-baryons, as the production of anti-baryons is suppressed.

WA97 have also made measurements of the (multi)strange (anti)baryon yields in Pb+Pb collisions, as a function of the mean number of participants in the collision, which is a definition of the collision centrality [63]. When the yield is plotted as the yield per participant, then for greater than 100 participants (approximately the 40%

most central collisions), relative to their measurement of p+Pb this enhancement factor for each particle remains constant.

The NA49 and WA97 experiments have both measured strange baryon production in p+p, p+Pb and Pb+Pb collisions [66] [67]. The data, shown in Figure 3.10, shows that an enhancement in Λ ($\overline{\Lambda}$) and Ξ^- ($\overline{\Xi^+}$) yields over and above what is predicted by a wounded nucleon model [68][3], as well as being present in the Pb+Pb data, is already seen in p+Pb collisions, when the p+p data is taken into account. Predictions from a basic wounded nucleon model are shown as a solid line in Figure 3.10. Therefore calculating enhancement factors for A+A data using a wounded nucleon model is unsatisfactory as it cannot describe the enhancement observed in the p+A data.

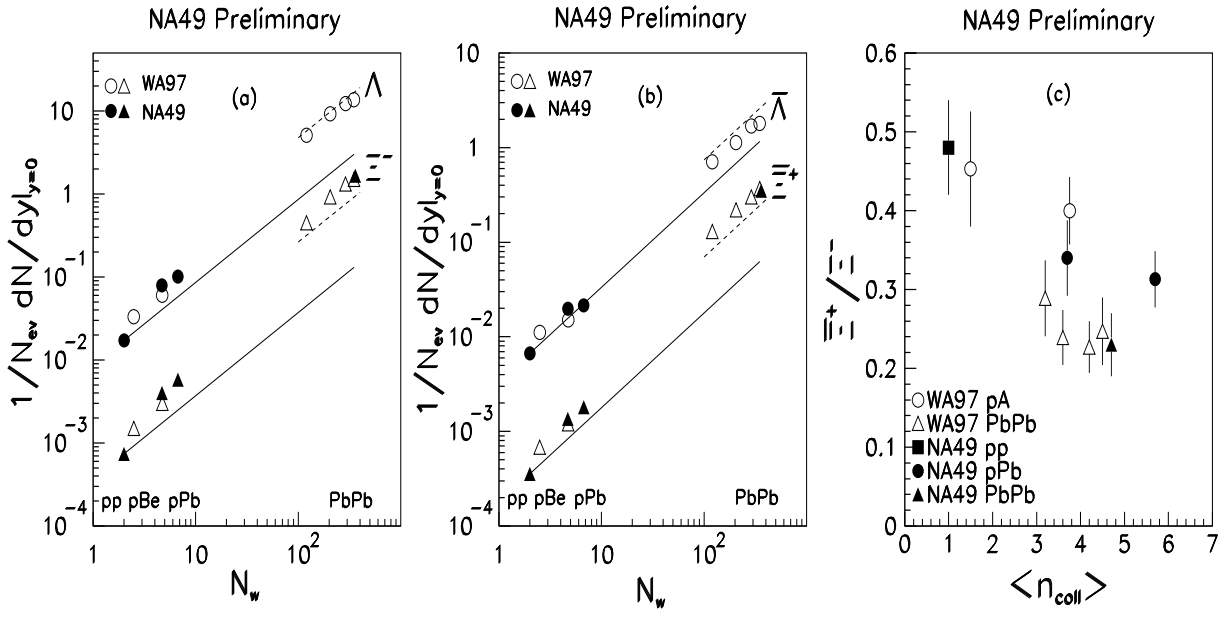

Figure 3.10: Mid-rapidity yields for strange baryons (a) and strange anti-baryons (b) as a function of the number of wounded nucleons. The solid line represents a wounded nucleon model extrapolation based on p+p data, and the dashed line is for a modified wounded model. The $\overline{\Xi^+}/\Xi^-$ ratio at mid-rapidity (c) is also shown.

The dashed line on Figure 3.10 represents a version of the wounded nucleon model, which was modified to describe the p+A data [66]. This gives very differ-

[3]A wounded nucleon model assumes that particle production scales with the number of nucleons which undergo an interaction.

ent predictions when it is extrapolated to A+A collisions compared to the standard wounded nucleon model. This shows therefore that a better understanding of the p+A data is required before quantitative conclusions on the level of the hyperon enhancement can be made about the A+A data.

Chapter 4

Theoretical Models

In order to understand and interpret the experimental data, they must be compared to theoretical models. As described in section 2.2, the different stages of the collision can have disparate physics processes which involve either hadronic or quark and gluon degrees of freedom, so it becomes very difficult to model the whole collision within one model. In particular, it is difficult to model the rapidity (y) and transverse momentum (p_t) spectra of produced particles. With this in mind, many models are developed which just deal with one stage of the collision in particular. There are two types of models, microscopic models which attempt to explain the details of particle production within a particular framework in the fireball, and thermal models which interpret the final state data, assuming that it represents the collisions at chemical freeze-out, and ignore any final state interactions which may be present.

4.1 Microscopic Models

There are three main stages of the collision as shown in Figure 2.1, the Pre-equilibrium phase, the Quark Gluon Plasma phase and the Hadronic Gas phase. Each stage has its own physics models, which are outlined in the next sections. For a complete microscopic treatment of the collision, one must therefore combine these different models.

4.1.1 Pre-Equilibrium Phase

The first stage of the collision is the pre-equilibrium stage, which involves so called 'hard' physics, where inelastic collisions between the partons occur at relatively high momenta. These can be described by parton cascade [69] and string fusion [70] models. The parton cascade is based on perturbative QCD where a nucleus-nucleus collisions is viewed as the inter-penetration of clouds of quarks and gluons which are bound within the initial nuclei. Particle production comes in the form of jets and mini-jets which are formed in the initial interactions. In the string fusion models, a nucleus-nucleus collisions is seen as a superposition of nucleon-nucleon collisions. The interacting nucleons draw colour flux tubes, or strings, between them as they separate, which then fragment via $q\overline{q}$ production, as described in section 1.1. At high densities, the strings overlap to form colour ropes.

4.1.2 Quark Gluon Plasma Phase

The QGP phase occurs when an equilibrated system of quarks and gluons has been created. When this occurs, hydrodynamics can be used to model the expansion and cooling of the plasma [24] [26]. Hydrodynamics describes the evolution of the plasma phase via macroscopic quantities, such as pressure and energy density, which is often obtained using the Bjorken model. Hydrodynamics also introduces the concept of flow, where the fireball expands radially outwards in central collisions due to pressure gradients which build up and is referred to as $radial$ flow. In non-central collisions, these pressure gradients lead to particle flow which can then be generated out of the plane of the collision with an anisotropic distribution, and is described as $elliptic$ flow.

4.1.3 Hadronic Gas Phase

As the QGP fireball expands and cools, the temperatures and densities required for deconfinement are no longer achievable so the quark matter hadronises. This hadronisation process can be modeled by quark coalescence and gluon fragmentation, where hadronic resonances are formed which in turn decay into hadrons [71].

Once hadronisation has occurred, the evolution of the collision can be calculated

microscopically, using known hadron-hadron scattering cross-sections [72]. However, not all hadronic cross sections have been measured accurately, so some model dependent assumptions for these cross-sections have to be used.

4.2 Thermal Models

The thermal model is widely used to describe particle abundances in the hadronic state, using a Boltzmann phase space distribution. An assumption of both kinetic and chemical equilibrium is assumed in its pure form, though an effective suppression factor for quarks of a given flavour (γ) is often used to describe a state in thermal equilibrium, but not complete chemical (flavour) equilibrium. For a system where the critical temperature (T_c) is approximately equal to the value of the strange quark mass, then only equilibrium of the three lightest quark flavours is expected. The beauty, as well as a criticism, of the thermal model is that it makes no assumptions as to how the system achieved equilibrium in the first place.

The first basic assumption of a thermal model is that the fireball, whether it consists of a QGP, hadronic gas or a mixture of both, must be in a state of local equilibrium [73]. There are two different kinds of equilibrium considered here, thermal and chemical. Thermal equilibrium is reached through all scattering processes, both elastic and inelastic, and it defines the temperature of the fireball. This information is reflected in the shape of the momentum spectrum. Chemical equilibrium occurs more slowly than thermal equilibrium as it is reached through inelastic processes only [74], and it defines the particle yields and ratios. Chemical potentials are introduced to describe systems where chemical equilibration is not complete. On the time-scale involved in nuclear collisions, the interactions are dominated by the strong and electro-magnetic force, so no flavour changing weak interactions are allowed.

The parameters that are available for a thermal analysis are the temperature, T, of the system, the volume, V of the system and the chemical potentials, μ_i (i = u,d,s,..), which are used to control the number of conserved quantum numbers in the grand canonical approach. A chemical potential here represents the amount of energy required to add a particle to the system, and is equivalent to the Fermi energy at T = 0 K. As an anti-quark is added to the particle system, it has the possibility

of annihilating with a quark at the top of the Fermi sea, independent of how many anti-quarks are already present. As this will liberate the energy of the particle, μ_i, the chemical potential of an anti-quark is defined as -μ_i.

The average hadronic particle multiplicities, N_i of species i, are obtained via equation (4.1) which assumes a Boltzmann statistical distribution, which is a valid assumption in the cases of low densities or high temperatures [75] :

$$\begin{aligned} N_i &= g_i V \int \frac{d^3p}{(2\pi)^3} \exp\left[-\frac{(E_i - \mu_i)}{T}\right] \\ &= \frac{g_i m_i^2 T}{(2\pi)^2} K_2 \frac{m_i}{T} \exp\left[\frac{(\mu_i)}{T}\right] \end{aligned} \tag{4.1}$$

where g_i represents the degeneracy and K_2 is a Bessel function [76]. The error involved in using the Boltzmann approximation, instead of full Fermi-Dirac or Bose-Einstein statistics has been shown to be negligible for any particle with a mass greater than that of the π meson ($\sim$ 140 MeV/c^2) [77].

An approximation can be made to equation (4.1) by introducing the fugacity term to describe particle yields. The relationship between the fugacity and chemical potential is given in equation (4.2).

$$\lambda_i = e^{\frac{\mu_i}{T}} \tag{4.2}$$

The fugacities for particle and anti-particle are related by the expression given by equation (4.3).

$$\lambda_{\bar{i}} = \lambda_i^{-1} \tag{4.3}$$

On the hadronic scale, the fugacity is given by the product of the valence quark fugacities, which leads to $\lambda_p = \lambda_u^2 \lambda_d$ and $\lambda_\Lambda = \lambda_u \lambda_d \lambda_s$.

As, initially, there are no strange quarks in the fireball coming from the colliding nuclei, and m$_s$ $\sim$ T$_c$, Rafelski suggested that the strangeness flavour may not reach its equilibrium value, whereas the u and d quarks are more likely to, due to their small current masses [78]. He introduced the factor γ_s which represents the amount of strangeness chemical equilibration, where $0 \leq \gamma_s \leq 1$, and γ_s = 1 represents full equilibrium. The strangeness fugacities are now modified according to equations (4.4) and (4.5).

$$\lambda_s^{'} = \gamma_s \lambda_s \tag{4.4}$$

$$\lambda_{\overline{s}}^{'} = \gamma_s \lambda_s^{-1} \tag{4.5}$$

It is possible to obtain the value of μ_B, T, μ_s and γ_s from experimental data by measuring ratios of strange particles. Two such ways are given in equations (4.6) and (4.7) as all the degeneracy factors, masses and the unknown fireball volume factors in equation (4.1) cancel, leaving just the relevant fugacities :

$$\frac{\overline{\Xi^+} \cdot \Lambda \cdot \Lambda}{\Xi^- \cdot \overline{\Lambda} \cdot \overline{\Lambda}} = \lambda_u^4 \lambda_d^2 \tag{4.6}$$

$$\frac{\overline{\Lambda} \cdot \Xi^- \cdot \Xi^-}{\Lambda \cdot \overline{\Xi^+} \cdot \overline{\Xi^+}} = \lambda_s^6 \tag{4.7}$$

4.3 Applications of the Thermal Model

As the thermal model by definition knows nothing about the history of the fireball before freeze-out, a thermal model analysis can be undertaken for the two possible scenarios, with and without a QGP. In these instances, the chemical potentials can either be quark or hadronic chemical potentials.

The assumption that only a hot hadronic gas is formed in these collisions has been pursued independently by Becattini and Cleymans and their collaborators [76] [79]. Both methods assume the local conservation of quantum numbers, which means that, for instance, net strangeness must be balanced locally and not just over the whole fireball when it is formed. They also allow for the possibility that the chemical equilibration of strangeness does not occur, and define this using the factor, γ_s, introduced previously. Becattini and Cleymans allow for the creation of multiple fireballs, which are introduced so as to be able to reproduce the observed rapidity dependence of particle yields in the experimental data. Cleymans has shown that by only considering particle ratios, the effects of particle flow and the case of multiple fireballs with different rapidities all cancel out [76]. Becattini, on the other hand, allows each fireball to have its own temperature and volume, and then obtains the overall event multiplicity by calculating a weighted sum of the average multiplicity in each of his multiple fireballs [79].

As shown in Figure 4.1, Becattini and Cleymans analyses are in good agreement with the data from the three different energy ranges at the SIS, AGS and SPS [80]. As is indicated on the figure, the value of γ_s obtained for collisions at both the AGS and SPS is approximately 0.7, which corresponds to a value of approximately 0.5 obtained when performing a statistical analysis on p+p data [81]. This indicates that strangeness is not fully equilibrated in heavy ion collisions, even at the highest SPS energies.

Thermal model analyses which assume a QGP scenario have been studied by Braun-Munzinger [82] and Rafelski [83].

The model by Braun-Munzinger $et.\ al.$ assumes complete thermal and chemical equilibrium (γ_s = 1)and uses a grand canonical approach, whereby quantum numbers are conserved globally, rather than locally. By fixing the volume of the fireball as well as the strangeness chemical potential only two free parameters remain, the temperature, T, and the baryo-chemical potential, μ_B, where $\mu_B = 3\mu_q$, and $\mu_q = \frac{\mu_u + \mu_d}{2}$.

This model has then been applied to the data from Pb+Pb collisions at the SPS, and is in good agreement with it, as shown in Figure 4.2. The values obtained for T and μ_B are T = 168 $\pm$ 2.4 MeV and μ_B = 266 $\pm$ 5 MeV.

The model by Rafelski on the other hand, allows for chemical non-equilibrium of both strangeness and the light quark flavours within his thermal model, thereby introducing an extra factor, γ_q. This, he argues, may be brought about by the sudden breakup of the QGP fireball, where the chemical freeze-out and thermal freeze-out points overlap [83]. With this, the model once again reproduces the data well, and even leads to an overpopulation of the strange quark phase space, i.e., $\gamma_s > 1$, which is in contrast to the result from Becattini.

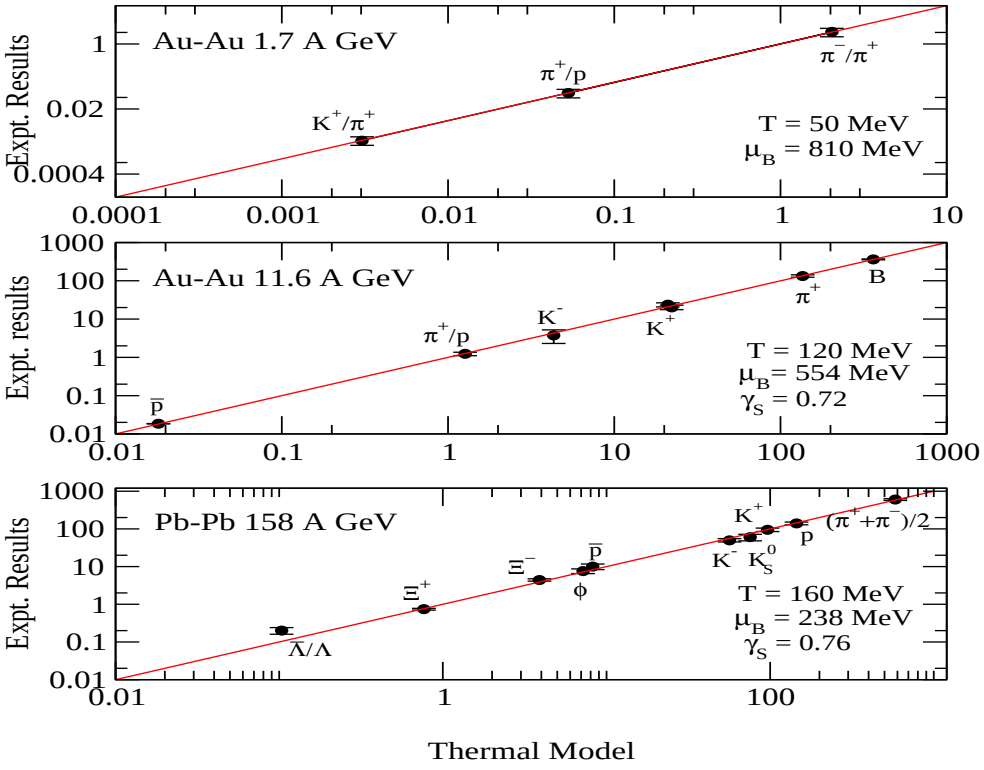

Figure 4.1: Comparison between measured particle multiplicities and those obtained using a HG type thermal model

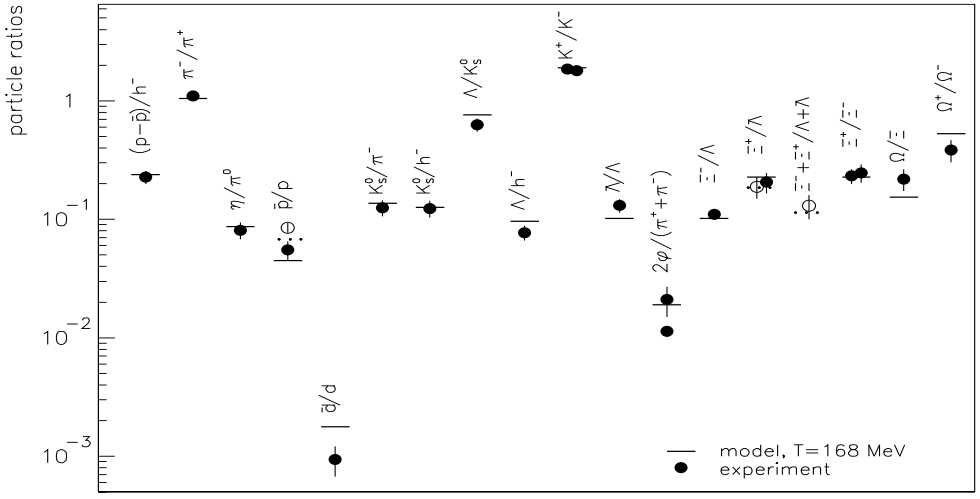

Figure 4.2: Comparison between measured particle ratios and those obtained using a QGP type thermal model

4.4 Limitations of the Thermal Models

There are three main limitations that have to be considered when analysing experimental data from relativistic heavy ion collisions within a thermal model.

The first problem arises due to the differences in the experiments which take the form of different acceptances and trigger conditions. Particle yields can only be measured in the rapidity and p_t intervals that fall within the acceptance of an experiment, which can be different for different particle species depending on their mass. Also, for example, different experiments may include a different percentages of the hadronic cross-section (or collision centralities) in their event samples in order to increase statistics.

The second problem with thermal model analyses is the assumption that the freeze-out occurs at constant temperature and chemical potential within the produced fireball. It has been shown that the central rapidity region contains fewer baryons than the target and projectile regions, so this should be taken into account in the chemical potentials.

Finally, the third and perhaps the largest problem concerns whether a system that has at most 400 participating nucleons and a few thousand produced particles, can actually be said to be in equilibrium. The finite size of the system introduces boundaries to the system, which can only ever be in a state of local equilibrium.

These problems mean that a global thermal model fit to heavy-ion data cannot provide more than a rough picture of what is happening and that minimising errors so that fits agree with experimental detail to a high precision is not necessarily the best method to use, as some deviations from experimental data would be expected.

4.5 Summary of Current Status

The abundance of experimental data now available, especially from experiments at the SPS, should give a clearer indication as to what is happening in these collisions. A report was released by CERN in early 2000, stating that there was ”compelling evidence (from the SPS data) that a new state of matter has indeed been created ...” [84]. This conclusion is based upon the results outlined earlier in this chapter.

However, one has to be careful when looking at this data. The J/Ψ suppression

follows normal nuclear absorption up to and including S+S collisions, before it drops off beyond what is expected, in Pb+Pb data, and the reported excess of direct photons is also only apparent in Pb+Pb data. However, the available data on strangeness enhancement, summarised in Figure 3.8, shows that the global enhancement of a factor of 2 is present for all systems at the SPS. This simple comparison indicates that either there is a discrepancy between the two signatures, or that their effects turn on with different initial conditions.

New results from NA49 show that there is also strangeness enhancement observed in p+Pb data at different collision centralities, which means that this has to be taken into account when modelling the enhancement in A+A collisions. The fact that WA97 do not see a 'switch on' effect in the strangeness enhancement when looking at Pb+Pb data at different centralities is also very interesting, as shown in Figure 3.10, though they only measure the most central 40% of the collisions.

The advent of RHIC means that data will be available at energies a factor of ten higher than previously seen. These higher energies suggest that a different region of the nuclear phase diagram is being explored, where less stopping takes place, and where the fireball region is baryon poor. With these higher energies come possible new QGP signatures, such as the suppression of jets which are created during the initial partonic collisions, as they travel through the deconfined dense medium of quarks and gluons [85].

Chapter 5

Experimental Setup

5.1 The Relativistic Heavy Ion Collider

The Relativistic Heavy Ion Collider (RHIC) is a new facility situated at BNL which is mainly dedicated to relativistic heavy ion research and in the year 2000 it completed its first period of operation. RHIC is designed to run with Au ions (79+), with a luminosity of approximately 10^{27} cm^{-2}sec^{-1} at a beam energies of between 30 and 100 GeV/A, which leads to centre of mass ($\sqrt{s_{NN}}$) energies of between 60 GeV and 200 GeV, up to an order of magnitude greater than any previous heavy ion accelerating facility. As well as the heavy ion beam programme, RHIC will also have the capability to accelerate polarised and unpolarised protons to a maximum beam energy of 250 GeV/A. Unpolarised protons will provide data for p+p and p+A collisions, which are an essential benchmark in understanding A+A data. The polarised protons will be used to facilitate research into the nucleon spin problem [86] [87].

The RHIC (illustrated in Figure 5.1) is injected with ions which have been accelerated to $\sim$ 10.8 GeV/A, the maximum beam energy available for Au ions from the AGS. Figure 5.1 also shows the beam energy and charge as it exits from each of the preliminary accelerators.

The collider comprises two concentric superconducting synchrotrons, 2.4 miles in circumference, where each ring accelerates ions in opposite directions. There are six interaction points located around the RHIC ring, four of which currently have experiments associated with them.

The first 'year' of data taking, referred to as year 1, lasted from June through

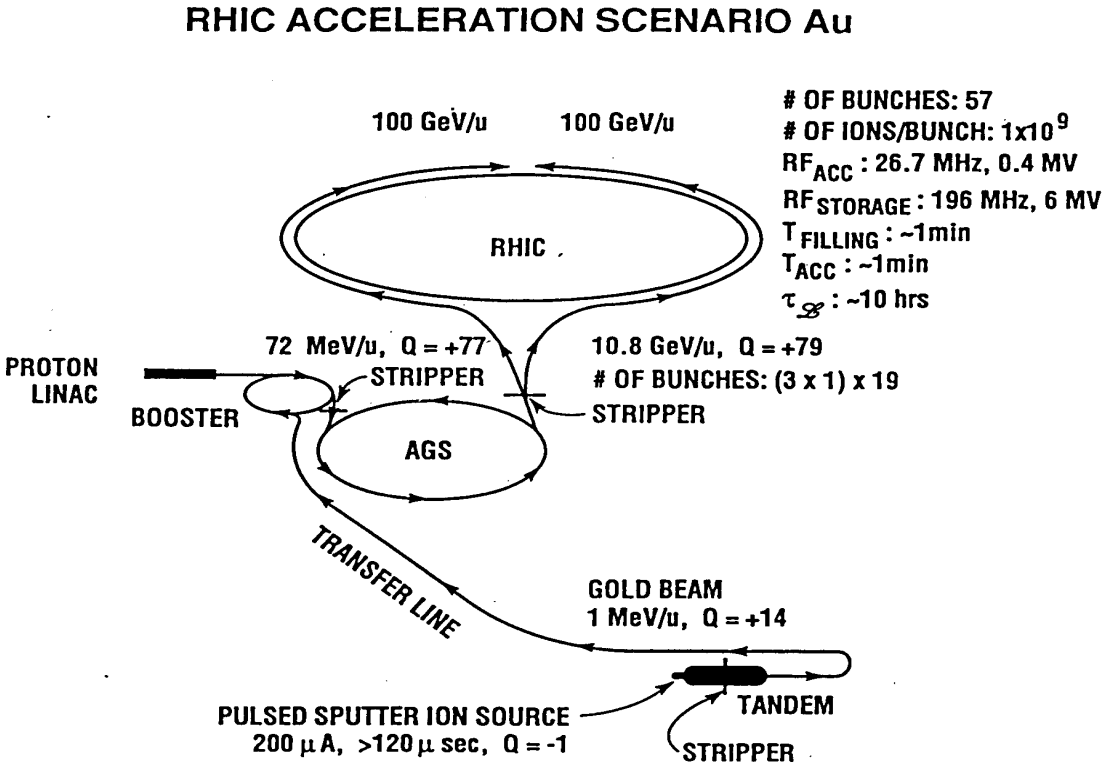

Figure 5.1: The RHIC accelerator complex

to September 2000. The maximum beam energy achieved during this time was 65 GeV/A, at $\sim$10% of the design luminosity.

5.1.1 The RHIC Experiments

The four RHIC experiments are BRAHMS (Broad Range Hadron Magnetic Spectrometers), PHOBOS [88], PHENIX [89] (Pioneering High Energy Nuclear Interaction experiment) and STAR (Solenoidal Tracker At RHIC).

BRAHMS is one of two smaller RHIC experiments, and focuses on measuring hadrons over a wide range of rapidity. It accomplishes this by having a movable spectrometer arm at forward angles of narrow acceptance, as well as a small Time Projection Chamber (TPC) at mid-rapidity, and can measure hadrons over the range $0 < |y| < 4$ and $0.2 < p_t < 3$ GeV/c. This gives BRAHMS the capability to record particle production at mid-rapidity, as well as in the beam fragmentation regions.

PHOBOS is the other small experiment at RHIC. It utilises silicon detectors to trigger on every collision, and therefore has a high data rate. The wide acceptance

coverage of the detector setup means that all of the particles produced in the collision can in principle be measured. With this, PHOBOS can measure single particle spectra, as well as particle correlations.

The PHENIX experiment is one of the two larger RHIC experiments, with a collaboration of over 400 physicists. PHENIX specialise in measuring muons and photons, with which they can make a measurement of the J/Ψ, the ϕ, and the π^0, via their decay products (J/$\Psi \rightarrow \mu^+\mu^-$, $\phi \rightarrow e^+e^-$ and $\pi^0 \rightarrow \gamma\gamma$). This is achieved by having two large muon arms, in the backward and forward rapidity regions, but these were not implemented in the first year.

The STAR experiment is the other large experiment, again consisting of approximately 400 collaborators. STAR is a multi-detector experiment based around a large TPC situated in a magnetic field . Although the large drift time of the TPC leads to the lowest data rate of all four experiments, STAR has a vast array of measurable observables, ranging from single particle spectra (including strange and multi-strange particles), to particle correlations, to electro-magnetic interactions only between the incoming nuclei. The large acceptance of the TPC even allows measurements to be made on an event by event basis, allowing for studies of event by event fluctuations.

The versatility of the different experiments should yield a complete picture of heavy ion collisions at RHIC, covering all suggested QGP signatures.

5.2 The STAR Experiment

STAR is a large acceptance experiment consisting of a number of detectors, situated inside a large solenoid, of strength 0.25 Tesla in year 1, which will be increased to 0.5 Tesla in future years. The main tracking detector in STAR is the large Time Projection Chamber. The implementation of the detectors is staged over a three year period, the final configuration of which is shown in Figure 5.2. The detectors are either used to trigger on an interaction, or to track and measure the particles created in a collision. The setup for year 1 comprised only the Time Projection Chamber (TPC), Ring-Imaging Cherenkov Counter (RICH), Central Trigger Barrel (CTB) and the two Zero Degree Calorimeters (ZDCs or ZCals).

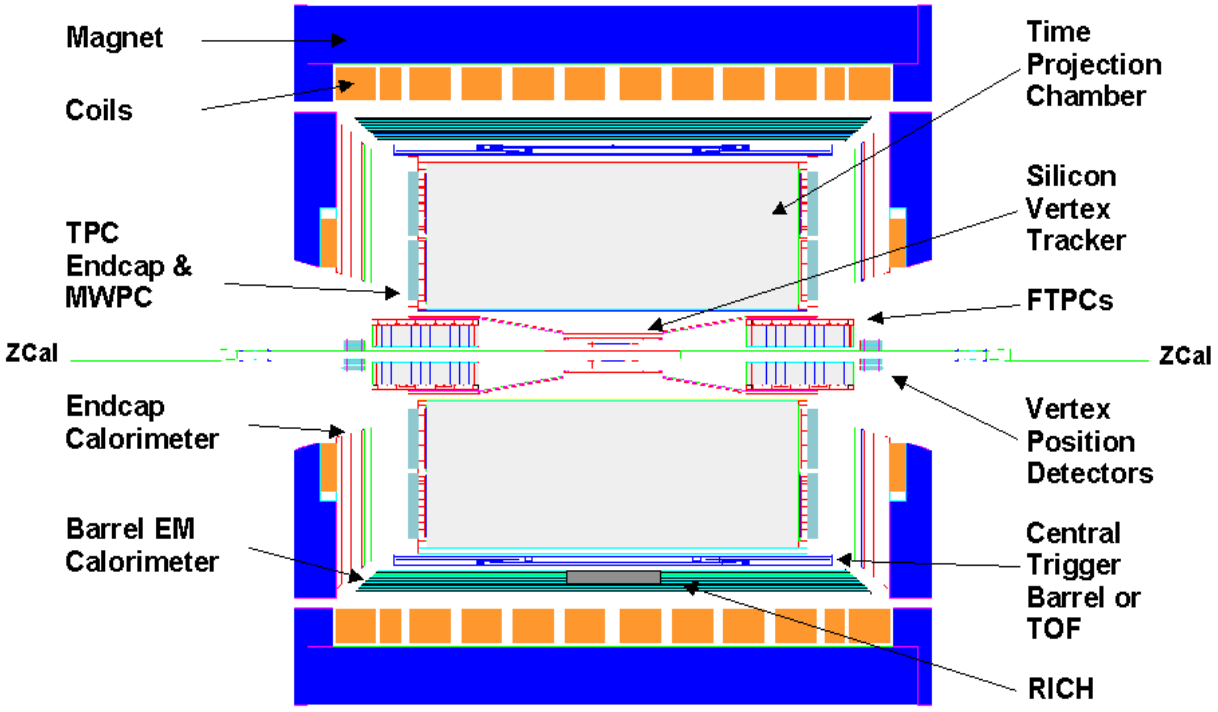

Figure 5.2: The STAR detector setup

5.2.1 The Tracking Detectors

In its year 1 configuration, the Time Projection Chamber (TPC) was the only tracking detector in STAR. The RICH was also installed, but as it only measures the momentum of the particle, as well as providing good particle identification, it is not classed as a tracking detector. These were supplemented in year 2, which extended from June through November 2001, by the Silicon Vertex Tracker (SVT) and two Forward Time Projection Chambers (FTPC's). In later years, the Silicon Strip Detector (SSD) will also be added.

5.2.1.1 The Time Projection Chamber

The main TPC is the principal tracking detector in STAR and was chosen for its large acceptance and high granularity, which makes particle identification possible. TPCs have been demonstrated to work successfully in high multiplicity environments in earlier Relativistic Heavy Ion experiments at both the AGS (E810,E895) and at the SPS (NA35, NA36 and NA49) [90].

The TPC is a cylindrical gas-filled tracking chamber which is 4.2m in length, and 4m in diameter. It has an inner radius of 50cm and extends out to 2m which, when combined with the length, represents an acceptance of ± 1.5 units of pseudo-rapidity, η.

P10 gas, a mixture of 90% Ar and 10% CH_4, is used as the gas in the drift volume for a number of reasons. It has a small transverse and longitudinal diffusion which leads to a good two track separation, while the electron drift velocity is $\sim$5cm/μs at E $<$ 300 V/cm [91], where the drift velocity determines the event rate of the detector. Importantly, this gas mixture works at atmospheric pressure.

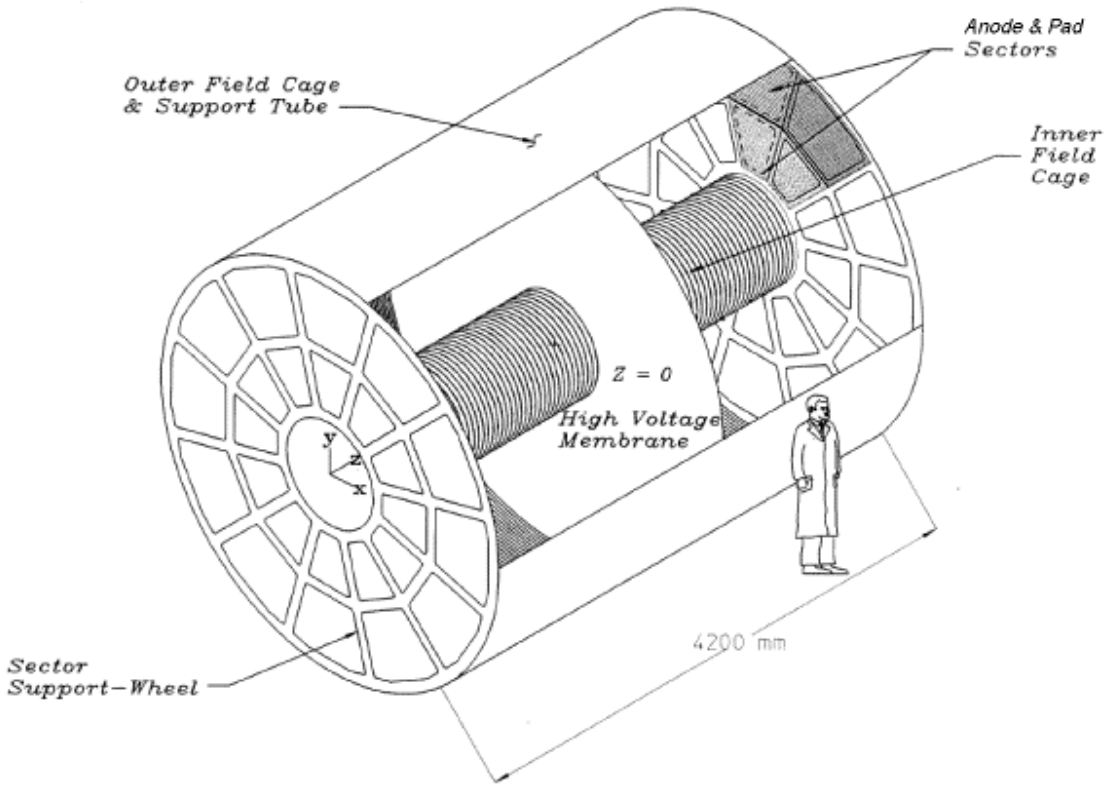

Figure 5.3: A cutaway view of the Time Projection Chamber

At the centre of the TPC is a thin cathode membrane, made from Aquadag painted mylar (see Figure 5.3). This cathode plane is maintained at a high voltage (-31 kV) so as to create a longitudinal electric field between the membrane and the ends of the TPC which are held at ground potential. Outer and inner field cages surround the drift volume in order to keep the electric field uniform at 148 V/cm. They are made out of rings of lightweight cylinders of Nomex honeycomb sandwiched between

two layers of Kapton, which have either Al or Cu stripes on them to form the rings around the circumference. The thin cathode membrane is connected to one of these stripes on the inner and outer field cages. There are 364 rings in total, each 10 mm wide, with a 1.5 mm gap between them, and are connected by a potential resistor chain, each resistor being 2 MΩ [92]. The field cages are very thin, with the inner field cage having a radiation length of 0.62%, and the outer field cage having a 1.26% radiation length.

The magnetic field created by the solenoid is parallel to the electric field and causes charged particles to follow helical trajectories. Their momentum can then be calculated from their radius of curvature, using equation (5.1) :

$$p_t = 0.3qBR \text{ (MeV/c)} \tag{5.1}$$

where p_t is the transverse momentum of the particle, q is the charge of the particle, B is the magnetic field strength and R is the radius of curvature.

When a charged particle, produced in the collision travels through the TPC, it will ionise the gas, producing secondary electrons. These secondary electrons will then drift towards one end of the TPC under the influence of the electric field. As they reach the end of the drift volume defined by the shield grid (often referred to as the ground plane), shown in Figure 5.4, they are accelerated towards a grid of anode wires which are held at 1265 V. As the electrons are accelerated, they cause further ionisation in the gas. The electrons which are created in this process are also accelerated towards the anode grid. This process repeats itself until an avalanche occurs. The drift of the positive ions created in the avalanching process then induce a charge on the cathode plane which is divided into individual pads and located behind the anode grid (see Figure 5.4). This induced charge is proportional to the initial ionisation.

A gating grid prevents the positive ions from re-entering the drift volume. It operates at -135 V and is positioned between the anode grid and the drift volume and is opened and closed when necessary.

Each face of the TPC comprises 12 super-sectors, each containing an inner and outer sector of cathode pads which mount into the TPC end-cap wheel, as shown in Figure 5.3. The cathode pads are arranged into planes, or rows, with 13 pad-rows in

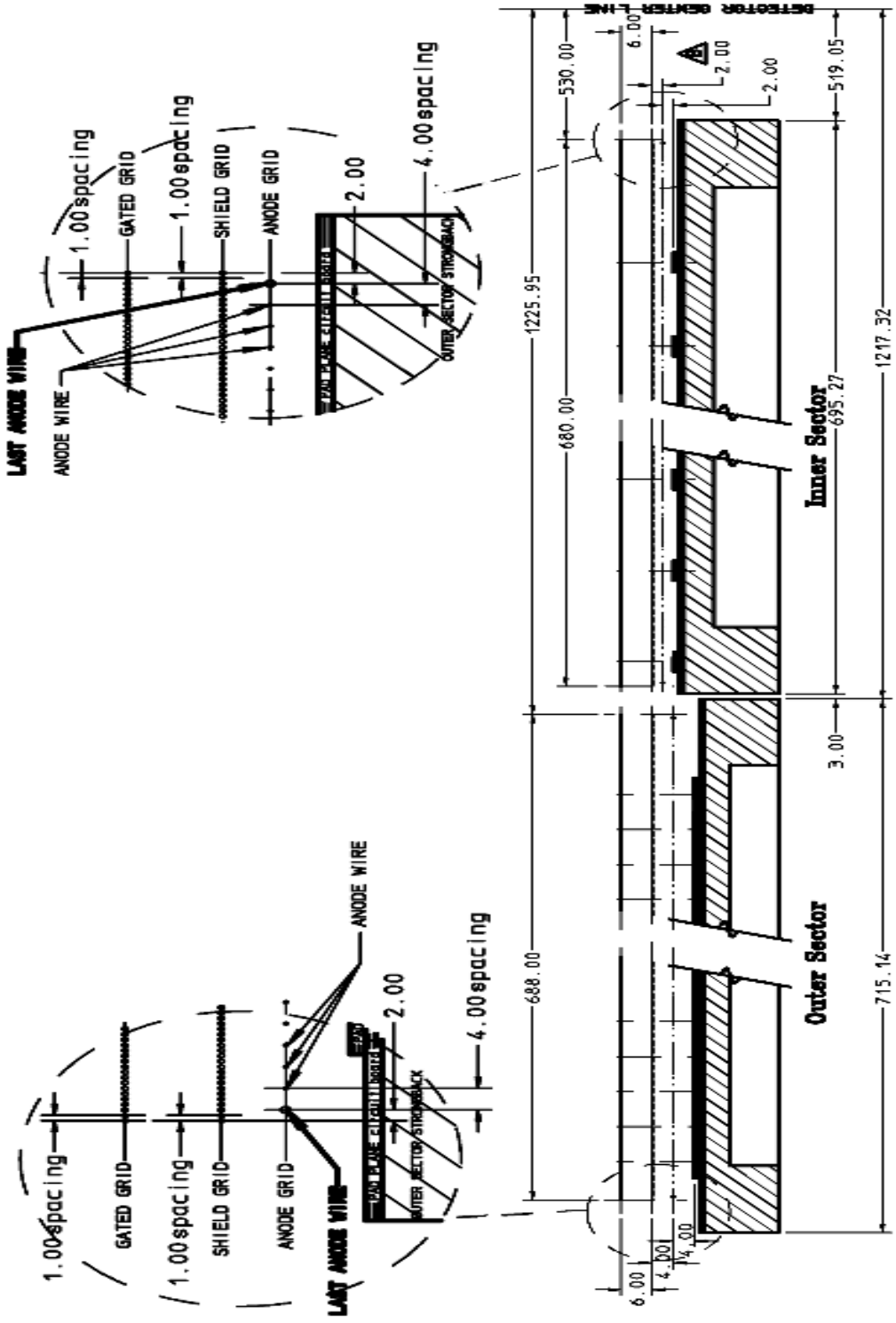

Figure 5.4: The readout planes for a sector in the TPC, where the dimensions are in mm (taken from [93]).

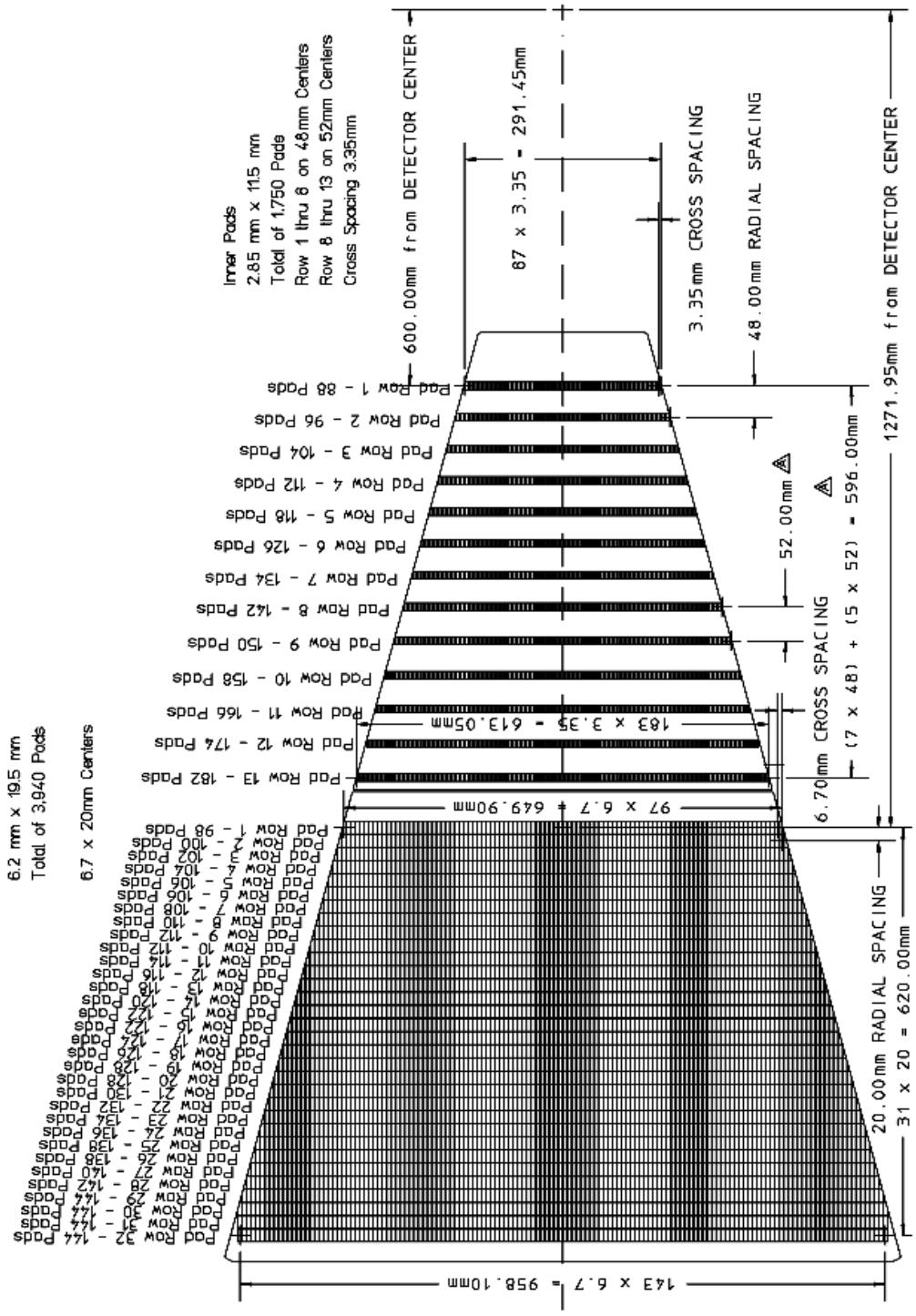

Figure 5.5: The arrangement of the cathode pads in each of the 24 sectors of the TPC, (taken from [93]).

the inner sector, and 32 in the outer sector which is illustrated in Figure 5.5. The pads in the inner sector are smallest (2.85 mm by 11.5 mm) and were chosen so that they provide good two-track spatial resolution in the high track density region which exists close to the interaction vertex by providing close space points. The size of the pads is limited by the space required for the electronics on the face of the TPC. The large outer segment pads (6.2 mm by 19.5 mm) completely cover the area under the anode wires which means that the outer sector is optimised for dE/dx measurements in the lower track density region, allowing for good particle identification. There are a total of 45 pad-rows in each sector, which comprise 5690 pads, which leads to $\sim$ 137,000 readout channels on the TPC. The charge on each pad is then sampled in 512 time bins. This leads to a total number of $\sim$ 70 million samples, or pixels.

5.2.1.2 The Readout of the TPC

The readout of the TPC pads is performed by chips on front end electronics (FEE) boards, with each pad having two chips associated with it. The first chip incorporates the pre-amplifier, shaper and buffer, while the second chip is a novel Switched Capacitor Array (SCA) and Analogue to Digital Converter (ADC) which was first used by the NA49 experiment [94]. The SCA itself comprises 512 capacitors, each one of which integrates the charge from one particular time bin. The amount of charge stored in each capacitor is subsequently converted to a digital number between 0 and 255.

However, due to the slow moving positive ions, the time signal induced on the cathode plane has a long tail, of approximately 62 μs. This is a large number, so in order to make the detector operate more quickly, the signal is differentiated after the characteristic shaping time of the pre-amplifier. Although this means that the detector is faster, only a fraction of charge (F) is seen by the electronics, determined by equation (5.2),

$$F = \frac{ln(1 + \frac{t_s}{t_0})}{ln(1 + \frac{t_m}{t_0})} \tag{5.2}$$

where t_0 represents the time it takes for the signal to develop ($\sim$ 1 ns), t_s is the shaping time of the pre-amplifier ($\sim$ 180 ns), and t_m is the duration of the signal ($\sim$ 62 μs. As a consequence, only $\sim$45$\%$ of the charge is used by the electronics.

The FEE cards then pass the ADC values for every channel to a read out board, of which there are 6 per super-sector. As the pixel occupancy in an event is at most 10%, there is a large amount of unnecessary space taken up by pixels which do not have any data, and only contain noise. The amount of noise on a chip is calculated by reading out the TPC when it has no data in it, and these are defined as $pedestal$ runs. Each read out board comprises a custom chip which moves the data from the ADC to a buffer, whilst subtracting the pedestals in a process known as $zero\ suppression$, which can reduce the data volume by up to a factor of 10. The location of charge clusters are also determined at this stage in the read out boards though, for now, this information is not used and cluster finding is performed in the offline analysis chain (described in section 6.1).

At this stage, each of the read out boards are read out in turn via communication with a 'global broker' chip, which communicates with all read out boards which are sometimes referred to as 'detector brokers'. The data is stored on disk, the location of the data from each read out board is in accordance with the 'event builder' which stores the pointers between the event information. Once complete, the whole event is sent sequentially down a gigabit optical fibre link to tape, in the mass data storage system.

5.2.2 The STAR Trigger System

There are approximately ten thousand beam crossings every second at RHIC, but STAR's recording rate is limited to $\sim$ 1Hz, so each event that is recorded has to be selected according to its suitability, determined by certain trigger criteria. As the majority of the Au+Au collisions are at large impact parameters, whereby not all of the participant nucleons interact, it is usually desirable to trigger on collisions with small impact parameters (central collisions) as it is expected that a QGP could be formed in these collisions. In order to measure quantities as a function of centrality, it is also desirable to accept the full range of impact parameters, which are referred to as minimum bias events, as these represent interactions with little or no bias (e.g., a low threshold on event multiplicity).

5.2.2.1 The Trigger Detectors

The trigger detectors in place during the year 1 data taking period were the Multi-Wire Proportional Chamber, the Central Trigger Barrel, and two Zero Degree Calorimeters. In the near future, Vertex Position Detectors (VPDs, whose coverage is 3.3 $< |\eta| <$ 3.8) and a Barrel Electro-Magnetic Calorimeter (BEMC) will also be added.

5.2.2.2 The Multi-Wire Proportional Chamber

The anode wires on the faces of the TPC are also utilised as a fast Multi-Wire Proportional Chamber (MWPC). These may be used to gather the charge deposited by tracks which actually pass through the TPC end-caps and therefore give a measure of the event multiplicity in the pseudo-rapidity range $1 < |\eta| < 2$. There are a total of 9000 anode wires, which are read out in 2000 separate segments.

5.2.2.3 The Central Trigger Barrel

The Central Trigger Barrel (CTB) surrounds the TPC at a radius of $\sim$ 2m from the nominal vertex position, and has a length of $\sim$ 4m. The CTB is sensitive to particle multiplicity in the range -1 $< \eta <$ 1 if the interaction vertex occurs at the centre of the TPC (co-ordinates defined as (0,0,0)), with a full 2π azimuthal coverage. It consists of 120 trays, each containing 2 scintillator slats. Scintillation photons are detected by a photo-multiplier tube, where the light output is proportional to the track multiplicity. As the multiplicity of the event is proportional to $\frac{1}{b}$, where b is the impact parameter, a trigger can be defined using the multiplicity that is detected in the CTB, which determines the centrality of the collision. In the initial stages of the trigger, the information from the 240 scintillator slats is divided into 16 segments (4 in η by 4 in ϕ), which allows faster processing.

5.2.2.4 The Zero-Degree Calorimeters

Two hadronic calorimeters, known as ZDCs, are located 17m upstream and downstream of the centre of the TPC along the nominal beam axis. They have a small acceptance ($\sim$ 2 mrad) and measure the spectator neutrons emitted from the breakup of the nuclear fragment. Tests were undertaken with the ZDCs using the NA49 setup at the SPS which showed that there is a strong correlation between neutron

energy and impact parameter [95]. It was found that the number of spectator nucleons varies from between 8 for small impact parameters, and 30 for large impact parameters. This means that all events were accompanied by neutrons measured in the two ZDCs in coincidence and therefore this can be used to trigger on real collisions as background events such as Coulomb dissociation of a single nucleus will not yield simultaneous neutrons in both ZDCs. In order to have some common measure of centrality, all RHIC experiments have two identically designed ZDCs associated with them. In year 1, a minimum bias trigger was used which only demanded a ZDC coincidence; that is a pulse in both ZDCs originating from the same bunch crossing.

An example of how the CTB and the ZDC can be used to trigger on events is represented in the left hand plot in Figure 5.6, which plots the multiplicity in the CTB against the signal in the ZDCs.

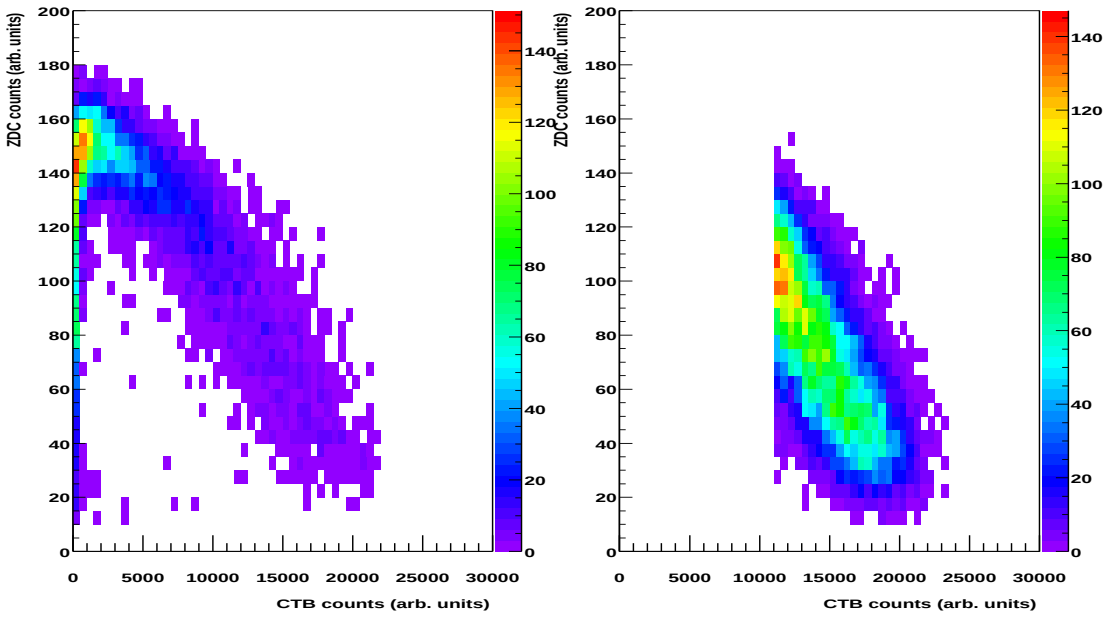

Figure 5.6: The CTB counts plotted vs the ZDC counts for the minimum bias trigger (left) and central trigger (right).

As one would expect, the higher the CTB multiplicity, the fewer the number of neutrons there are which are detected by the ZDC. However, at very low CTB multiplicity, where the beam fragments are more stable, neutron dissociation is less prominent which also leads to a small signal in the ZDCs. During year 1, a central trigger

was defined by simultaneously placing cuts on the CTB multiplicity as well as requiring a ZDC coincidence as shown in the right hand plot in Figure 5.6. This central trigger corresponded to the most central 14% of the hadronic cross-section.

5.2.2.5 The Trigger System

Due to the different time scales of the detectors involved in measuring an event, STAR employs a four level trigger system [91], which is operated in the following mode :

The trigger logic is activated by coincident ADC counts in the two ZDCs, together with information from the RHIC clock on bunch positions. A **Level 0** trigger is implemented to make decisions based on information processed from the CTB and the MWPC. This information can take the form of raw multiplicity as well as geometry of hits within the CTB. A decision has to be made on the event suitability within the bunch crossing time of 110ns, and is distributed to the rest of the STAR trigger electronics within 200ns of the collision.

The drift time of the TPC is 40μs, during which time a **Level 1** trigger makes decisions on whether or not to accept an event based on the measured location of the primary vertex. This location is determined by timing information from the Zero Degree Calorimeters as well as coarse information from the CTB. This helps guard against beam+gas interactions as well as beam+beam interactions that are not localised in the centre of the detector.

A **Level 2** trigger then adds additional summary data from other trigger detectors. A time limit of 8 ms is allowed for the Level 2 trigger which is based upon the digitizing time of the TPC. It allows a full processing of all the CTB data, as well as information coming from the Level 1 trigger. This allows more sophisticated decisions as to whether to accept an event or not to be made at this level. Due to a lack of processing power, the level 2 trigger was not implemented fully in year 1, and was not used to veto an event.

Finally, a **Level 3** trigger is able to make decisions within 10ms of an interaction occurring based on tracking information obtained from real-time software, an example of which is shown in Figure 5.7. The level 3 software algorithms can be used to trigger on the exact position of the primary vertex, as well as physics quantities such as the presence of particle jets, which are distinguishable by the presence

of high momentum tracks in the event.

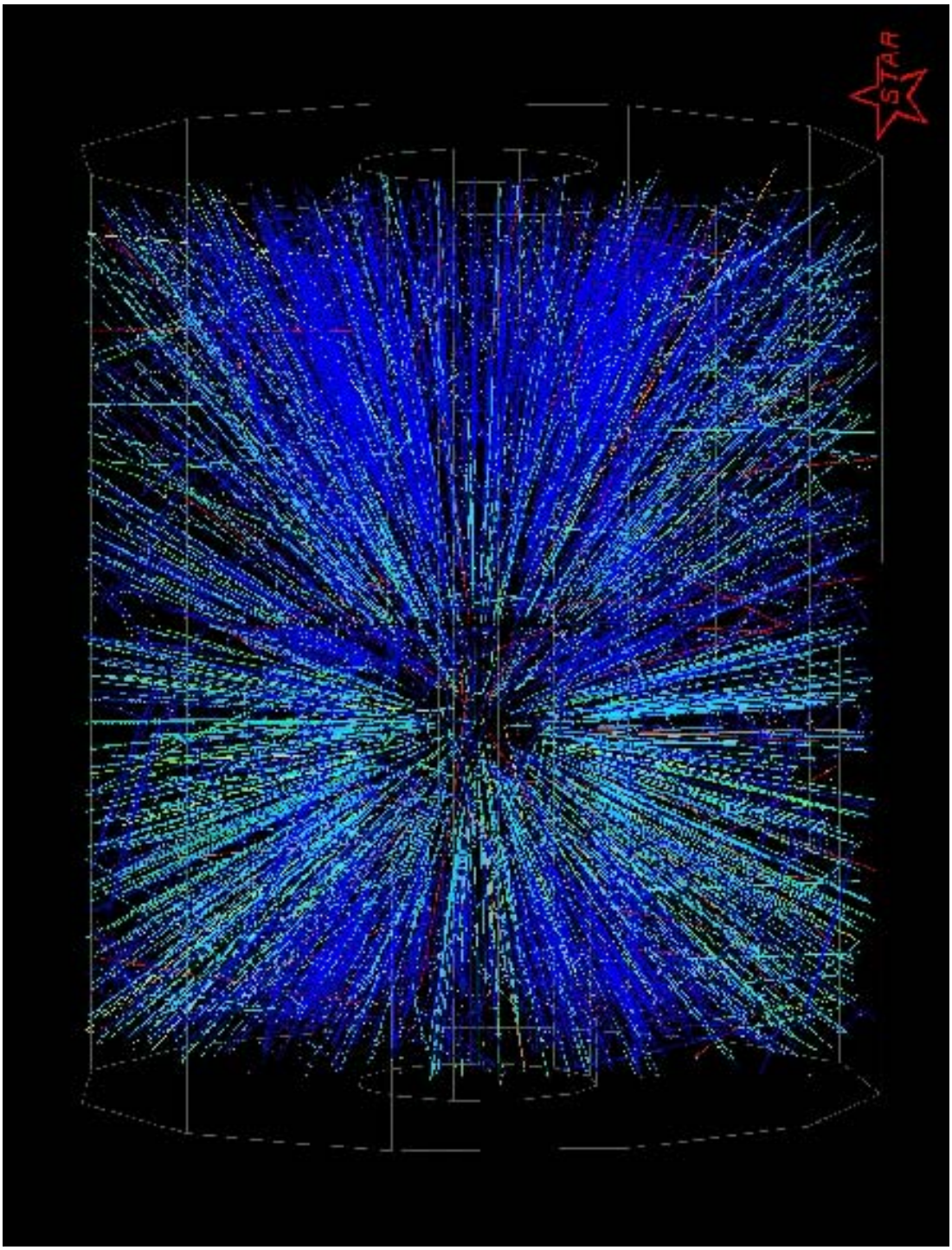

Figure 5.7: An event reconstructed with the L3 tracking algorithm, within 10 ms of an interaction occurring.

Chapter 6

Event Reconstruction

In order to extract meaningful physics from the raw data, the pixel information which is stored from each tracking detector must be 'converted' into reconstructed tracks. This is implemented with event reconstruction software, organised into a reconstruction chain. In year 1, where the only tracking detector was the TPC, the purpose of this software is to determine charge clusters in pad-time space and convert them into position co-ordinates in the TPC. Using this cluster information, pattern recognition software finds tracks which are in turn used to accurately determine the position of the beam interaction point (primary vertex). The tracks that are found at this stage are either secondary (from weak decays), or primary (produced in the collision, or from strong and electro-magnetic decays), so a re-fit of the tracks is undertaken, including the interaction point in the fit. This determines which tracks are primary using the selection criterion that the track must pass within 3 cm of the primary vertex. Two copies of each track are then kept, with and without the extra re-fit. The initial class of tracks which do not have a re-fit to the primary vertex are then used to reconstruct neutral strange particles (K^0_S, Λ and $\overline{\Lambda}$, referred to as V0s) via their charged daughters. These V0s are in turn used to find multiply strange 'Cascade' particles (Ξ^-, $\overline{\Xi^+}$, Ω^- and $\overline{\Omega^+}$), which decay via a Λ ($\overline{\Lambda}$) and another charged particle. The following sections describe this process in more detail.

6.1 Cluster Finding

As the charged hadrons traverse the TPC, they produce a continuous trail of ionisation which drifts and diffuses under the influence of the $\vec{E}$ and $\vec{B}$-fields. At the readout plane, charge is induced on a series of pads, which effectively turn the continuous stream of ionisation into discrete samples, referred to as hits. A track traveling through the whole of the TPC, can leave a maximum of 45 hits. As outlined in Section 5.2.1.1, each TPC sector contains 5690 pads, giving a total of $\sim$ 137,000 total readout pads. Each pad is then sampled 512 times (each sample known as a time bucket), which in total leads to $\sim$ 70 million total samples, or pixels.

The cluster finding is performed in a local co-ordinate system, where the radial direction, perpendicular to the pad-row is vertical and defined as the y axis, and the position along the pad-row is horizontal and defined as the x axis. A sequence is defined as a series of consecutive time buckets on a pad with ADC values above the readout threshold. A cluster is then a set of sequences on adjacent pads on a pad-row which have some overlap in time. An example of how a cluster is seen, in terms of pedestal corrected ADC values is shown in Figure 6.1. The distributions are then fit with a two dimensional Gaussian function to determine the centroid of the cluster along the pad-row and in the time direction. The centroid in the pad-row direction determines the x co-ordinate of the cluster while the centroid in the time direction determines the z co-ordinate of the cluster, where the z direction is along the drift axis. The y co-ordinate is simply defined as the centre of the pad-row in the y-direction.

6.1.1 Corrections to Cluster Position

The equation of motion of a charged particle moving in an $\vec{E}$ and $\vec{B}$ field is given by equation (6.1), referred to as the Langevin equation [96],

$$\vec{F} = m\frac{d\vec{v}}{dt} = q(\vec{E} + \vec{v} \times \vec{B}) + m\vec{A}(t) \tag{6.1}$$

where $\vec{E}$ is the electric field strength vector, $\vec{B}$ the magnetic field strength vector, q the charge of the particle, $\vec{v}$ the velocity vector of the particle and $\vec{A}$(t) is the stochastic deceleration of electrons with collisions with the gas. For a constant $\vec{E}$ field, the

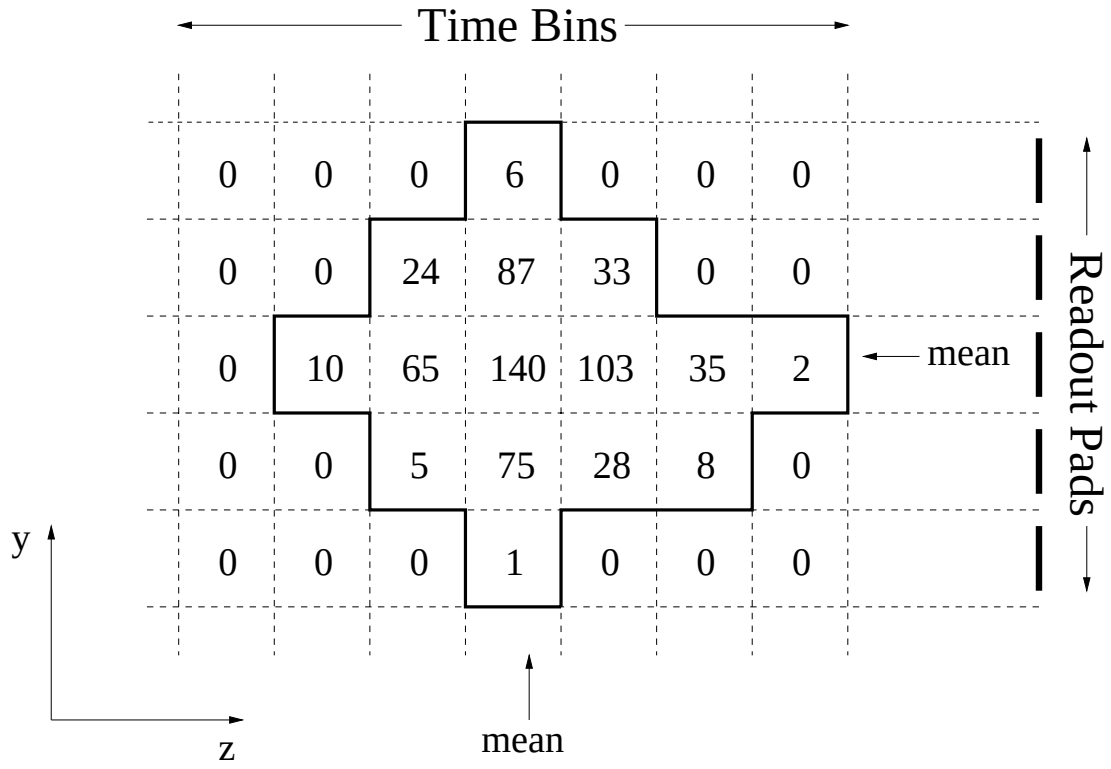

Figure 6.1: ADC counts in individual pixels making up sequences and a cluster, outlined with a solid line. The mean values are indicated on the figure, which lead to the x and z coordinate of the hit

combination of the electron acceleration and stochastic deceleration will lead to a constant drift velocity on average, for the whole cluster. Therefore the left hand side of equation (6.1) is zero, and substituting for $\vec{A}$(t) (= -$\vec{v}_D/\tau$, where $\vec{v}_D$ is the electron drift velocity and τ the mean time between collisions), gives

$$\frac{\vec{v}_D}{\tau} + \left(\frac{q\vec{B}}{m} \times \vec{v}_D \right) = \frac{q\vec{E}}{m} \tag{6.2}$$

The solution to equation (6.2) for $\vec{v}_D$ is then ([96])

$$\vec{v}_D = \frac{\mu}{1+\omega^2\tau^2} \left(\vec{E} + \frac{\vec{E}\times\vec{B}}{B}\omega\tau + \frac{(\vec{E}\cdot\vec{B})\vec{B}}{B^2}\omega^2\tau^2 \right) \tag{6.3}$$

where $\mu = q\tau/m$ is the electron mobility, and $\omega = -qB/m$ is the electron cyclotron frequency.

It is easily seen from equation (6.3) that in the case where the $\vec{E}$ and $\vec{B}$ fields are

parallel, the only contribution to the force exerted on the drifting electrons is in the direction of the $\vec{E}$ field, as $\vec{E} \times \vec{B} = 0$.

In actual fact, due to a slight misalignment of the TPC in the magnet and $\vec{B}$ field non-uniformities, the $\vec{E}$ and $\vec{B}$ fields are not completely parallel. The effect that this has on a particle trajectory is illustrated in Figure 6.2, which is not to scale. Without applying a correction, the measured hit would appear to come from a position directly in line with the pad, the distance determined by the drift velocity and drift time. The real position is determined from a measured field map of the detector, extrapolating the path of the charge back away from the anode wires, with the position determined again by knowledge of the drift velocity and drift time.

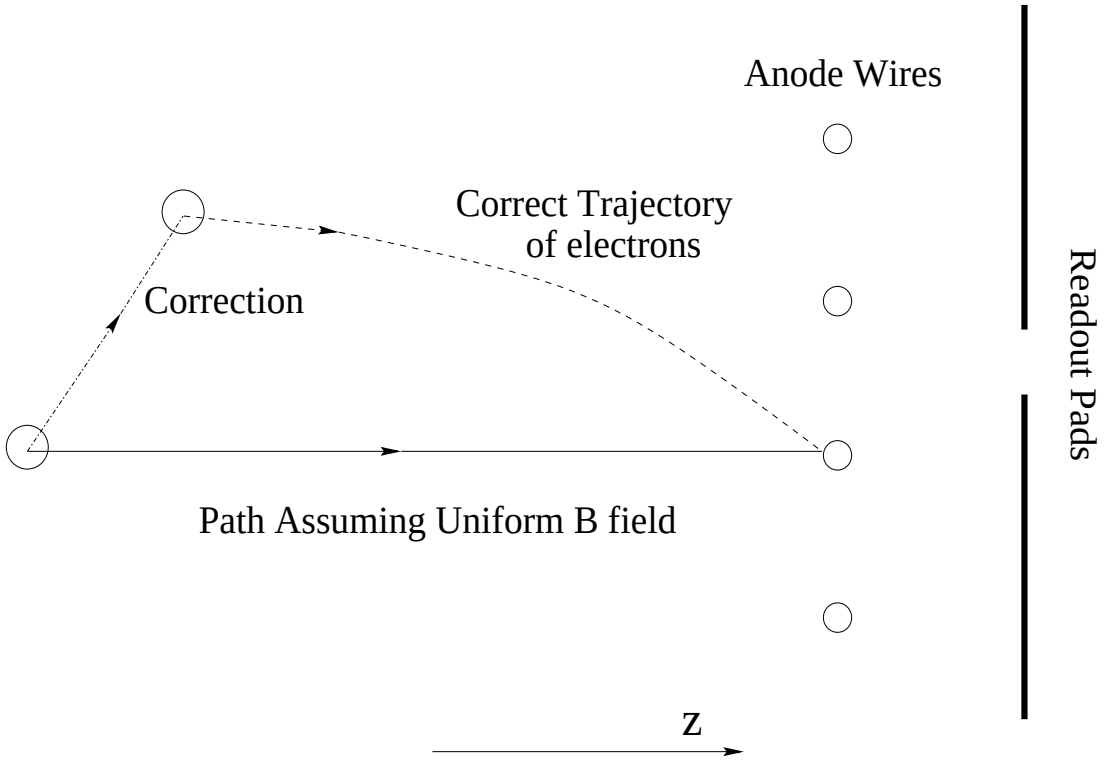

Figure 6.2: A schematic diagram showing the effect of the non-uniform magnetic field on the drift path of the electrons.

The largest value of the radial component of the B field is 40 Gauss, which is small compared to the value of the B field in the drift direction which is 2.5 kGauss (0.25 Tesla). This small non-uniformity leads to a maximum distortion of 1 mm for the measured hits, for a full 2m drift length. This is large when compared to the

spatial resolution of $\sim 100\ \mu$m. Although this value is small, not correcting for this effect can have a measurable effect on the momentum distributions of the measured particles.

Although the non-uniformity of the B field produces the largest deviation in the electron drift path, others have been found by plotting the residuals of the hits on a track, where the residual is defined as the distance between the actual position of the hit, and the tracks position on the pad-row. Figure 6.3 shows these residuals both before and after the corrections have been applied[1]. These processes include the non-uniformity of the $\vec{E}$ field at the termination on the anode wires, a small misalignment in the endcap magnet, a twist in the central membrane and a small misalignment between the inner and outer sectors.

6.2 Track Finding

Once the clusters positions have been corrected, their x,y and z coordinates are transformed to a global co-ordinate system and are used as hits by the TPC tracking package, where a hit represents a possible point on a track.

Tracking starts at the outermost pad-row of the TPC, where the hit density is lowest. Each point on the outer pad-row is considered to be the starting point of a track and is referred to as a root. Using an assumed position along the beam direction for the interaction vertex as a guide, 3 point links are formed between a root and hits on the adjacent pad-rows using linear extrapolation. From each starting point, several 3 point links can be formed. These links are then extended into segments by extrapolating as far as possible towards the innermost pad-rows, using linear extrapolation and the local slope of the track as a guide. Once this is completed, the longest track candidate is kept and its associated hits are removed from the hit collection. The next point on the outermost pad-row is then used as a root and this process repeats itself for all sectors. Once all of the hits in the outer pad-rows have been used, the process continues and proceeds to the inner pad-rows where new roots are formed, using the available hits still in the hit collection.

After all of the segments have been found, a helix model is applied to the segments. Each segment is extrapolated both towards and away from the assumed in-

[1] Figure compiled by S. Trentalange

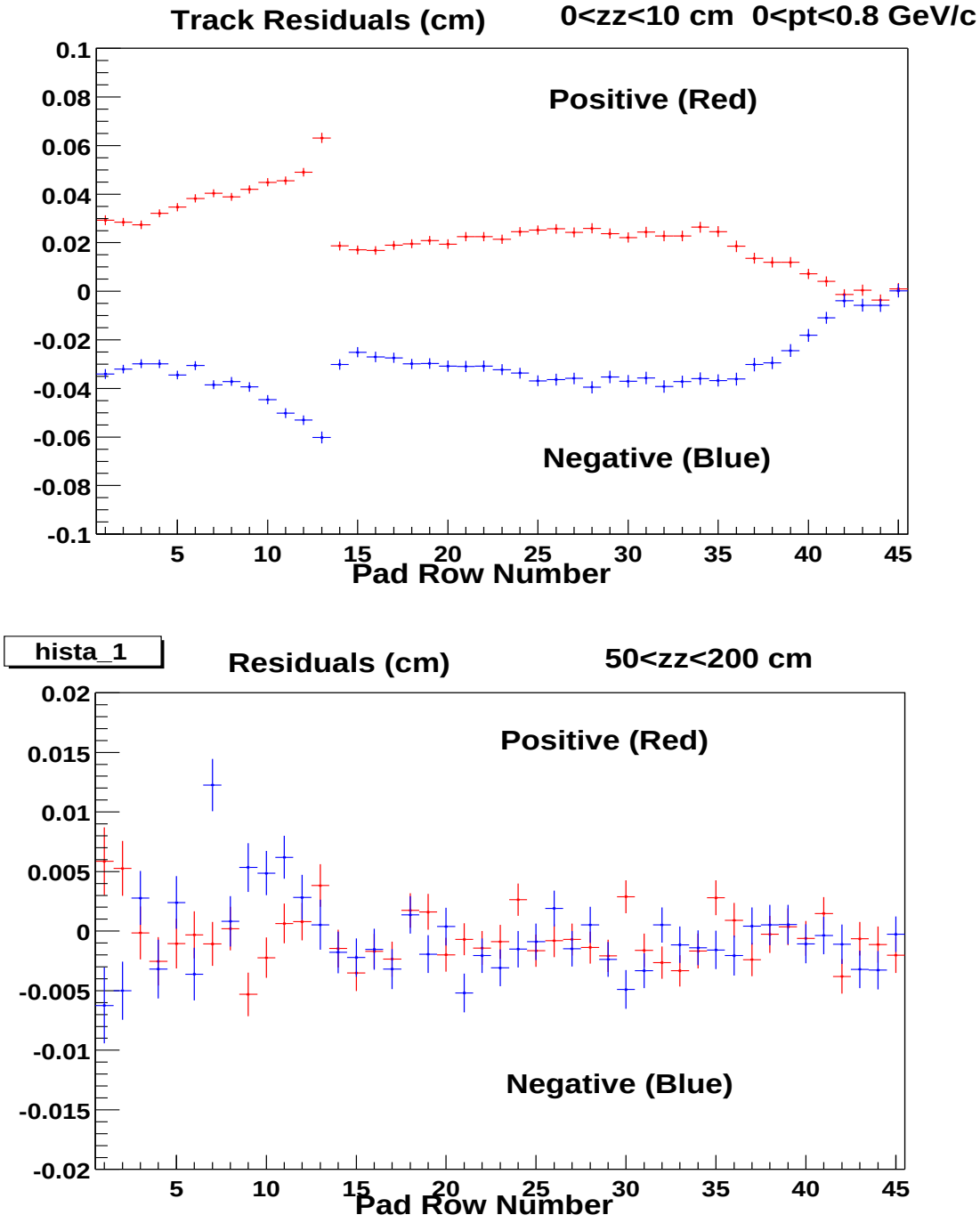

Figure 6.3: Residuals of hits on tracks within 10 cm of the central membrane and $p_t < 0.8$ GeV/c. Pad-rows 1 to 13 represent the inner sector, and 14 to 45 the outer sector. a) Residuals before the corrections are applied. b) Residuals after the corrections are applied.

teraction point, starting with the longest available segment. Hits are then added to the segment and removed from the hit collection if they fall within a specified distance of the helix and do not belong to another segment. For tracks with high transverse momentum ($\sim >$ 1 GeV/c), it is usually found that one segment will describe the whole track. For lower momentum tracks, whose curvature is much greater, it is likely that the track will be split into several segments. At this point, the process of helix merging is performed, which compares the helix parameters from different segments. If the parameters agree within specified thresholds, the segments are merged to form one track. In order for a track to be said to be found, it must have a minimum of 5 hits, otherwise the hits are returned to the hit pool.

Due to the radius of the active volume of the TPC, and the minimum number of hits requirement, the TPC can measure tracks with $p_t >$ 75 MeV/c in year 1 (B = 0.25 Tesla), and tracks with $p_t >$ 75 MeV/c when the magnetic field is a maximum (B = 0.25 Tesla).

6.2.1 Global track fitting - The Kalman Filter

Once the tracks have been found, they are then fit using a Kalman Filter approach [97]. This is more realistic than a simple helix fit as it takes into account multiple scattering and energy loss in the inner field cage and the gas inside the TPC in each step of the fitting routine, in order to obtain the best estimate of the track momentum. This approach requires three passes through the data. The first pass, known as filtering, starts at the outermost pad-row and works its way in, removing hits from the track that fail very crude cuts, known as outliers. The second pass, referred to as smoothing, starts at the innermost radius and works its way outwards. Again, outliers are removed from the track but this time the rejection cuts are much harsher. The third pass is for the evaluation of the track parameters and the total χ^2.

In order to estimate the degree of multiple scattering and energy loss, an estimate of the mass of the particle must be used. This is accomplished by assuming that all particles are pions. This is true for approximately 70-80% of tracks, but the effect of using an incorrect mass hypothesis should only be non-negligible for very low momentum kaons and protons. Although it is desirable to fit every track (or at

least a subset of tracks) with other mass hypotheses, this was not performed in the first year reconstruction as the process is extremely CPU intensive.

6.2.2 Primary Vertex Reconstruction

An accurate knowledge of the interaction position (primary vertex) for each collision is required as this helps distinguish between tracks which originate from the primary vertex (primary tracks) and those from weak decays, as well as tracks created via interactions with the detector material (secondary tracks). The primary vertex co-ordinates can also be included in a track re-fit for primary tracks (determined via a selection on their distance of closest approach (DCA) to the primary vertex) which leads to a better determination of their momentum.

In order to calculate the primary vertex position, a rough first estimate of its co-ordinates is needed. All tracks are extrapolated to a point where they have a DCA to the STAR beam-line with an offset of 0.5cm in the x and y directions. The value of 0.5cm in the x and y directions were determined by preliminary event reconstruction to be the nominal beam position in the STAR co-ordinate system, a value which will change from year to year. The z value of the track DCAs is binned in intervals of 0.5 cm and after all the tracks have been extrapolated, the z bin with the highest occupancy is used as a seed in the primary vertex determination. Using this seed, the primary vertex position is found by minimizing the sum of the DCAs of the global tracks. Although most of the tracks in an event are primary, the secondary tracks distort the DCA distribution so an outlier rejection method is used to remove these. After several iterations, using a least-squares method to minimise the DCA values, a primary vertex is found.

Using the additional information of the primary vertex position as an extra point on the track, the tracks are re-fit with a helix model, using the primary vertex as a fitting constraint. Therefore after the tracking and primary vertex reconstruction processes have finished, there remain two copies of each track. One copy contains the information from the Kalman fit to the track only and are known as $global$ tracks, while the second copy contains the information from the second helix fit and are known as $primary$ tracks. For data taken in the run in the autumn of 2001, a Kalman Fitter approach for tracks is applied to both the global and the primary tracks.

During the first year of running, the interaction position of the beam in STAR was not well tuned and primary vertices were reconstructed over the full 4m range in z, as shown in Figure 6.4. However, studies with Monte Carlo generated events have shown that the primary vertex is found to within $\pm$ 200 μm of its actual position, for all z positions and centralities.

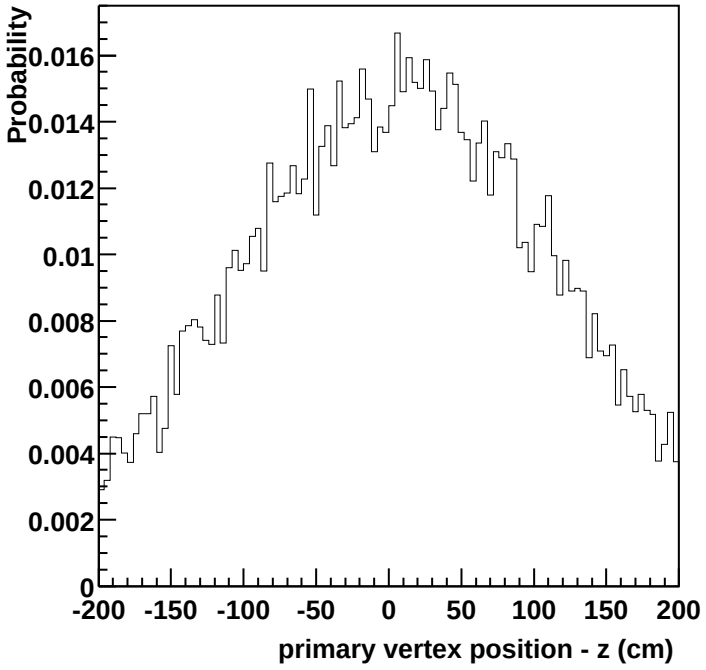

Figure 6.4: Primary vertex distribution along the beam axis from the first year of data-taking.

6.3 V0 Reconstruction

The next part of the reconstruction chain is the V0 finder, which searches for neutral strange particle decays. A V0 is the collective term for the $|S|$ = 1 neutral strange particles (the K^0_S, Λ and $\overline{\Lambda}$), whose properties are outlined in Table 6.1. They have a charge of zero and have a dominant weak decay branch into a final state of two oppositely charged daughters. The term 'V0' originates from the topology of the decays, which were first observed in bubble chamber experiments.

Due to their mean lifetime being small, the majority of V0s decay before they

Particle	Quark Content	Mass (GeV)	Dominant Decay Mode	$c\tau$ (cm)
Λ	uds	1.116	$p + \pi^-$: $\sim$ 64 %	7.89
$\overline{\Lambda}$	$\overline{u}\overline{d}\overline{s}$	1.116	$\overline{p} + \pi^+$: $\sim$ 64 %	7.89
K^0_S	$\frac{1}{\sqrt{2}}\lvert d\overline{s} + \overline{d}s\rvert$	0.498	$\pi^+ + \pi^-$: $\sim$ 69 %	2.68

Table 6.1: The properties of the V0 particles, showing quark content, mass, dominant decay mode and mean lifetime multiplied by the speed of light

reach the tracking volume of the TPC (radius = 50 cm). Moreover, as the V0s are charge neutral, they do not ionise the gas in the TPC, therefore they cannot be detected directly. A V0 therefore has to be reconstructed from its charged daughter particles. By definition, the V0 daughters are secondary tracks, so the global track collection is used. A schematic diagram of a V0 decay is given in Figure 6.5.

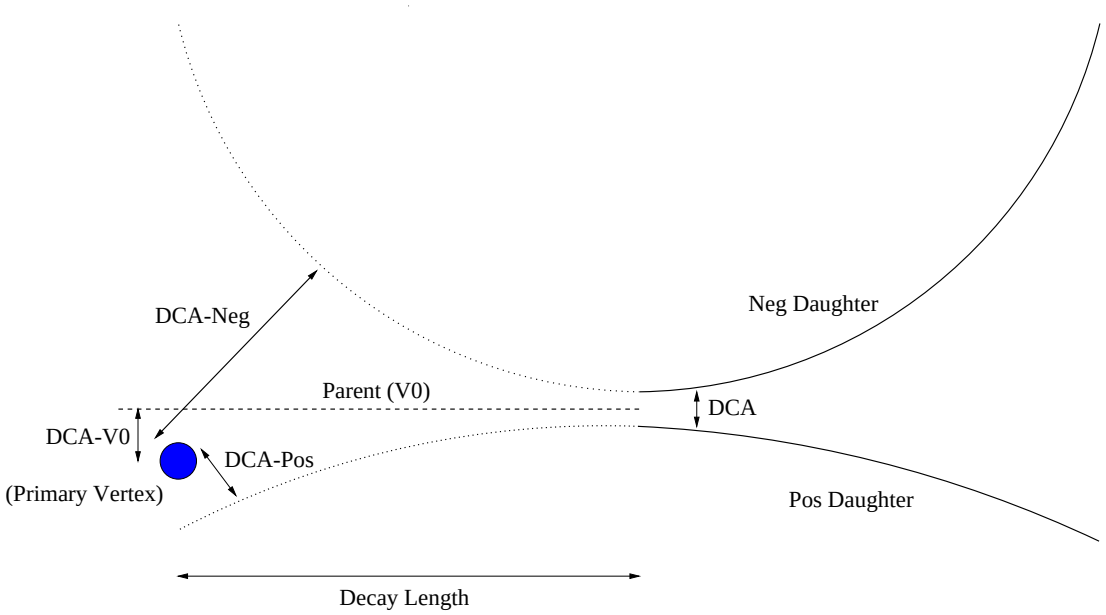

Figure 6.5: A schematic representation of a V0 decay and associated parameters.

The general principle behind V0 reconstruction is to consider all tracks in each event that do not originate from the primary vertex. All of the positive tracks are paired with all of the negative tracks in the event, and are extrapolated towards the primary vertex. A cut is placed on their distance of closest approach in co-ordinate space (DCA) which determines whether they originated from a common point. For

candidates passing the DCA cut, the momentum of the parent can be calculated from the momentum of the daughters using vector addition. A final check is made to see that the momentum of the parent is consistent with having originated from the primary vertex.

Cut Description	Value
Number of hits in the TPC	> 10
DCA of daughter tracks to Primary Vertex	> 0.7 cm
DCA between V0 and Primary Vertex	< 0.8 cm
DCA between daughters at decay vertex	< 0.8 cm
Decay Length of V0	> 2.0 cm

Table 6.2: The cuts applied to V0 candidates whilst conducting the V0 reconstruction in the production chain.

However, in each event there are thousands of particles from the primary vertex that do not point back there exactly due to finite momentum resolution. As the tracks originate at the primary vertex, they may randomly cross with other primary tracks and form fake secondary vertices, which is known as combinatorial background. In order to minimise this background and reduce the size of the data volume, cuts on various quantities are made. These cuts are placed where the background is largest but still need to be tuned further (see Chapter 7). Strict cuts are not applied at this stage as they may impinge upon different analyses. The cuts that are applied in the finding stage are outlined in Table 6.2 which includes extra cuts to the ones mentioned earlier in this section. These additional cuts are explained below :

i) The minimum number of hits on a track is 5, so a requirement that greater than 10 hits are on a track is used in this stage to try and minimise the contributions from split tracks, where a split track is one track in the TPC which for some reason has been reconstructed as two separate tracks. This usually occurs if there is a gap in the track path.

ii) As the majority of the tracks in the event do come from the primary vertex, and these make up the majority of the combinatorial background, then the majority of the track crossings occur close to the primary vertex. For this reason, a cut on

the decay distance of the V0 from the primary vertex of greater than 2 cm is also applied. As the V0s decay distance distribution has an exponential fall off from 0, this cut reduces the signal by quite a bit, but the background is reduced even more.

iii) As the daughter tracks do not necessarily originate from the primary vertex, an effective cut to differentiate between the signal and the background is to require that the tracks do not point back to the primary vertex.

Figure 6.6 shows plots of the cut variables plotted against the mass of the Λ, for 1000 events from the centrally triggered dataset. Each plot is evidently still dominated by background candidates.

After the V0 reconstruction has finished, the reconstruction chain then moves on to the Cascade finder. A Cascade is a term for multiply strange baryons which decay weakly into a V0 and another particle, hence their generic name also comes from their decay topology. The Cascade finder operates in essentially the same way as the V0 finder, where this time one of the decay particles is a V0. In this way, the V0 information is used to reconstruct the multiply strange particles which can be detected in STAR (Ξ^-, $\overline{\Xi}^+$, Ω^- and $\overline{\Omega}^+$) which decay into a $\Lambda(\overline{\Lambda})$ and either a $\pi^-(\pi^+)$ or a $K^-(K^+)$.

6.4 DSTs and MicroDSTs

Once the event reconstruction has taken place, all of the track and vertex data is written to a Data Summary Tape (DST), which is a collection of C++ classes. The DSTs are split into chunks of approximately 130 events as each file is large ($\sim$ 500 MBytes) by this stage. Due to the hundreds of thousands of events that are recorded, it is impractical to read through these large files time and again. To this end, a set of MicroDSTs are created, extracting the information required for a V0 analysis only. The strangeness MicroDST is again a set of C++ classes which means that only a small amount of data needs to be stored in the data file, such as the momentum of the daughters and the decay vertex co-ordinates. Indeed, the same 130 events which take up $\sim$ 500 MBytes in the DST only occupy $\sim$ 2.5 MBytes of MicroDST space.

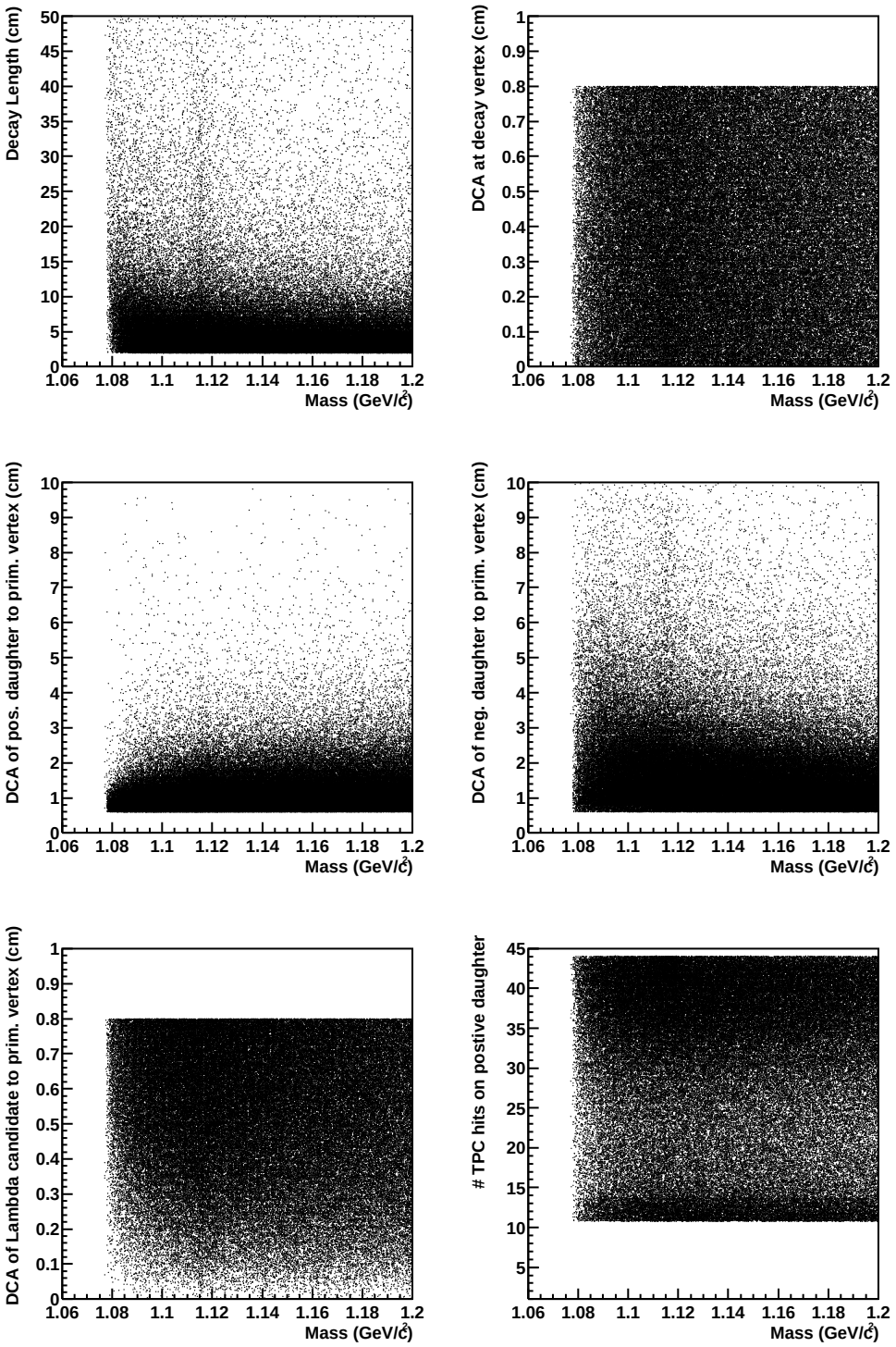

Figure 6.6: Initial values of the cut variables for Λ candidates, plotted versus the Λ mass, from 1000 events from the central dataset. This shows that a large background remains.

Chapter 7

Analysis

The principle aim of this analysis is to measure the $\overline{\Lambda}/\Lambda$ ratio, as well as the average yields of Λ, $\overline{\Lambda}$ and K^0_S produced in an event, as a function of rapidity (**y**), transverse momentum (p_t) (or transverse mass (m_t)) and centrality. These measurements carry important information on the relative amount of strangeness production as well as the amount of baryon stopping achieved in a collision. Both the ratio and corrected yields and inverse slopes will be presented as a function of centrality of the collision in Chapter 8. The analysis steps taken in order to achieve the final results will now be described in detail.

7.1 Dataset

A problem that occurs in colliders is that the position of the interaction vertex is not the same for each and every collision as was shown in Figure 6.4. In the dataset analysed, in order that the phase space measured by the detector was kept as uniform as possible while still yielding high enough statistics, a cut on the z of the primary vertex position was placed so that only events whose primary vertex in the beam (z) direction was within $\pm$ 75 cm of the central membrane (defined as z=0) were considered. This limits the event sample under consideration to approximately half of the total number of events that were triggered on.

As a result of this cut, the dataset under consideration for the analysis in this thesis corresponds to 180,496 centrally triggered Au+Au collisions, and 250,396 events taken with the minimum bias trigger, with a found primary vertex. The central

trigger, as it was defined in Section 5.2.2, corresponded to the top 14% of the total hadronic cross-section, while the minimum bias trigger accepted most hadronic interactions.

7.2 Cut Tuning

The first step in the analysis process is extracting the raw Λ, $\overline{\Lambda}$ and K^0_S signal. Whilst the initial cuts applied in the V0 finding stage, outlined in Table 6.2, cut down on the number of background candidates, the amount of combinatorial background is still large as observed in Figure 6.6. This level of background becomes apparent when plotting the mass of the particle, which is calculated by invoking the conservation of energy and momentum in the decay process as given in equation (7.1),

$$M^2_{V0} = M^2_1 + M^2_2 - 2(E_1E_2 - \vec{p_1}.\vec{p_2}) \tag{7.1}$$

where the subscript V0 refers to the mass of the V0 'parent' particle, and the subscripts 1 and 2 refer to the decay products, or 'daughter' particles. The masses of the K^0_S, Λ and $\overline{\Lambda}$ are calculated in turn, by assuming different identities for the daughter particles, whose energies are calculated from their mass and their measured momenta, using equation (7.2).

$$E^2 = p^2 + M^2 \tag{7.2}$$

Figure 7.1 shows the calculated masses for the Λ, $\overline{\Lambda}$ and K^0_S respectively, for ten thousand events from the centrally triggered dataset, using only the cuts applied in the V0 finding stage. This shows that although mass peaks are visible at the correct masses, the background is still large and dominates the plot.

The method used to extract raw yields for the strange particles is to sum the number of entries in each of the mass peaks. For the distributions in Figure 7.1, even though these peaks could be fit by a function and the yield extracted, the large amount of background leads to a large uncertainty in the yield. For this reason, tighter cuts are needed to reduce the background level further. Whilst the cuts reduce the number of background candidates, they inevitably also reduce the signal, so the aim of the cuts is to optimise the signal to background ratio, whilst leaving as

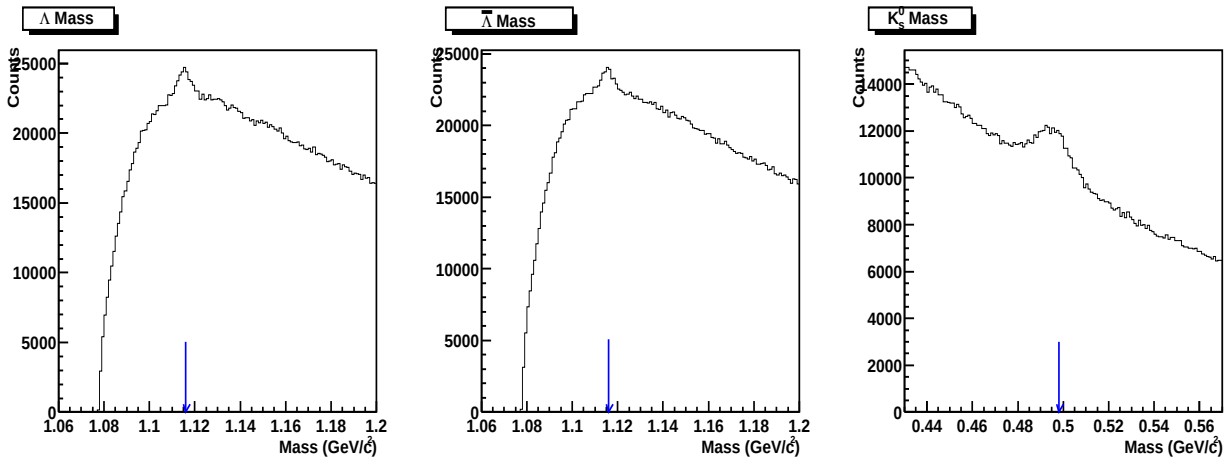

Figure 7.1: Λ, $\overline{\Lambda}$ and K^0_S mass distributions using only the cuts employed in the reconstruction chain. The arrows represent the correct value of the mass in each case, taken from the particle data book [2].

much of the signal as possible. This is desirable as the candidates that are removed by the cuts at this stage will have to be corrected for at a later stage and the more candidates that can be kept at this stage will minimise these correction factors.

The first stage of cut optimisation was the implementation of particle identification cuts based upon the specific energy loss of the particles due to their interactions with the gas in the TPC.

7.2.1 Particle Identification

As the particles traverse the TPC, they lose energy via electro-magnetic interactions with the constituent gas, by the process of ionisation. The energy loss is parameterised by the $Bethe$-$Bloch$ formula given in equation (7.3),

$$-\frac{dE}{dx} = \frac{e^2\,(Ze)^2\,n_e}{4\pi\,\epsilon_0^2\,m_e c^2\beta^2}\left[\ln\left(\frac{2m_e c^2\beta^2\gamma^2}{I}\right) - \ln\left(1-\beta^2\right) - \beta^2\right] \tag{7.3}$$

where m_e is the mass of the electron, e its charge, Ze is the charge of the hadron in units of electron charge, and n_e and I are the number of electrons per unit volume and the average ionisation energy of the material. Although this parameterisation doesn't explicitly rely on the mass of the particle, it can be shown that $\beta\gamma = p/mc$,

where p and m are the momentum and mass of the hadron, and c is the speed of light. Therefore, although the specific energy loss is the same at a constant value of $\beta\gamma$ for particles of different masses, it will be different for the same value of momentum.

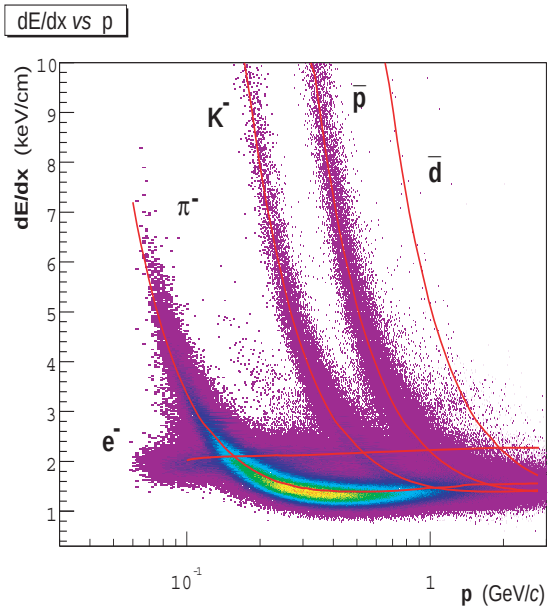

Figure 7.2: The measured dE/dx of all negative particles in the TPC.

Figure 7.2, taken from [98], shows the measured dE/dx value for different negatively charged particles in the STAR TPC. The expected values for the specific energy loss for the different negatively charged particles (electrons (e^-), pions (pi^-), kaons (K^-), anti-protons ($\overline{p}$) and anti-deuterons ($\overline{d}$)) as a function of momenta are represented by lines on the plot. It is evident from this plot that reasonable particle species separation can be achieved up to a momentum of approximately 1 GeV/c.

Particle identification becomes important when conducting a V0 analysis due to the large combinatorial background levels. In the cases of the Λ and $\overline{\Lambda}$, a lot of the background comes from π^- and π^+, the most abundant particles produced in the collision, being misidentified as p and $\overline{p}$. Therefore a cut on the dE/dx values of the daughter particles can reduce this contribution significantly. Figure 7.3a) shows the measured dE/dx values for the positive V0 daughter for all candidates. Figure 7.3b) shows the same plot but where a cut on the dE/dx of the positive daughter being within 5σ of the expected value for a proton, obtained from the $Bethe$-$Bloch$ formula, has been applied. There is still some background for particles which have a momen-

tum greater than approximately 400 MeV/c, and at $\sim$ 700 MeV/c, the proton band becomes indistinguishable from the pion band, however as the $<p_t>$ of the pions is much less than that of the protons, the ratio of protons to pions increases at higher momenta.

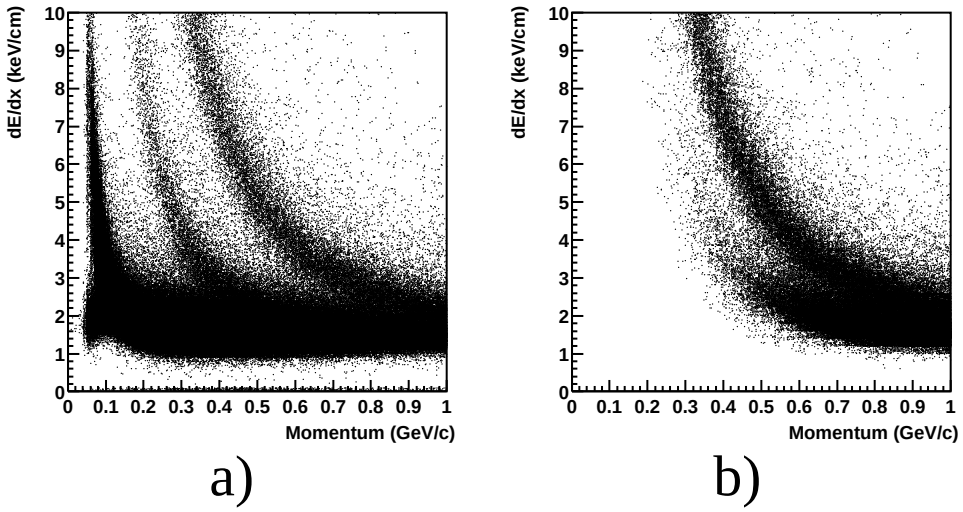

a) b)

Figure 7.3: The measured dE/dx values for positive V0 daughter: a) Before a cut is placed, b) After a 5σ cut on the expected proton dE/dx has been made.

If a cut of 5σ is placed on both the positive and negative daughter for the Λ, $\overline{\Lambda}$ and K^0_S respectively, then the mass plots in Figure 7.4 are obtained. The K^0_S mass doesn't show much improvement to the one presented in Figure 7.1 as the combinatorial background coming from pions is much greater than the background contribution coming from protons which are mis-identified as pions, but there are significant improvements for both the Λ and $\overline{\Lambda}$.

Although the signal to noise ratio has now increased for the Λ and $\overline{\Lambda}$, the background still peaks under the Λ and $\overline{\Lambda}$ mass peaks. Therefore, the background still needs to be reduced even further so that it is flatter, which eases the background subtraction procedure. To this end, tighter cuts need to be applied on the geometry of each candidate.

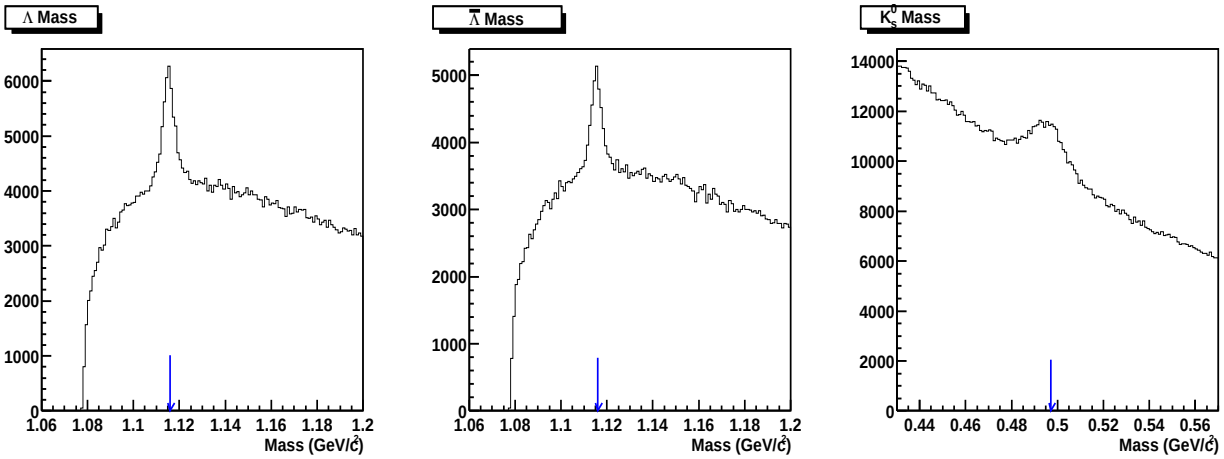

Figure 7.4: Masses of the Λ, $\overline{\Lambda}$ and K^0_s respectively, after dE/dx cuts have been applied.

7.2.2 Geometrical Cuts

The geometrical cuts that are used to define a V0 decay were presented in Figure 6.5 and explained in section 6.3.

The best way that was found to optimise the initial cut values, listed in Table 6.2 was to plot 2 dimensional 'dot plots' of the particular cut under investigation, on one axis, and the mass of the parent particle on the other. An example of this method is given in Figure 7.5, which shows a two dimensional plot of the Λ mass plotted against the distance of its decay, or decay length.

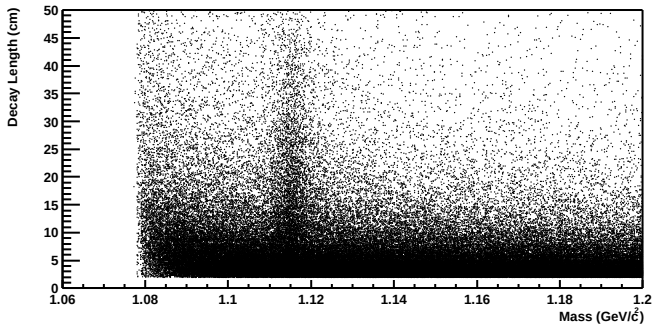

Figure 7.5: Decay length of the Λ candidates, plotted versus their mass.

From Figure 7.5, it can be seen that the majority of the background comes at values of the Λ decay length below 10cm. It would therefore seem desirable to place

a cut on the decay length being greater than 10 cm, or even 15cm. However, a cut at these values would also reduce the signal by a large amount. The best way to reduce this background even further is to place cuts on different quantities. As the cuts are often related (e.g., a small DCA of a daughter track to the primary vertex implies a small decay length), the final cut values are obtained via a systematic process of tuning the cuts. This involves considering each cut in turn and adjusting the cut value to find the optimum value whilst keeping all other cuts constant. This process continues for all of the cuts involved and the process is iterated on until the final values are found. Table 7.1 outlines the final values of the cut variables for each of the K^0_S, Λ and $\overline{\Lambda}$ respectively.

Cut Description	Initial Value	K^0_S	Λ	$\overline{\Lambda}$
Number of hits in the TPC	> 10	> 15	> 15	> 15
DCA of Negative daughter to Primary Vertex	> 0.7 cm	> 1.3 cm	> 2.5 cm	> 1.05 cm
DCA of Positive daughter to Primary Vertex	> 0.7 cm	> 1.3 cm	> 1.05 cm	> 2.5 cm
DCA between V0 and Primary Vertex	< 0.8 cm	< 0.6 cm	< 0.5 cm	< 0.5 cm
DCA between Daughters	< 0.8 cm	< 0.8 cm	< 0.8 cm	< 0.8 cm
Decay length of V0	> 2.0 cm	> 6.0 cm	> 6.0 cm	> 6.0 cm
Particle Identification on daughters	No	Yes	Yes	Yes

Table 7.1: The final cuts applied to K^0_S, Λ and $\overline{\Lambda}$ candidates.

Figure 7.6 shows the cuts plotted against the mass of the Λ, where all other cuts apart from the quantity plotted have been applied and the value chosen for the cut is indicated by a blue horizontal line on the plot.

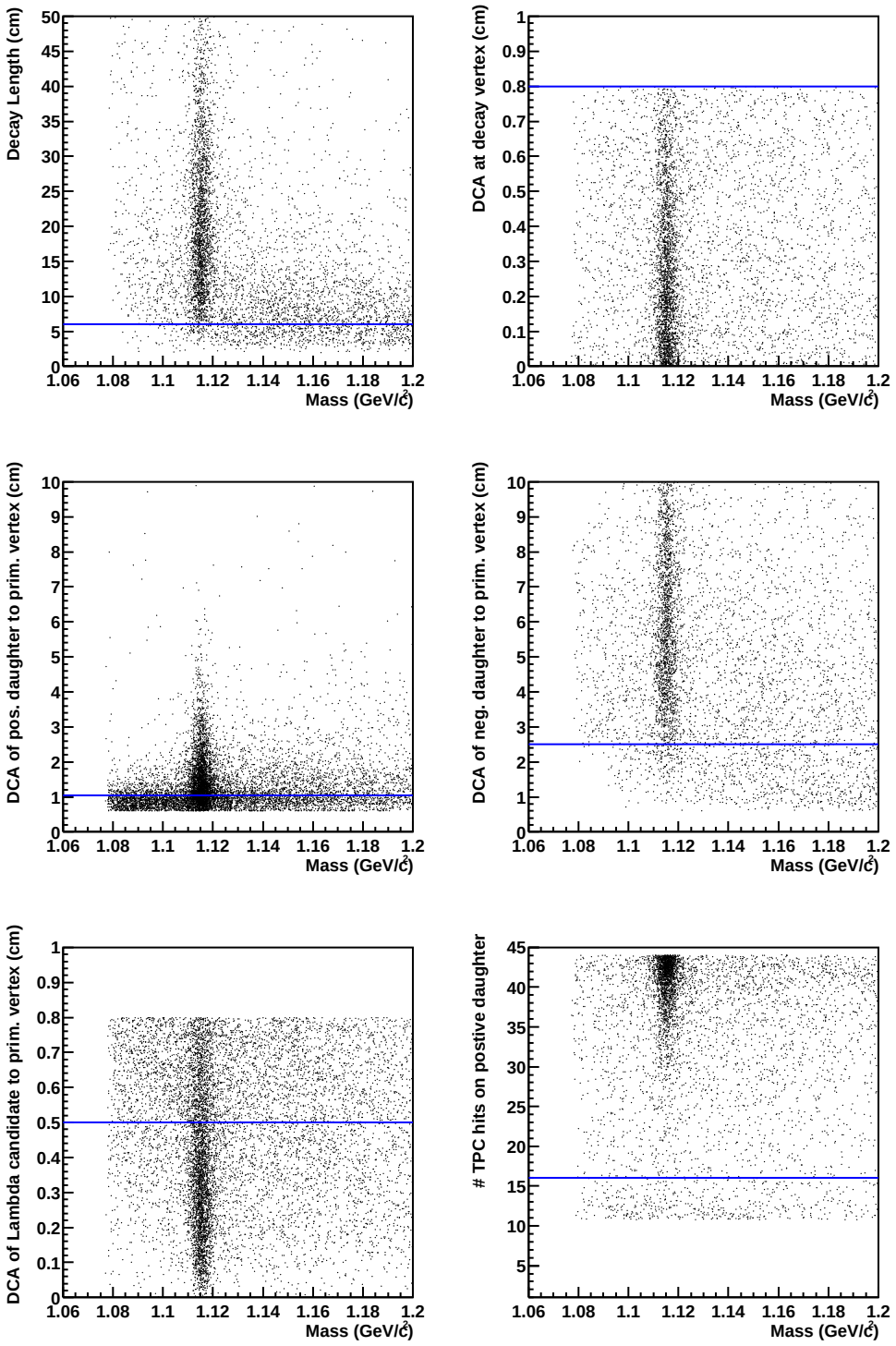

Figure 7.6: Final distributions of the cut variables for Λ candidates. Comparison of these with Figure 6.6 shows the large background suppression that has been achieved.

The mass plots shown in Figure 7.7 are then obtained after the application of these cuts and are for the same 10000 events that were investigated in Figures 7.1 and 7.4. The signal-to-noise ratio is now large ($\sim$ 5:1) and the yields can be reliably extracted from the background using linear extrapolation.

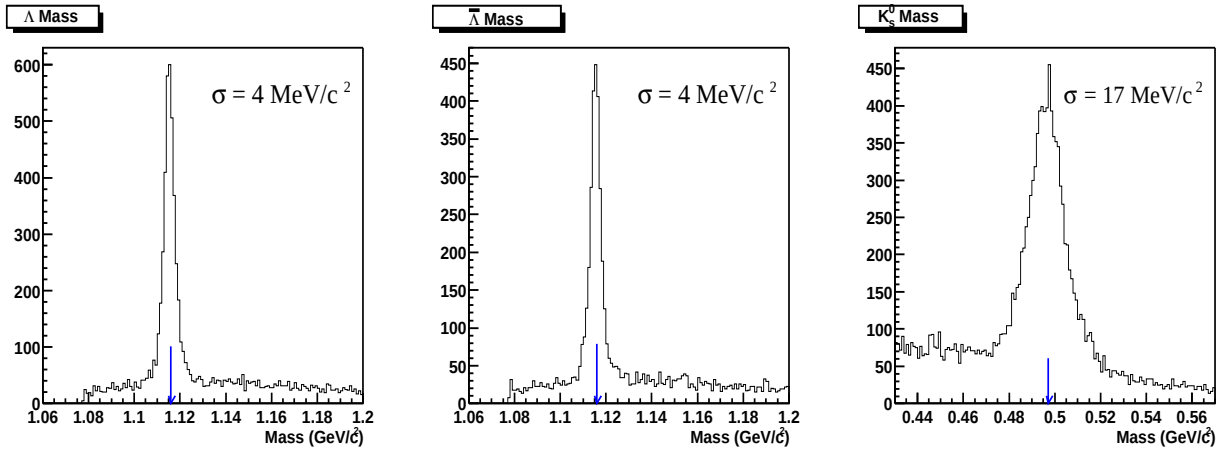

Figure 7.7: Masses after the particle identification and optimised geometrical cuts have been applied.

7.3 Determining the Raw Particle Yields

In order to extract the raw particle yields, the number of counts in the mass peaks must be determined. There are several ways of doing this, by fitting the peak with different functional forms, as well as summing the entries in each of the bins under the mass peak.

7.3.1 Fitting the Mass Peaks

In order to extract the yield from the fit, then the function which is used must describe not only the signal well, but also the background it sits on. As a result of the cuts that are applied, the background is linear and this makes fitting the signal and background easier. Both single and double Gaussian functions have been used to describe the signal, while a second order polynomial was used to describe the background. The fitting procedures were accomplished using the C++ based ROOT package [99].

7.3.1.1 Gaussian Fits

As the V0s decay weakly, they have relatively long lifetimes with respect to resonances and their natural line width is very small. Therefore any width in the mass peak comes from experimental resolution effects. The resolution is a function of p_t, but in small enough p_t slice these contributions are uniform and the width of the mass peaks could be of the form of a Gaussian distribution. Figure 7.8 shows a fit to the Λ and K^0_S mass peak for 50000 events of the form given in equation (7.4), which represents a Gaussian function plus a second order polynomial, in order to describe the peak and the background respectively, where A, σ and μ are the area, width and mean of the Gaussian respectively, and a,b and c are the parameters of the polynomial.

$$f = \frac{A}{\sigma\sqrt{2\pi}} e^{-\frac{(x-\mu)^2}{2\sigma^2}} + a + bx + cx^2 \tag{7.4}$$

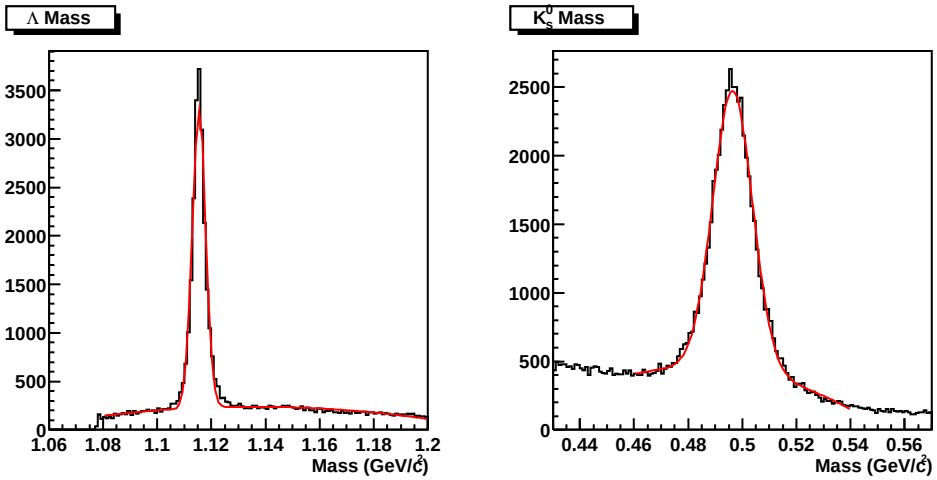

Figure 7.8: Gaussian plus polynomial fit to Λ (left) and K^0_s (right) mass peaks

The figure shows that the Gaussian plus polynomial fit describes the K^0_S peak well (χ^2/dof $\sim$ 2.7), but does not do a very good job for the Λ (χ^2/dof $\sim$ 5). In the case of the Λ, there are clear differences between the data and the fit function in the tails of the distribution, as well as (most notably) in the amplitude of the peak. Therefore, the Gaussian plus polynomial fit can be used to describe the K^0_S data, but another function must be used to describe the Λ distribution.

A solution that was attempted in the case of the Λ was to fit the peak with a double Gaussian plus polynomial, of the form given in equation (7.5),

$$f = \frac{A_1}{\sigma_1\sqrt{2\pi}} e^{-\frac{(x-\mu)^2}{2\sigma_1^2}} + \frac{A_2}{\sigma_2\sqrt{2\pi}} e^{-\frac{(x-\mu)^2}{2\sigma_2^2}} + a + bx + cx^2 \tag{7.5}$$

where A_1, σ_1, A_2 and σ_2 are the areas and widths of the first and second Gaussians respectively, and μ is the common mean for each function. As shown in Figure 7.9, there is excellent agreement between the fitted function and the data (χ^2/dof $\sim$ 2).

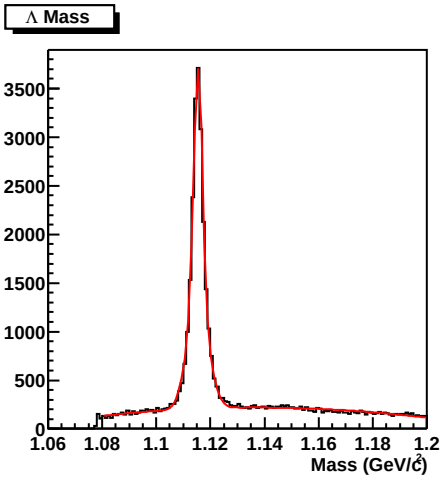

Figure 7.9: Double Gaussian plus polynomial fit to Λ mass peak

Although the data and function shown in Figure 7.9 are in good agreement, it was found that when splitting the data into discrete p_t and centrality slices that this was not always the case and varied between each mass histogram. For bins where there were only a few hundred counts in the mass peak, above the background level, it was found that the fit would fail. Also, the error in the area obtained for the fit was very large, much larger than for the single Gaussian functions and due to these reasons, another method was investigated.

7.3.2 Bin Counting

Another way to obtain the yield is by simply summing the number of counts in the peak. As some background underneath the peak remains, by simply summing the entries in the histogram between two limits, the background is also being counted in the yield. However, in the case where the background is linear in shape, by simply

subtracting the background values from either side of the peak, in such a way that the total range of the background subtraction is equal to the range under the peak, then the background can be properly accounted for. This makes the assumption that there is no shape change in the background under the mass peak, which should be the case. An example of how this works is shown in Figure 7.10, which is again for 50000 events.

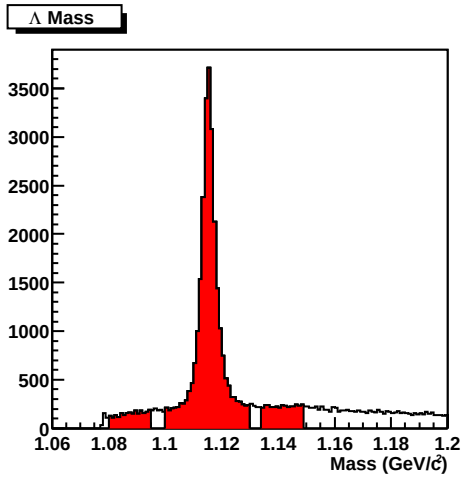

Figure 7.10: A Λ mass distribution indicating the ranges used in the bin counting method.

The peak region is chosen to be 30 MeV/c^2 in width, whilst the two background regions are 15 MeV/c^2. It was found that even though the width of the peak increases with momentum, the 30 MeV/c window that was chosen sufficed in all cases.

Table 7.2 shows the yield calculated using the different methods outlined, for the same 50000 events.

Function	Yield
Single Gaussian	19197.5 ± 151.0
Double Gaussian	20292.4 ± 1123.6
Bin Counting	20733.0 ± 180.5

Table 7.2: The raw Λ yield for 50000 events evaluated using different fitting methods.

It was therefore decided to use the single Gaussian function to fit the K^0_S data and the bin counting method for the Λ and $\overline{\Lambda}$ data. An additional benefit of the bin counting

method is that it is reliable in the limit of low statistics, where a fit may fail, as long as the background is linear in shape. The differences that occur when using the different yield subtraction methods is used later to estimate the systematic error.

7.3.3 Phase-space Coverage

Once the raw yields have been reliably extracted, the phase space coverage of the raw data can be calculated. Figure 7.11 shows the y-p_t coverage for the Λ and K^0_S, where the $\overline{\Lambda}$ coverage is not shown as this is the same as for the Λ. This shows that for all particles, the data that pass the cuts are concentrated between $\mid y \mid < 1$ and $p_t < 2$ GeV/c. The different shapes of the distributions at low p_t is dominated by the acceptance of the detector.

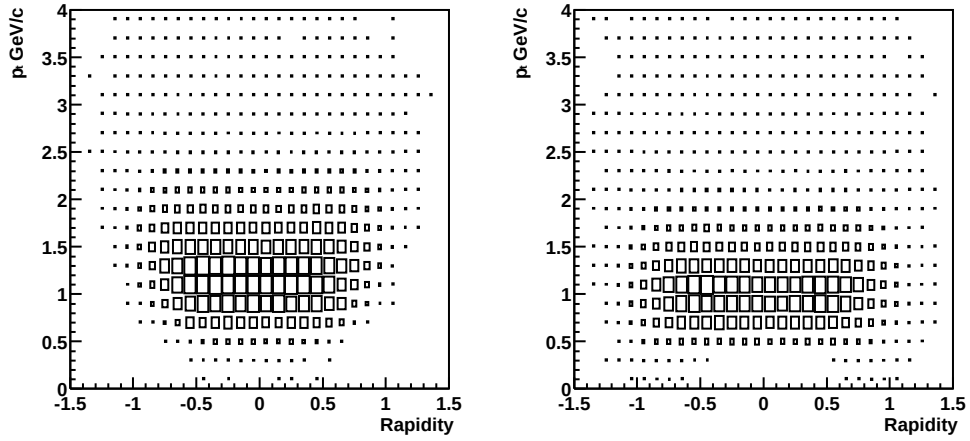

Figure 7.11: Phase space coverage for Λ (left) and K^0_S (right), in terms of p_t and rapidity, the larger the box, the greater the occupancy in that bin.

In order for the coverage, or acceptance, to be constant as a function of rapidity, all analyses, except where specifically investigating rapidity distributions, are conducted between the rapidity interval -0.5 $<$ y $<$ 0.5

7.4 Corrections

The main aim of this thesis is to measure the yields and spectra of $\overline{\Lambda}$, Λ and K^0_S particles in the collisions under investigation. However, the number of particles that

are measured experimentally are not the total number that are produced in the collision, and this has to be corrected for by applying correction factors to the measured yields. These factors are commonly separated into two distinct groups, referred to as geometrical acceptance and reconstruction efficiency. The acceptance correction is required for particles that are not able to be reconstructed because either the daughters do not actually make it into the detector, the particle decayed via another decay mode not under consideration, or because the candidates fail the geometrical cuts. The reconstruction efficiency is required for particles that do pass the acceptance cuts, but are not reconstructed properly for a variety of reasons (such as only one daughter is reconstructed, or both daughters are reconstructed but are not formed into V0 candidates).

The correction factors are determined using Monte-Carlo (MC) based techniques. MC particles are generated, propagated and decayed in the experimental setup. This propagation is achieved by using the GEANT simulation program, which uses known cross-sections to determine the interactions of the generated particles with other MC particles, as well as with detector material [100]. Once this process has occurred, a detail TPC response program simulates the physical processes that occur within the TPC and generates output in the same format as the raw data.

Both of these corrections have been obtained via the process of embedding MC particles into real events. This is done so as to best simulate the conditions of a real event (such as particle multiplicity and $<p_t>$), as the efficiency correction is the efficiency of finding a particle in such an event.

7.4.1 The Embedding Chain

The embedding chain is a process which involves the generation of the MC particles, their simulation in the TPC, and then finally the event reconstruction and an association process that occurs between the MC and reconstruction information.

The MC particles are generated by the GENTX program, which takes as input the vertex position and particle multiplicity of each raw event, the rapidity and p_t ranges of the particles that are required, as well as the inverse slope parameter that will be used to generate the p_t distributions of the generated particles. The primary vertex co-ordinates of the real event that is being embedded into are required so that

the generated particles and the real particles all originate from the same vertex. This is an important consideration because, in order to calculate the efficiencies, all of the final cuts need to be applied to the data, which include cuts on the distance of closest approach of both the parent and daughter particles to the primary vertex. So as not to perturb the overall characteristics of the event, there is a limit on the number of particles that are embedded. For $\overline{\Lambda}$, Λ and K^0_S, the multiplicity of particles to embed was chosen to be 10% of the event multiplicity, which turned out to be an increase in the track multiplicity in the TPC of 6%, as not all generated particles are accepted. A test was carried out whereby only 5% of the event multiplicity was embedded, and no differences were observed in the results. The inverse slope parameter is the 'T' parameter in the Hagedorn formula (equation 2.3), which describes particles momentum distributions. Although the required rapidity and p_t ranges were determined from their coverage in the raw data, the inverse slope parameter required for input is one of the quantities being investigated, so it is not an a priori known quantity. As the correction is done on a bin-by-bin basis in terms of p_t, it is not necessary that the MC and the real data have the same momentum distributions. However, if the distributions are similar, then the relative statistics in each bin are approximately the same, whereas if the MC particles were embedded flat in p_t, then the errors due to the MC in each bin would not be representative of the errors due to the data. A good estimate for this parameter can be extracted from previous results at different energies, as well as from preliminary results for other particle species at the energy under investigation.

GENTX generates three momentum vectors (p_x, p_y and p_z) according to a thermal distribution for each particle originating from the pre-determined primary vertex position, which are confined by the rapidity and p_t limits that are chosen as input. The output from GENTX is then used as input by the GEANT program, running within a STAR specific framework, which then propagates and decays the generated particles. The GEANT setup contains precise information on the detector geometries, as well as the amount of the material in the detectors, and detector support structures as well as the value of the magnetic field. The GEANT program then propagates the MC particles, using the momentum vectors from GENTX. The particles are then decayed accordingly, and their daughters are then tracked through the TPC. The amount of ionisation created with interactions in the gas is also deter-

mined by GEANT, which depends upon the momentum of the track as well as the ionisation potential of the gas (equation (7.3)). As the embedding process is very CPU intensive, in order to increase the statistics, the branching ratios of the generated particles were redefined so that they would decay 100% of the time into the system under investigation. This is corrected for as part of the overall correction factor.

Once the particles have been fully propagated through the detector, the transport of the ionisation electrons from their generation to the read-out plane has to be modeled. This task is done by the TPC Response Simulation package (TRS), which also models the charge collection, as well as the analogue and digital signal generation. In order for the correction factors to be correct, the simulation must be accurate so that the properties of the reconstructed MC particles are the same as those of the raw reconstructed particles.

After TRS has run, the embedding is then performed by taking a real event, and by adding the ADC counts obtained from the simulated particles with the ADC counts from the raw data in each pad-time bin. The new embedded event is then run through the reconstruction chain in almost the same mode as for the real data. The only difference is that the distortion corrections are not applied, as there are no distortions in the MC data. Although this now means that the real data part of the event will not be exactly the same as the raw data reconstructed with the distortion corrections, this does not matter as the raw data in the event is only used as background, and is therefore not used explicitly in the acceptance or efficiency calculations. The MC information is saved to the DST for every event, and this information is used when calculating the values of the acceptance and efficiency corrections.

7.4.2 Acceptance Correction

The acceptance correction is determined using only the MC information from the embedded particles, where the acceptance (A(y, p_t)) is defined as the ratio of the number of particles that pass the geometrical cuts (Acc(y, p_t)), to the number that are generated (Gen(y, p_t)).

$$\mathrm{A}(\mathrm{y}, p_t) = \frac{\mathrm{Acc}(\mathrm{y}, p_t)}{\mathrm{Gen}(\mathrm{y}, p_t)} \tag{7.6}$$

The only caveat in this procedure is that the number of TPC hits cut cannot be modeled exactly. In the real data, a hit may not be assigned to the track on a given padrow due to the finite resolution in the tracking. Therefore a track which physically crosses 15 padrows, may, for instance, only have 14 assigned hits. In the acceptance correction, the assumption is made that every pad that the track crosses contributes a hit. This means that the boundary between the acceptance correction and the efficiency correction can not be exactly defined. This has no bearing on the final correction factor however which is just defined as the acceptance*efficiency. The acceptance is calculated as a function of y and p_t, upon which it is strongly dependent, although unlike the efficiency correction, it is independent of the centrality of the collision. This is because it is not dependent on the other tracks in the event. Figure 7.12 shows the acceptance for the K^0_S, Λ and $\overline{\Lambda}$ as a function of p_t in the range |y |<0.5. It indicates that at low p_t, the acceptance is very low for all particles, but it then continues to increase to a level of approximately 65$\%$ in the measured p_t range, for all 3 particles.

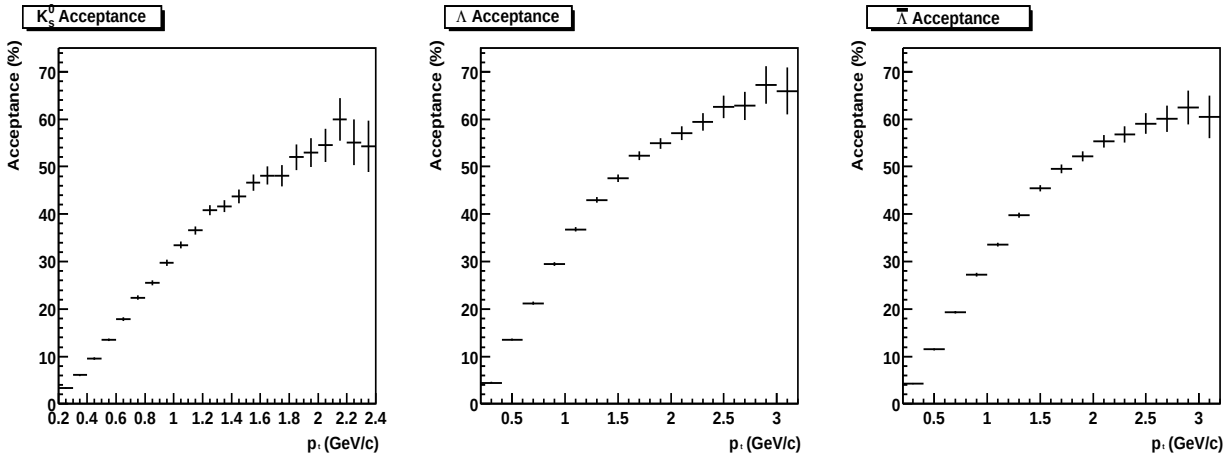

Figure 7.12: The geometrical acceptances of the K^0_S, Λ and $\overline{\Lambda}$ respectively.

This is the expected behaviour of the acceptance, as low p_t particles do not actually enter the TPC active volume due to their curvature in the magnetic field, and by definition fail the acceptance cuts. The acceptances for the Λ and $\overline{\Lambda}$, as expected due to the charge symmetry of the TPC, are very similar and there is only a small difference in the acceptance of the K^0_S, which is slightly lower than that of the Λ and $\overline{\Lambda}$.

7.4.3 Efficiency Correction

Whereas the calculation of the acceptance correction only involves the MC information of the embedded particles, the efficiency correction requires knowledge of both the MC and reconstructed information. To enable this process, a matching process is performed between the MC and reconstructed data, in order to associate the reconstruction information of each reconstructed embedded particle with its MC information.

The matching process is initially performed at the hit level, where a reconstructed hit is said to be matched if it falls within 5mm of a MC hit (see Table 7.3). The tolerance is the same in all three co-ordinates, which compares with the hit resolution which is approximately 1mm in all three co-ordinates. After the hit matching procedure has been performed, track matching is carried out. This requires at least three matched (or common) hits between the MC and reconstructed tracks before the tracks are labelled as matched.

Matching Level	Requirements
Hit	$\lvert\text{Reconstructed}_{x,y,z}$ - $\text{MC}_{x,y,z}\rvert < 5$ mm
Track	≥ 3 matched hits
V0	both tracks are matched to tracks generated from the same decay

Table 7.3: The requirements for an associated track.

While it appears that the requirement that there must be at least 3 (out of a maximum of 45) common hits before a track is said to be matched is small, in practice, due to the minimum of 15 hits on a track cut in the real data, the number of common hits on a track is much more than this. This is shown in Figure 7.13 which outlines the fraction of matched hits on a track to the total number of hits, for both the positive and negative tracks in the case of the Λ, normalised to unity. As both distributions are essentially zero below 0.5, no two reconstructed tracks are matched with the same MC track are would form 2 reconstructed Λ from a single MC Λ.

After the track matching is performed, the only requirement for a MC and reconstructed V0 to be matched is that both of the daughter tracks are matched to tracks

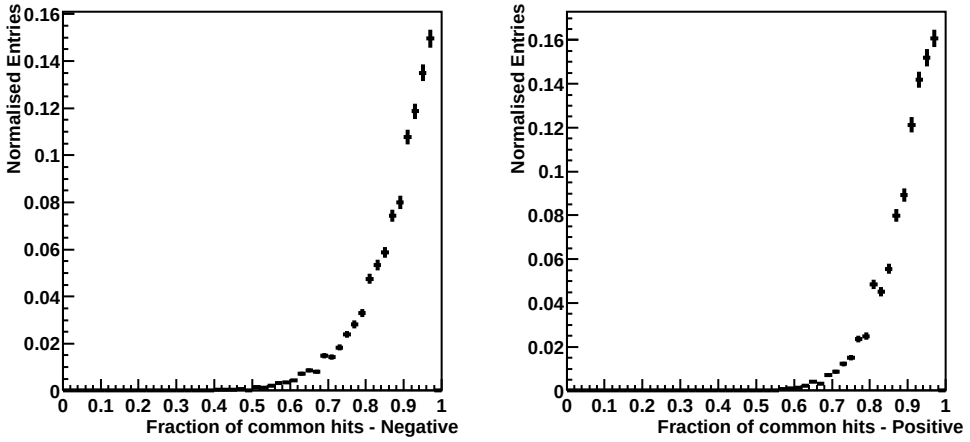

Figure 7.13: The fraction of the number of matched hits on a track divided by the number of reconstructed hits, for both the negative and positive daughters of the Λ

which are generated from the same decay vertex, again outlined in Table 7.3.

Once the association process has been carried out, the efficiency (E(y, p_t, mult) can be calculated, which is defined as the ratio of the particles that are reconstructed (Rec(y, p_t, mult)) to the number of particles that are accepted (Acc(y, p_t)).

$$\mathrm{E}(\mathrm{y}, p_t, \mathrm{mult}) = \frac{\mathrm{Rec}(\mathrm{y}, p_t, \mathrm{mult})}{\mathrm{Acc}(\mathrm{y}, p_t)} \tag{7.7}$$

The efficiency is calculated as a function of y and p_t for the various centrality bins, and it is strongly dependent on all three variables. Figures 7.14-7.16 show the efficiency as a function of p_t for the K^0_S, Λ and $\overline{\Lambda}$ for all of the centrality bins under study (defined in Table 8.1), in the range $|\mathrm{y}|<0.5$.

As can be clearly seen, the efficiency in all centrality bins is dependent on the p_t, which for low p_t Λ, shows approximately the same behaviour as the acceptance. The shape of the efficiency distributions is approximately independent of the centrality for each particle. As expected, the efficiency decreases with increasing centrality, where it is more difficult to reconstruct a V0 in a high multiplicity environment. In the centrality range measured, the efficiency varies by approximately a factor of two. At its best possible value, the efficiency for finding a V0 is the square of the single track reconstruction efficiency. Studies have shown that for single particles (in this case π^-), the value of the efficiency, once the plateau has been reached at $p_t \sim 0.4$ GeV/c, varies between $\sim 95\%$ for the least central events, and $\sim 80\%$ for the most

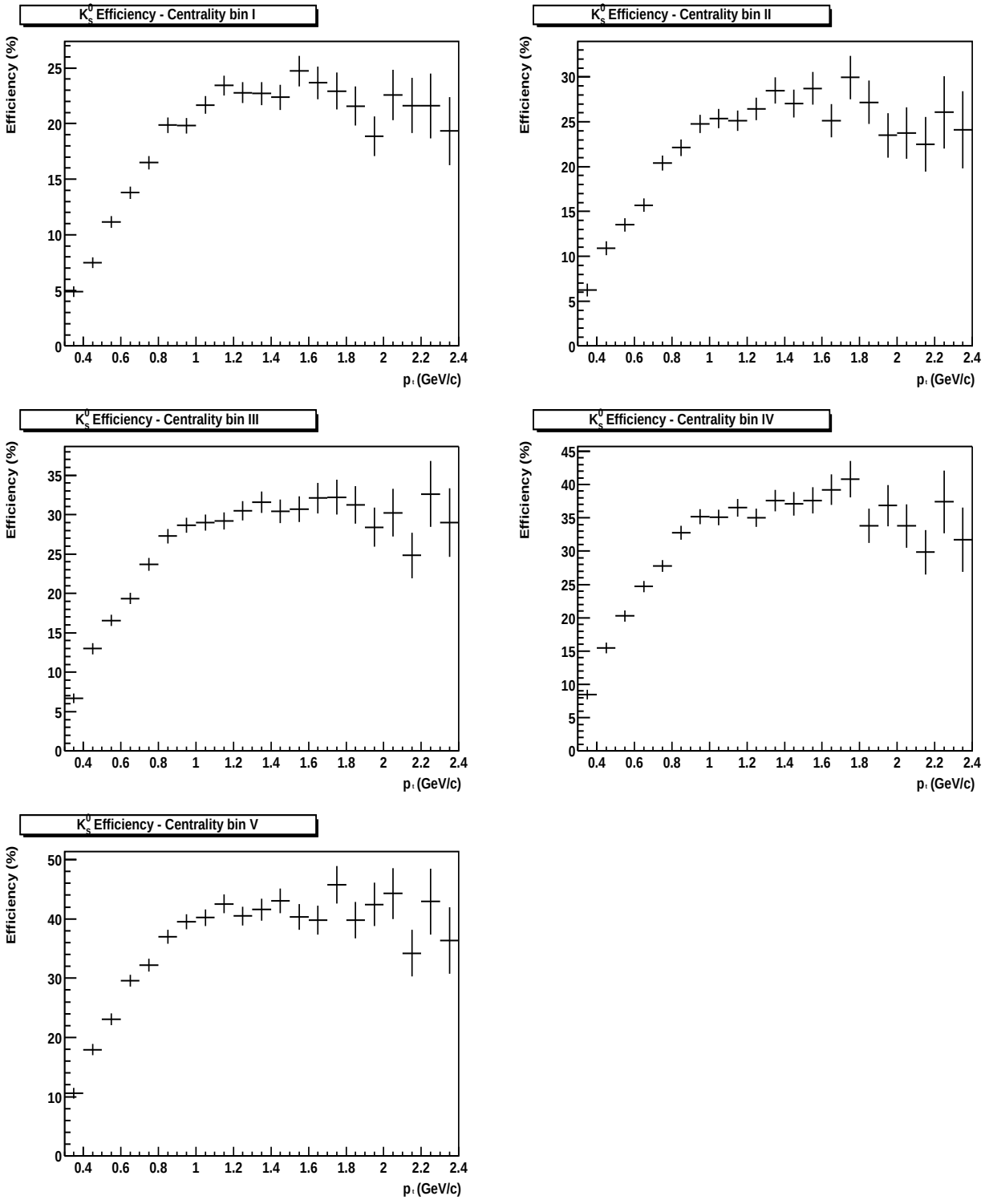

Figure 7.14: The efficiency of finding a K^0_S as a function of collision centrality. Bin I represents the most central collisions, Bin V represents the least central collisions.

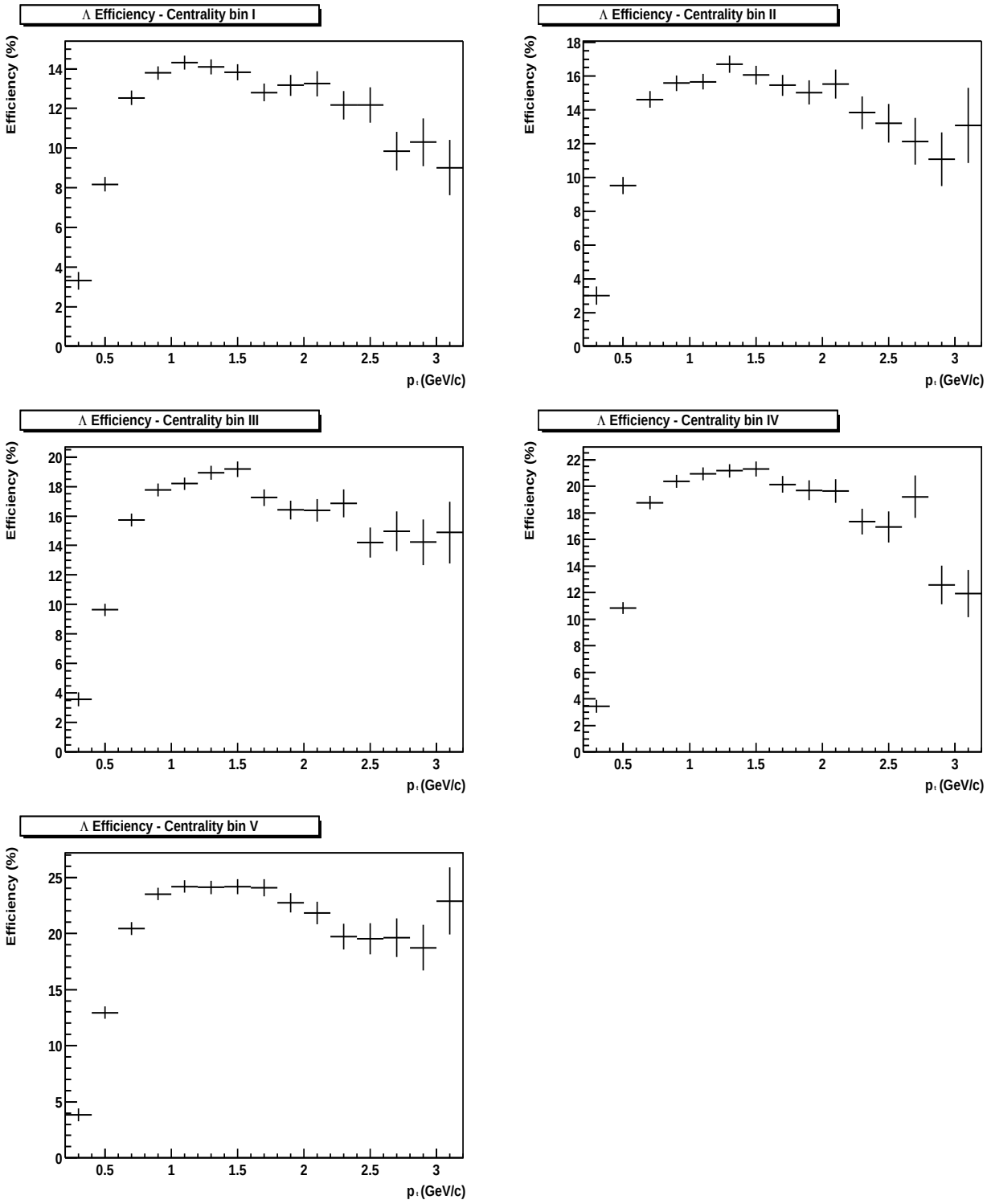

Figure 7.15: The efficiency of finding a Λ as a function of collision centrality. Bin I represents the most central collisions, Bin V represents the least central collisions.

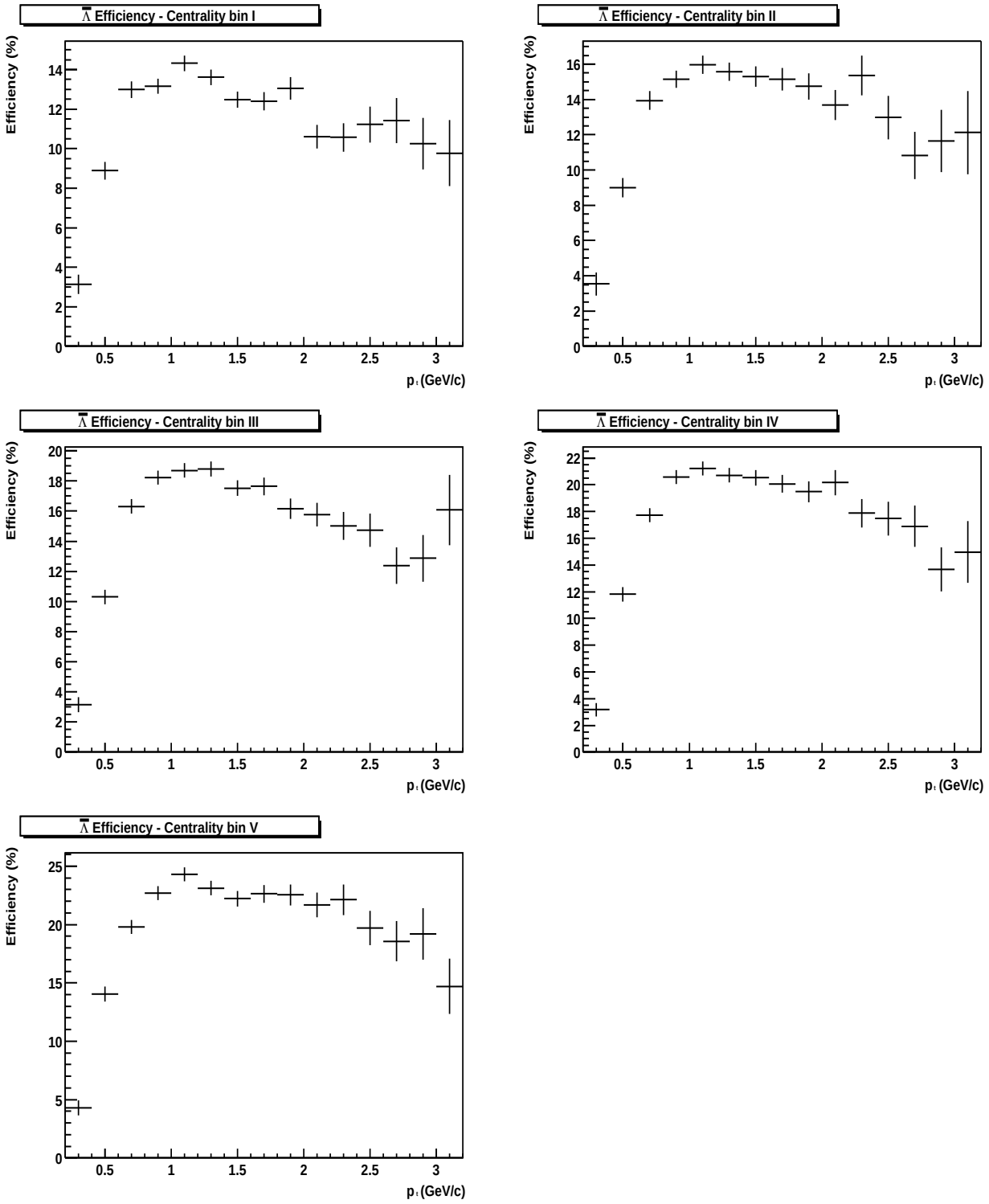

Figure 7.16: The efficiency of finding an $\overline{\Lambda}$ as a function of collision centrality. Bin I represents the most central collisions, Bin V represents the least central collisions.

central events [98]. The K^0_S, Λ and $\overline{\Lambda}$ efficiencies, however, are clearly lower than the square of the single track efficiency, and this is due to the efficiency of forming a K^0_S, Λ or $\overline{\Lambda}$ candidate, even though both of the daughter tracks have been reconstructed. This V0 finding efficiency is not 100% due to the cuts that are applied to reduce the background levels.

7.4.4 Total Correction

The total correction applied to the raw yields combines both the acceptance and the efficiency corrections. However, as the branching ratio (br) of each decay was redefined to be 100% in the embedding process, this has also to be corrected for. Therefore, the total correction factor (C(y, p_t, mult) is outlined in equation 7.8.

$$\begin{aligned} \mathrm{C}(\mathrm{y}, p_t, \mathrm{mult}) &= \frac{\mathrm{Acc}(\mathrm{y}, p_t)}{\mathrm{Gen}(\mathrm{y}, p_t)} \times \frac{\mathrm{Rec}(\mathrm{y}, p_t, \mathrm{mult})}{\mathrm{Acc}(\mathrm{y}, p_t)} \times br \\ &= \mathrm{A}(\mathrm{y}, p_t) \times \mathrm{E}(\mathrm{y}, p_t, \mathrm{mult}) \times br \end{aligned} \tag{7.8}$$

The values of this correction for the K^0_S, Λ and $\overline{\Lambda}$, plotted in each of the different centrality bins and as a function of p_t, are outlined in Figures 7.17-7.19, and are again in the range $|\mathrm{y}|<0.5$.

Approximately 180,000 minimum bias events were embedded into, for each particle species in turn. This meant that there were approximately the same number of particles reconstructed in both the raw data and the embedding runs.

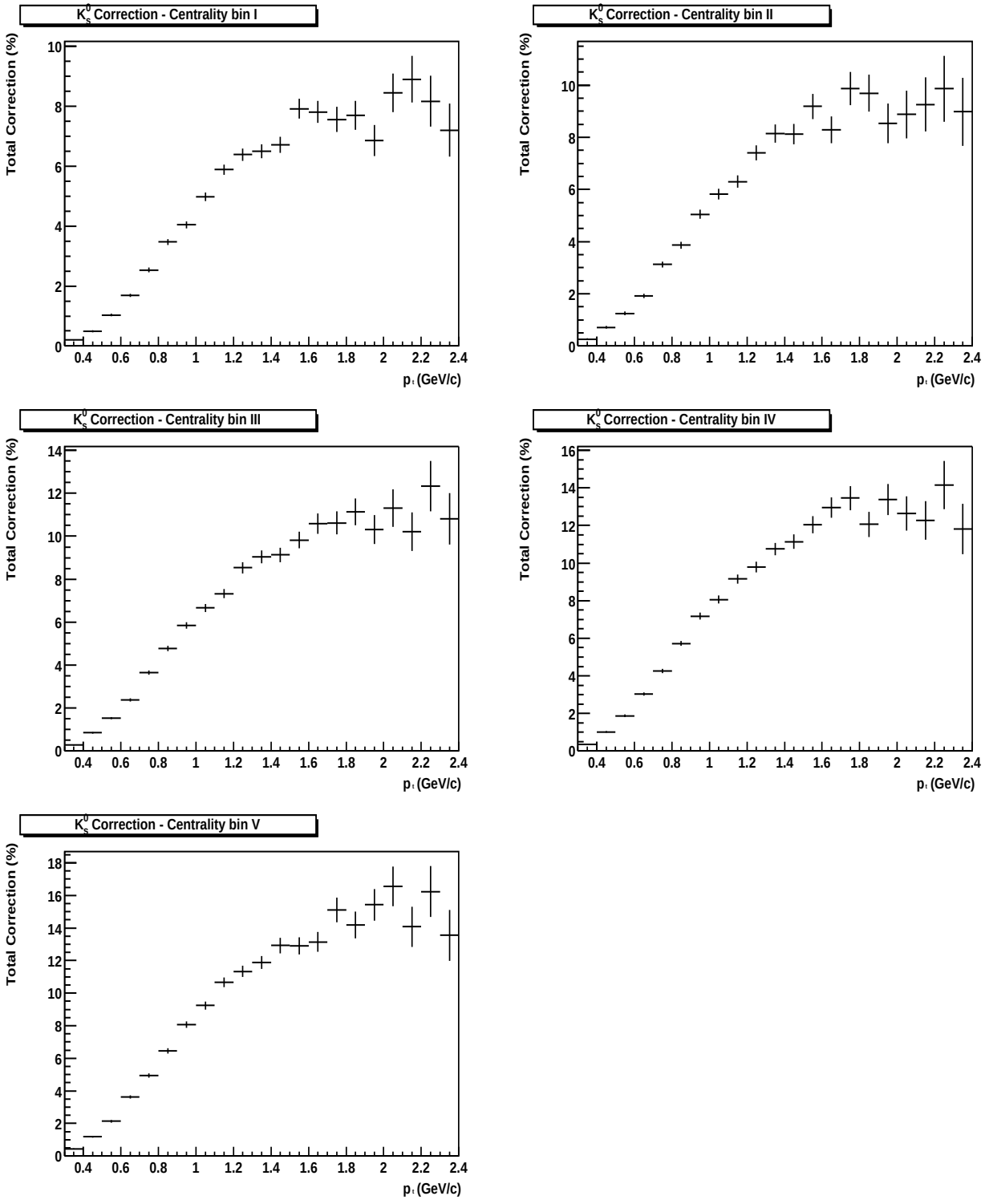

Figure 7.17: The total correction factors for the K^0_s, plotted as a function of collision centrality and p_t. Bin I represents the most central collisions, Bin V represents the least central collisions.

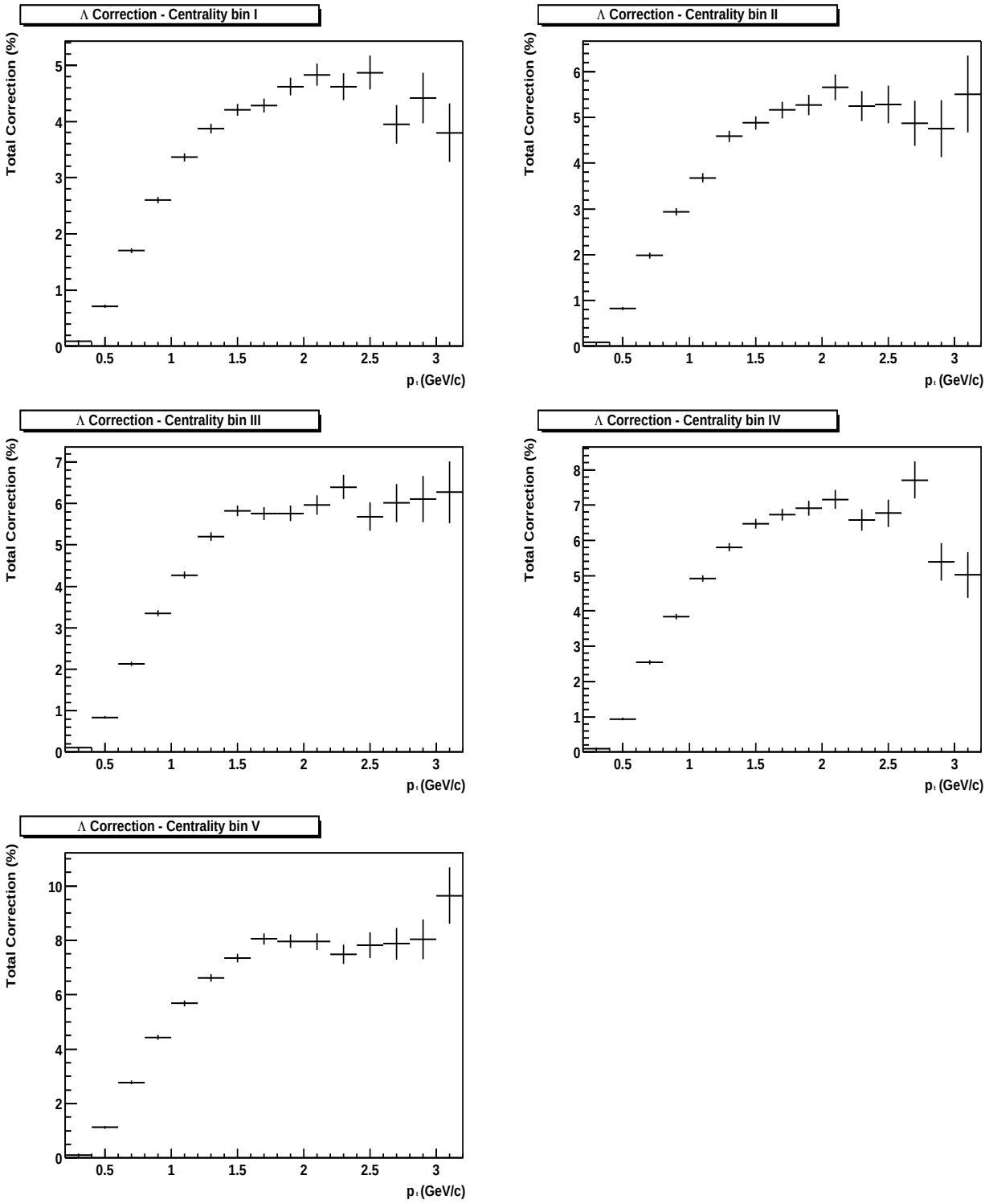

Figure 7.18: The total correction factors for the Λ, plotted as a function of collision centrality and p_t. Bin I represents the most central collisions, Bin V represents the least central collisions.

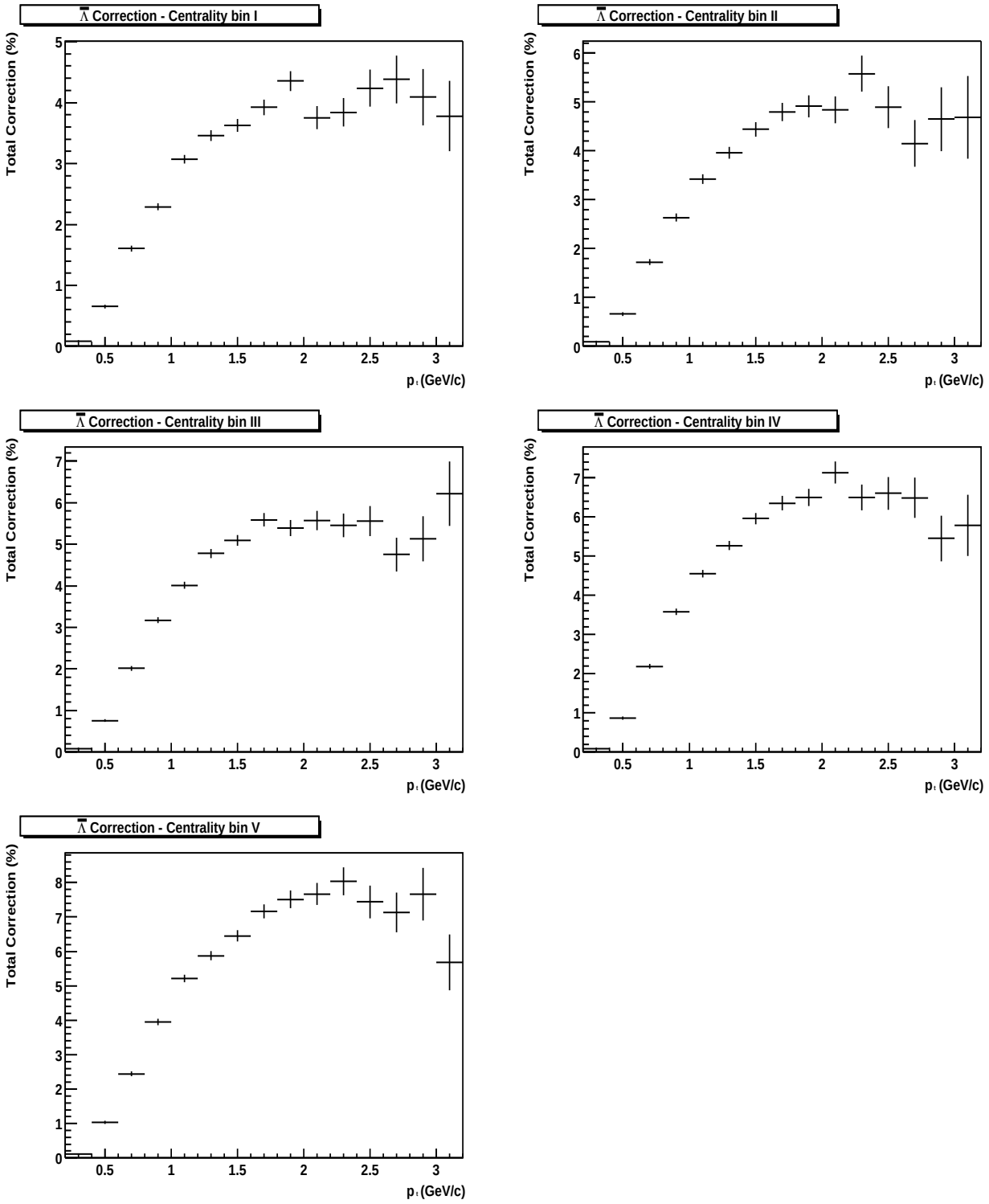

Figure 7.19: The total correction factors for the $\overline{\Lambda}$, plotted as a function of collision centrality and p_t. Bin I represents the most central collisions, Bin V represents the least central collisions.

Chapter 8

Results

The results presented in this chapter were obtained by analysing data taken with both the central and the minimum bias triggers. This means that the $\overline{\Lambda}/\Lambda$ ratio as well as the particle spectra can be investigated as a function of the centrality of the collision. The motivation for performing an analysis as a function of collision centrality is that very peripheral A+A hadronic interactions should be similar to p+p collisions (small volume, few re-interactions) where deconfinement cannot occur, as opposed to central collisions where there are hundreds of participating nucleons and deconfinement may occur. In order to perform such an analysis, a measure of the centrality of each event must be made. This has been accomplished via a conversion of the raw, measured, TPC track multiplicity, into the fraction of total hadronic cross-section, σ_h.

The track multiplicity distribution is shown in Figure 8.1, and is labelled as arbitrary as it does not represent the total number of measured tracks in the event, but rather the number of tracks in the TPC in the range $|\eta| \leq 0.75$. This raw multiplicity is converted into the corrected h^- multiplicity, where h^- refers to all negatively charged tracks, and from this, σ_h can be calculated [101]. The h^- distribution, is used as a reference as all negative particles must be produced in the collision. Table 8.1 shows how the different bins indicated in Figure 8.1 are related to σ_h, (where bin I represents the most central 5% of σ_h), the mean value of the h^- multiplicity in each centrality bin, and the raw K^0_S, Λ and $\overline{\Lambda}$ yields in each centrality bin. The centrality bins were chosen as they were so that there were sufficient statistics in each bin. Note that the central trigger overlaps with the first two centrality bins, and as it

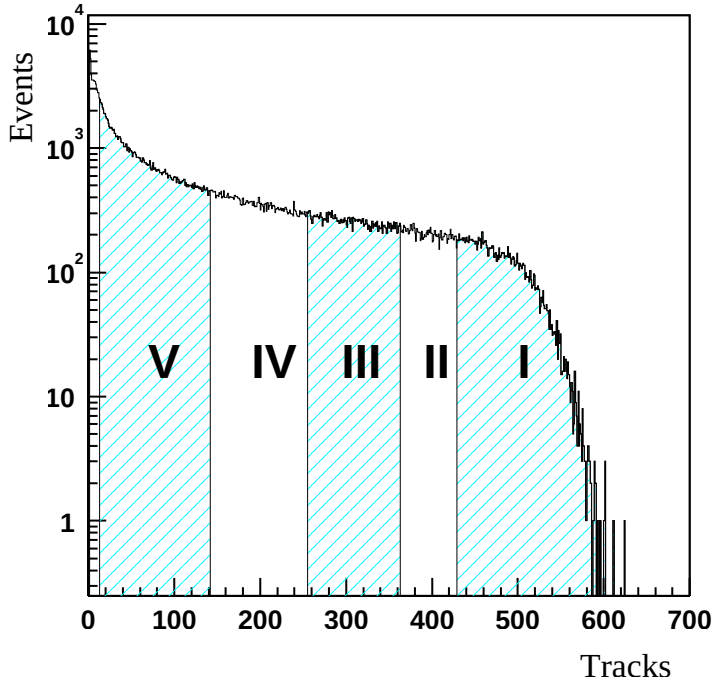

Figure 8.1: Centrality Definition

yields an order of magnitude greater raw statistics than the minimum bias dataset, the central dataset was used to calculate the particle spectra for the two most central bins (I and II).

Centrality Bin	σ_h	$<N_{h^-}>$	K^0_S yield	Λ yield	$\overline{\Lambda}$ yield
I	$0\% \rightarrow 5\%$	33.3	9392	5688	4041
II	$5\% \rightarrow 10\%$	109.6	8518	4547	3357
III	$10\% \rightarrow 20\%$	186.7	14398	7488	5412
IV	$20\% \rightarrow 35\%$	243.4	15053	7502	5488
V	$35\% \rightarrow 75\%$	296.6	12723	5717	4453

Table 8.1: The centrality bins used in this analysis, their definition in terms of σ_h and the raw yields of the K^0_S, Λ and $\overline{\Lambda}$.

The total coverage in collision centrality for the five bins is the top 75% of σ_h, which represents greater than 14 measured tracks in the TPC, indicated on Figure 8.1. Below this value, the fact that there are only a few tracks in the detector makes the exact determination of the position of the primary vertex difficult.

8.1 $\overline{\Lambda}/\Lambda$ Ratio

By investigating the anti-baryon to baryon ratio, much can be learned about the initial conditions of the collision. If the amount of baryon stopping is large, then there is an abundance of quarks in the fireball from the participating nucleons. It is then easier to produce a Λ (uds) with a K^+ ($u\overline{s}$) through the reaction N+N->N+Λ +K^+ (known as associated production), than a Λ and an $\overline{\Lambda}$ ($\overline{u}\overline{d}\overline{s}$) through the reaction N+N->N+N+Λ +$\overline{\Lambda}$ (known as pair production). The $\overline{\Lambda}/\Lambda$ ratio is governed by the relative rates of associated production and pair production, as given in equation 8.1, where Y_Λ represents the Λ yield, $Y_{\overline{\Lambda}}$ the $\overline{\Lambda}$ yield, and Y_{pp} and Y_{ap} the yields from pair production and associated production respectively.

$$\frac{Y_{\overline{\Lambda}}}{Y_\Lambda} = \frac{Y_{pp}}{Y_{pp} + Y_{ap}} \tag{8.1}$$

In a baryon-rich scenario, the baryo-chemical potential (μ_B) is large, and the production of anti-baryons is suppressed, therefore associated production dominates the Λ yield. As μ_B reduces, the relative importance of associated production to pair production decreases and the $\overline{\Lambda}/\Lambda$ ratio tends to 1. Therefore, a measure of the $\overline{\Lambda}/\Lambda$ ratio is sensitive to the net baryon density at mid-rapidity in the collision. Also, due to the predicted strangeness enhancement in a QGP, the values of the strange $\overline{\text{B}}$/B ratios may increase, for a constant temperature and a constant μ_B [102].

When measuring $\overline{\Lambda}$ and Λ particles in the detector, the values reported also include the yield of Σ^0 (uds) and $\overline{\Sigma^0}$ ($\overline{u}\overline{d}\overline{s}$) respectively. These decay electromagnetically through the channels $\Sigma^0 \rightarrow \Lambda\ \gamma$ and $\overline{\Sigma^0} \rightarrow \overline{\Lambda}\ \gamma$, with a mean lifetime ($c\tau$) of 2.22 x 10^{-11}m and a branching fraction of 100%, which means that they cannot be distinguished experimentally from primary Λ and $\overline{\Lambda}$ hyperons. However, this is the case for all experiments, so comparisons of yields and $\overline{\Lambda}/\Lambda$ ratios with other experimental values are valid, but care has to be taken when comparing to theoretical models and predictions, where Σ^0 and Λ may be treated separately.

As the acceptance of the TPC is symmetric with respect to both charge signs, the efficiency of finding an $\overline{\Lambda}$ is approximately the same as that for a Λ. Therefore, raw Λ and $\overline{\Lambda}$ yields can be used to determine the $\overline{\Lambda}/\Lambda$ ratio without applying any of the corrections discussed in the previous chapter. The only difference is the absorption of both Λ and $\overline{\Lambda}$ hyperons which occurs with the material in the detector. This effect

has been studied using the Monte-Carlo (MC) generated Λ and $\overline{\Lambda}$ particles used in embedding. The absorption effect is greatest for the $\overline{\Lambda}$, as expected, and is approximately constant as a function of transverse momentum and rapidity in the measured range. The average value of the correction to the ratio itself is 0.990 ± 0.008 and has been applied to all results quoted in this chapter.

8.1.1 Integrated $\overline{\Lambda}/\Lambda$ Ratio

Figure 8.2 shows a plot of the $\overline{\Lambda}$ mass (red) superimposed onto the Λ mass (black), and it represents the full statistics available in the rapidity range $|y| < 0.5$, integrated over all transverse momenta. From this, the value of the $\overline{\Lambda}/\Lambda$ ratio after the absorption correction was applied, was determined to be : 0.736 ± 0.008 (statistical). This suggests, utilising equation (8.1), that at mid-rapidity, approximately 74% of Λ come from pair production, and approximately 26% come from associated production.

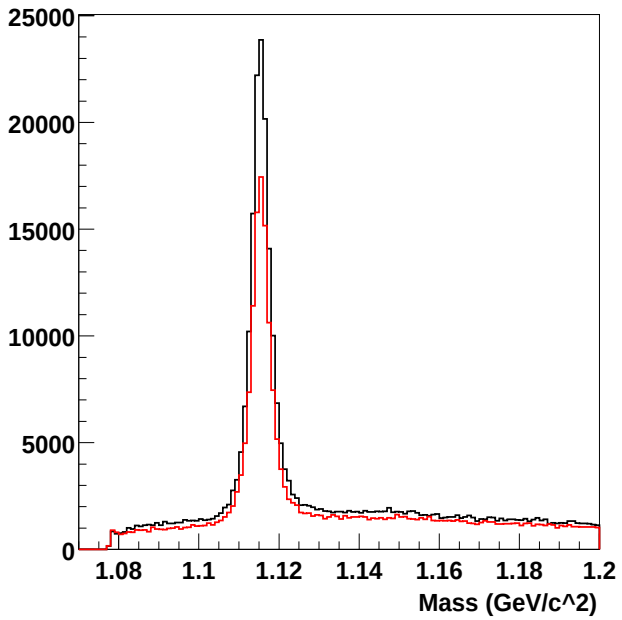

Figure 8.2: Λ (black) and $\overline{\Lambda}$ (red) mass distributions, using all available data in the rapidity range $|y| < 0.5$.

The $\overline{\Lambda}/\Lambda$ ratio behaviour was also investigated as a function of different physical variables. In order to accomplish this, the data were divided into different bins of

the relevant quantity, whilst summing over the other variables. Table 8.2 shows the binning used for each variable under consideration.

Variable	Bin Low	Bin high	No. Bins	Bin width
Rapidity	-1.0	1.0	10	0.2
p_t (GeV/c)	0.4	3.6	16	0.2
Centrality (σ_h)	75%	0%	5	Variable

Table 8.2: The binning and ranges used in the rapidity, p_t and centrality dependent analyses.

8.1.2 Rapidity Dependence of $\overline{\Lambda}/\Lambda$

The $\overline{\Lambda}/\Lambda$ ratio as a function of rapidity is shown in Figure 8.3. It has an interesting feature in that it is flat about mid-rapidity and then it decreases at larger rapidities, which suggests that the distributions in rapidity of the Λ and $\overline{\Lambda}$ are different. As discussed above, the $\overline{\Lambda}/\Lambda$ ratio is dependent on the amount of nuclear stopping in the collision.

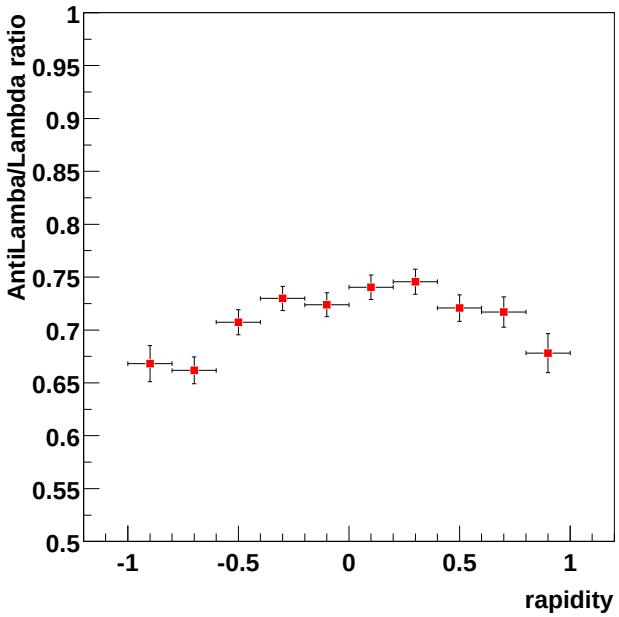

Figure 8.3: $\overline{\Lambda}/\Lambda$ ratio as a function of rapidity.

At mid-rapidity, it is seen that the stopping is low, however, at rapidities away from zero, this may not necessarily be the case. At y = 3, for example, the baryons only have to lose $\sim$ 2 units of rapidity compared to $\sim$ 5 units in order to be transported to mid-rapidity. As a consequence, it is expected that the net-baryon density is larger at higher rapidities, a fact borne out by a measurement of the $\overline{p}/p$ ratio by the BRAHMS experiment at different rapidities. They find that the ratio drops from $\sim$ 0.66 at y = 0 to $\sim$ 0.41 at y = 2, for the 40% most central collisions [103].

The rapidity dependence of the $\overline{\Lambda}/\Lambda$ ratio, shown in Figure 8.3 can then be explained in terms of this dependence on rapidity of μ_B. At higher rapidities, the fraction of Λ coming from associated production is larger than those coming from pair production, as the production of anti-baryons becomes suppressed. As a result, the $\overline{\Lambda}/\Lambda$ ratio decreases.

8.1.3 Transverse Momentum Dependence of $\overline{\Lambda}/\Lambda$

The $\overline{\Lambda}/\Lambda$ ratio as a function of p_t is presented in Figure 8.4. The spectrum is consistent with being flat over the measured range of p_t, within the stated statistical error bars. The small increase in the ratio between p_t = 1.0 GeV/c and 1.5 GeV/c is enhanced in the plot, due to the suppressed 0 in the ordinate.

At the low transverse momenta in Figure 8.4, it is not surprising that the $\overline{\Lambda}/\Lambda$ ratio is flat, as coupled with the fact that most of the $\overline{\Lambda}$ and Λ are produced in the same reaction, there will be plenty of re-scattering. At higher p_t, the $\overline{\Lambda}/\Lambda$ ratio should tend to 0 as the higher p_t particles are produced from fragmenting jets. It has been predicted that this fall off with p_t should be approximately 10% by $p_t \sim$ 3.5 GeV/c [85], and due to the large statistical errors, this can not be ruled out by the data.

8.1.4 Centrality Dependence of $\overline{\Lambda}/\Lambda$

The $\overline{\Lambda}/\Lambda$ ratio has also been investigated as a function of the centrality of the collision. As the most peripheral collisions tend towards simple nucleon-nucleon collisions, then there could be a difference in the amount of baryon stopping between these peripheral collisions and central nucleus-nucleus collisions, and hence a difference in the $\overline{\Lambda}/\Lambda$ ratio. Figure 8.5 shows this ratio for the five centrality bins outlined in section 8

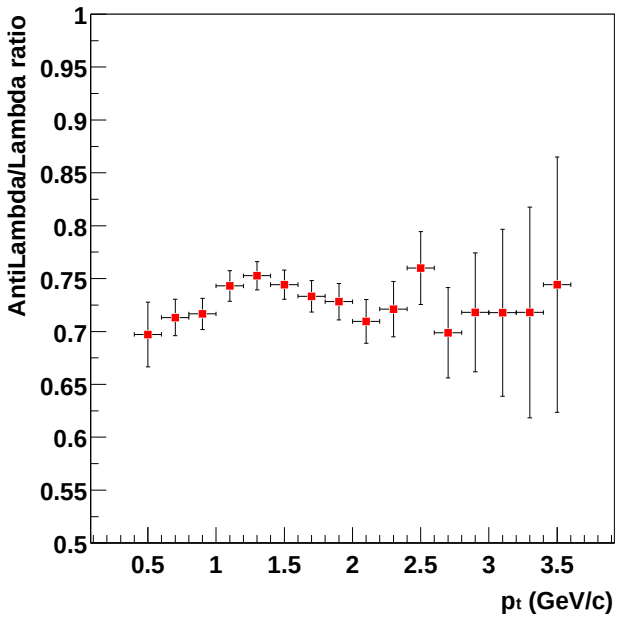

Figure 8.4: $\overline{\Lambda}/\Lambda$ ratio as a function of transverse momentum.

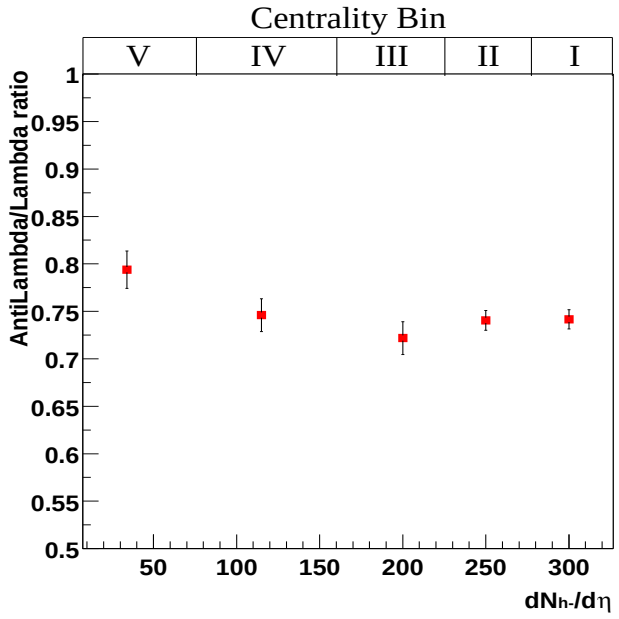

Figure 8.5: $\overline{\Lambda}/\Lambda$ ratio as a function of collision centrality.

There is a slight rise in the ratio in the most peripheral bin, which indicates an effect of the order of $\sim 10\%$. However, a larger dataset enabling finer binning and greater

coverage at lower centralities would be required to investigate this centrality dependence further.

The $\overline{\Lambda}/\Lambda$ ratio was also reported to be flat as a function of centrality in Pb+Pb collisions at $\sqrt{s_{NN}} \simeq 17$ GeV at the SPS by WA97, whose four centrality bins covered the most central 40% of the cross-section [104]. However, an increase in the ratio of a factor of 3 was observed by WA97 when comparing p+Be collisions to Pb+Pb.

8.1.5 Systematic Error Determination

In order to estimate the systematic error on the ratio, the process of systematically changing the value of the geometrical cuts and re-calculating the ratio was used. This process showed that the value of the ratio was extremely stable to different cuts, and a systematic error of 0.005 (or 0.6%) was obtained.

The value of the $\overline{\Lambda}/\Lambda$ ratio in different physical regions within the TPC was investigated as another possible source of systematic errors. The ratio was calculated as a function of the azimuthal angle, ϕ, and the z position (drift axis) of the primary vertex. The $\overline{\Lambda}/\Lambda$ distribution was flat as a function of ϕ, but discrepancies were seen in the z distribution, which is shown in Figure 8.6. Here, the $\overline{\Lambda}/\Lambda$ ratio is plotted as a function of the position along the z axis of the primary vertex, while no restriction was placed upon the co-ordinates of the decay vertices of either the $\overline{\Lambda}$ or the Λ. As charge drifts to either end of the TPC, this effect illustrates that the two halves are effectively independent detectors with different responses. The systematic error was determined by calculating the mean value of the $\overline{\Lambda}/\Lambda$ ratio in each half of the TPC. The assumption was then made that the difference between these values and the value calculated over all z was the major source of the systematic error. Using this method, the systematic error of 0.022 ($\sim 3\%$) was calculated.

By summing in quadrature the systematic errors obtained from the variation of the geometrical cuts, as well as the vertex distribution in z, the final systematic error for the $\overline{\Lambda}/\Lambda$ ratio was determined to be 0.023 ($\sim 3\%$), and is constant as a function of centrality, transverse momentum and rapidity. Therefore, the final integrated ratio was determined to be : $\overline{\Lambda}/\Lambda = 0.736 \pm 0.008 \pm 0.023$.

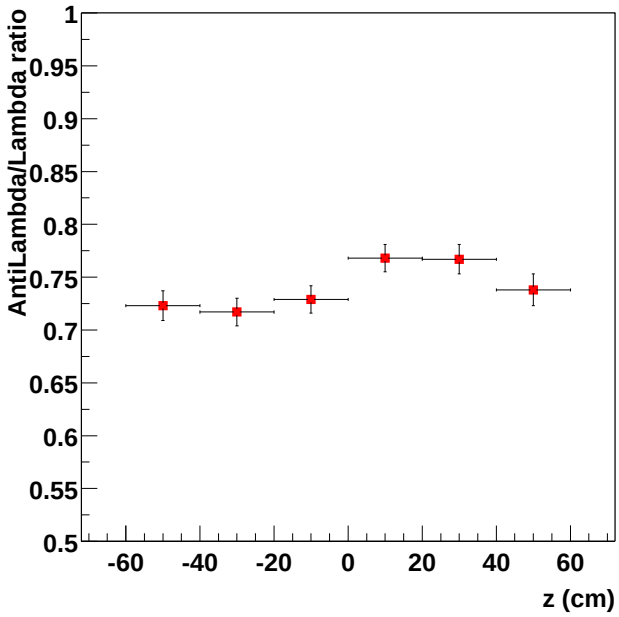

Figure 8.6: $\overline{\Lambda}/\Lambda$ ratio as a function of the z co-ordinate of the reconstructed primary vertex.

8.2 Corrected Yields

This next section outlines how the yields of K^0_S, Λ and $\overline{\Lambda}$ were obtained by applying the corrections obtained in section 7.4 to the raw data distributions. The yields of the K^0_S, Λ and $\overline{\Lambda}$ enable a measurement of the amount of strangeness produced in the collision, as (along with the charged kaons) they carry the majority of the produced strangeness. In conjunction with data from other collision systems (e.g. p+p, p+A), the yields can give quantitative information on any form of strangeness enhancement.

The finite acceptance of the detector means that even after applying all of the corrections, it is still not possible to measure the average yield per event of a given particle species over full phase space. In order to make comparisons between experiments feasible, the yields are reported over all p_t and per unit rapidity, denoted by $dN/d\mathrm{y}$.

Starting from the total invariant cross-section, using generally accepted nomenclature it can be shown that [31],

$$E\frac{d^3\sigma}{dp^3} = E\frac{d^2\sigma}{2\pi p_t dp_t dp_{||}} \tag{8.2}$$

and by making the substitution $dp_{||} = Ed\mathbf{y}$ using the relations in equations (A.2) and (A.3), equation (8.2) becomes

$$E\frac{d^3\sigma}{dp^3} = const.\frac{1}{2\pi p_t}\frac{d^2N}{d\mathbf{y}dp_t} \tag{8.3}$$

Under the assumption that the p_t distribution is thermal, it has been shown that equation (8.4) is valid,

$$E\frac{d^3\sigma}{dp^3} = const.\frac{1}{2\pi p_t}\frac{d^2N}{d\mathbf{y}dp_t} = const.m_t\sum_{n=1}^{\infty}(\mp)^{n+1}K_1(n\frac{m_t}{\mathrm{T}}) \tag{8.4}$$

where K_1 is a modified Bessel function and T is the temperature of the particular particle species under consideration [31]. An approximation is usually made to equation (8.4) which is of the form given in equation (8.5), where A is a multiplicative constant. From equation (8.5), the temperature parameter, T, is more commonly referred to as the inverse slope parameter.

$$\frac{1}{2\pi p_t}\frac{d^2N}{d\mathbf{y}dp_t} = A\sqrt{m_t}.e^{\frac{-m_t}{T}} \tag{8.5}$$

In order to make comparisons with data from other experiments, the $\sqrt{m_t}$ is usually dropped, and using the relationship between p_t and m_t (equation (A.4)), it can also be shown that,

$$\frac{1}{2\pi p_t}\frac{d^2N}{d\mathbf{y}dm_t} = \frac{1}{2\pi m_t}\frac{d^2N}{d\mathbf{y}dm_t} = Ae^{\frac{-m_t}{T}} \tag{8.6}$$

which is used more often in the literature.

By integrating equation (8.6) over m_t, the constant factor on the right hand side can be evaluated exactly in terms of the $dN/d\mathbf{y}$ (extrapolated to m_t = m_0, and m_t = ∞), as given in equation (8.7).

$$\frac{1}{2\pi m_t}\frac{d^2N}{d\mathbf{y}dm_t} = \frac{dN/d\mathbf{y}}{2\pi T(m_0+T)}e^{-(m_t-m_0)/T} \tag{8.7}$$

The advantage of this method is that by fitting one function to the measured data, both the yield and the inverse slope parameter can be extracted. The data is also now plotted versus (m_t-m_0) on the horizontal axis, where m_0 is the rest mass of the particle. This involves a simple translation along the axis and does not affect the shape of the spectra. This has the advantage that, if desired, the spectra of particles of different masses can be plotted on the same histogram, with the same scale on the horizontal axis. This provides a visual aid for determining differences in slopes of the different particles.

8.2.1 K^0_S Yields and Inverse Slopes

The K^0_S data were split into 21 different p_t bins of equal width in the range 0.3 $< p_t <$ 2.4 GeV/c. The fitted raw mass distributions for every third p_t bin are shown in Figures 8.8 and 8.9. Due to a lack of statistics in the minimum bias dataset, not all of these p_t bins could be utilised in all of the centrality bins. For the two most central bins, the statistics were increased by adding the central data to the minimum bias data.

The corrected K^0_S distributions for all centrality bins in the rapidity range $<$ |y | <0.5 are shown in Figure 8.7, where the data are normalised by the number of events used in the analysis (Nev). The fits to the data using equation (8.7) show that the parameterisation describes the data well, for all five of the centrality bins. The yields and inverse slopes obtained in the fit are presented in Table 8.3. The yields reported in Table 8.3 have been extrapolated to m_t = m_0, and m_t = ∞. The extrapolation outside the measured p_t range contributes about 20% of the total yield.

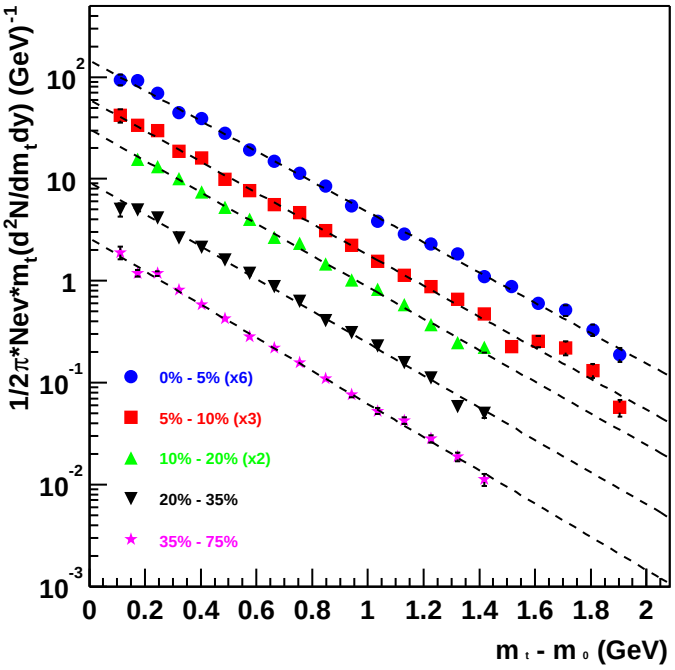

Figure 8.7: Transverse mass distributions of the K^0_S, plotted for various centralities. The three most central bins (I, II and III) have been scaled for clear viewing.

Centrality Bin	dN/dy	T (MeV)	χ^2/dof
I	35.22±0.73	292±3	1.39
II	28.02±0.80	285±3	1.56
III	21.20±0.47	280±5	1.18
IV	12.41±0.30	274±4	1.37
V	3.36±0.07	267±4	1.06

Table 8.3: The extracted yields, inverse slopes and χ^2/dof of the fit, for the K^0_S.

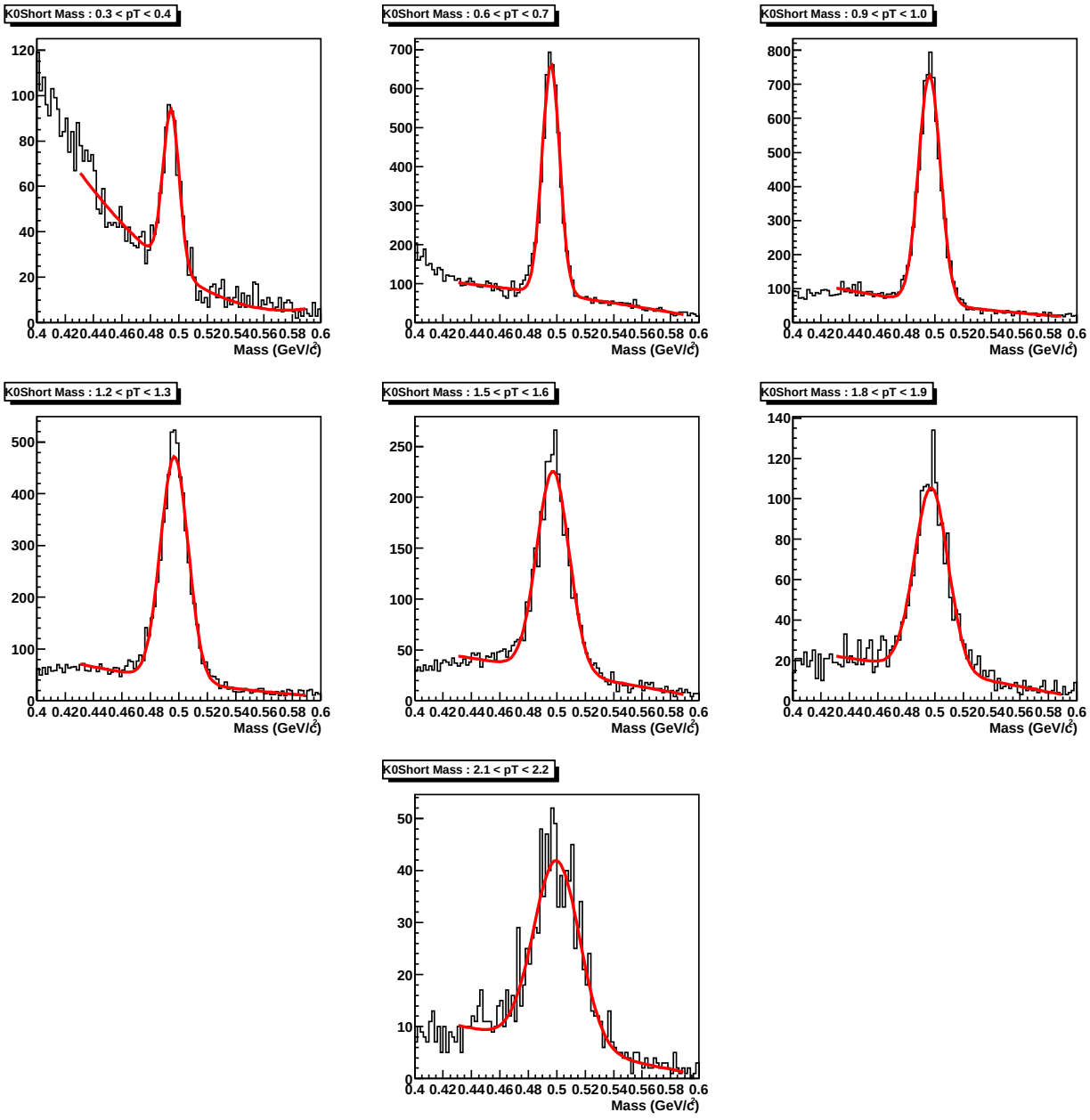

Figure 8.8: Mass distributions and Gaussian fit for the K^0_S, plotted for every third p_t bin for the most central bin (I), using the data from the central dataset.

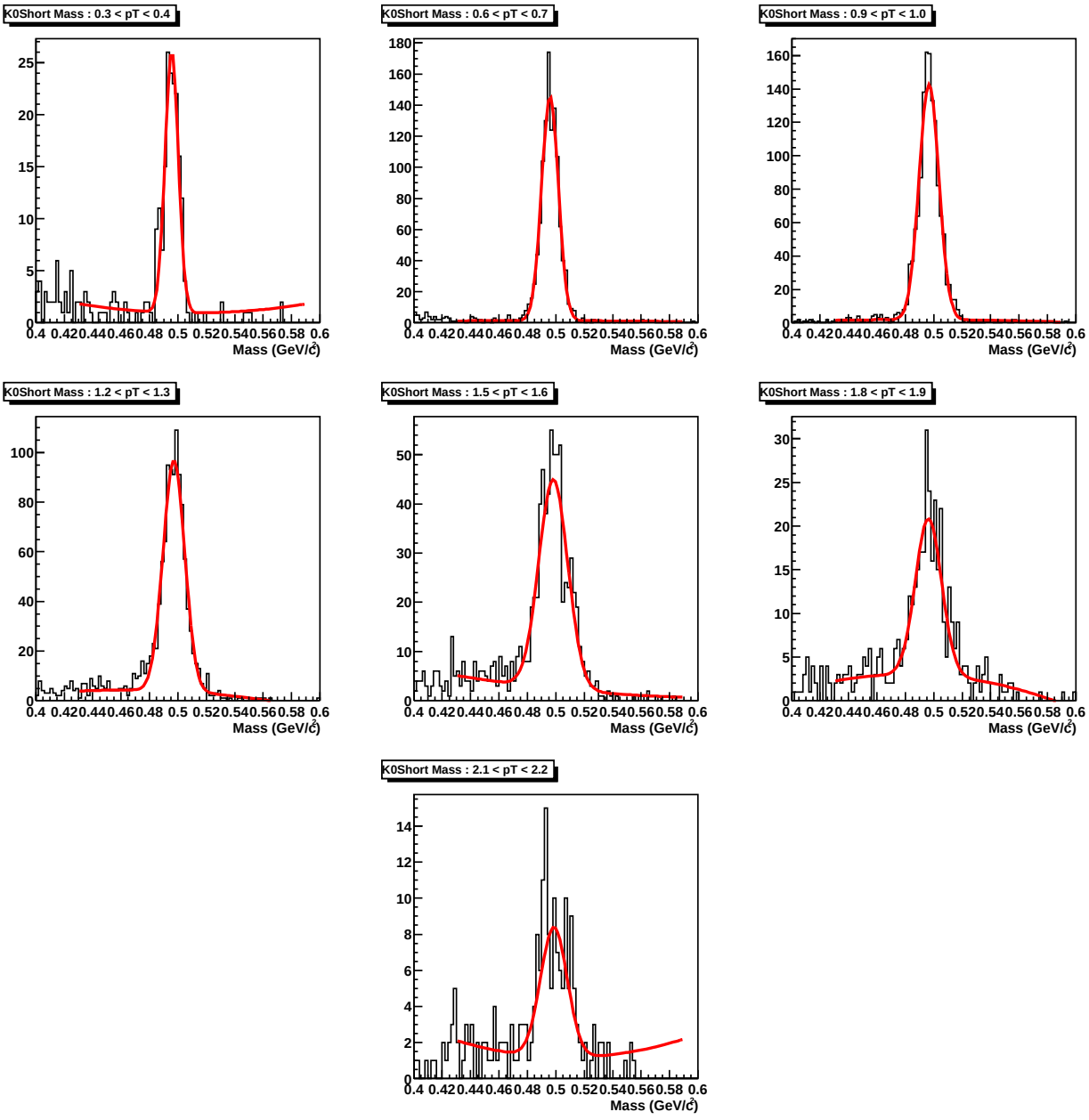

Figure 8.9: Mass distributions and Gaussian fit for the K^0_S, plotted for every third p_t bin for the most peripheral bin (V), using data from the minimum bias dataset.

8.2.2 Λ and $\overline{\Lambda}$ Yields and Inverse Slopes

The same correction process was applied individually to the Λ and the $\overline{\Lambda}$ hyperons, although this time, the p_t ranges were necessarily different to that of the K^0_S. In both cases, the central dataset allowed 14 p_t bins of width 200 MeV/c in the range $0.4 < p_t < 3.2$ GeV/c, whilst the minimum bias dataset allowed 10 p_t bins, again of width 200 MeV/c, in the range $0.4 < p_t < 2.4$ GeV/c.

Both the Λ and $\overline{\Lambda}$ m_t distributions were fit with the expression in equation (8.7). While the fits were quite good (determined from the χ^2 of the fit), the data was seen to deviate from a straight line, and it was found that on average, a better χ^2 was obtained when fitting a Boltzmann expression, which is of the form given in equation (8.8).

$$\frac{1}{2\pi m_t}\frac{d^2N}{d\mathbf{y}dm_t} = Am_t e^{\frac{-m_t}{T}} \tag{8.8}$$

As with equation (8.6), by integrating the expression over m_t, it is possible to calculate the multiplicative constant A in equation (8.8) in terms of the $dN/d\mathbf{y}$, so that again T and $dN/d\mathbf{y}$ are the free parameters in the fit. This takes the form of equation (8.9).

$$\frac{1}{2\pi m_t}\frac{d^2N}{d\mathbf{y}dm_t} = \frac{m_t dN/d\mathbf{y}}{2\pi T(m_0^2 + 2m_0T + 2T^2)} e^{\frac{-(m_t - m_0)}{T}} \tag{8.9}$$

Figures 8.10 and 8.11 show the m_t distributions for the Λ and $\overline{\Lambda}$ respectively. In both plots, the fits with a straight line exponential (equation (8.7)) and the Boltzmann distribution (equation (8.9)), and again the three most central bins have been scaled to allow for easier viewing.

The yields and inverse slopes have been extracted from both fits and are tabulated in Table 8.4 and Table 8.5 for the Λ and $\overline{\Lambda}$ respectively, along with the χ^2 per degree of freedom for each fit. In both cases, the Λ and the $\overline{\Lambda}$ yields from the two fitting functions agree with each other very well. There is a difference in the slope parameter, however, which is to be expected as the fitting functions are different. The differences in inverse slope between the two values are approximately constant ($\sim$ 50MeV) as a function of centrality, for both the Λ and the $\overline{\Lambda}$.

Note that the largest differences in the χ^2 between the fits is in the most central bins. The reason for this is that the p_t coverage extends out to higher p_t due to the greater statistics from the central dataset, and it is these high p_t data-points which deviate most from the straight line exponential.

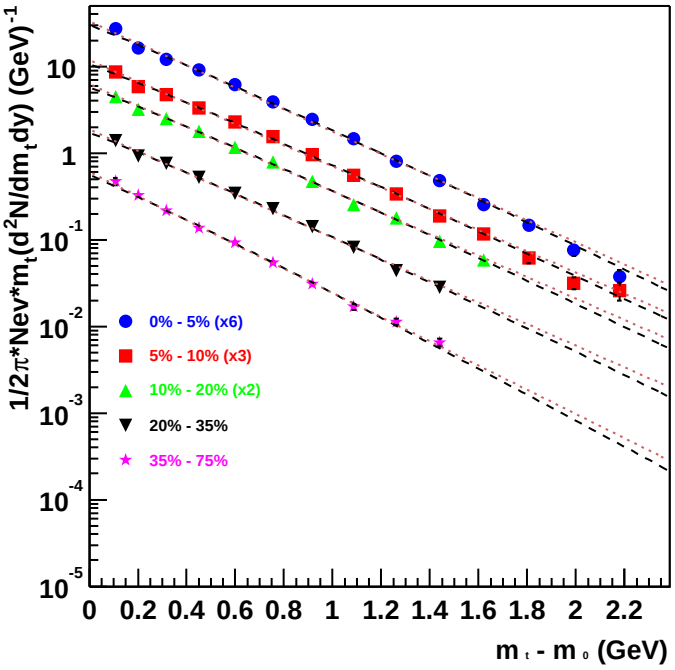

Figure 8.10: Transverse mass distributions of the Λ, plotted for various centralities. Centrality bins I, II and III have been scaled for clear viewing. Both a straight line exponential (brown) and a Boltzmann function (black) have been fit to the data points.

Centrality Bin	$dN/dy_{(SLE)}$	$T_{(SLE)}$ (MeV)	χ^2/dof	$dN/dy_{(Boltz.)}$	$T_{(Boltz.)}$ (MeV)	χ^2/dof
I	17.26±0.49	340±6	2.03	16.85±0.35	290±4	1.49
II	12.84±0.31	355±6	1.49	12.56±0.21	300±3	1.03
III	10.11±0.22	351±6	1.11	9.90±0.17	295±4	0.89
IV	5.98±0.15	348±7	1.30	5.86±0.11	292±4	1.02
V	1.69±0.03	311±5	0.86	1.66±0.04	264±4	1.06

Table 8.4: The extracted yields, inverse slopes and χ^2/dof for the two different fits to the Λ spectra, in the different centrality bins.

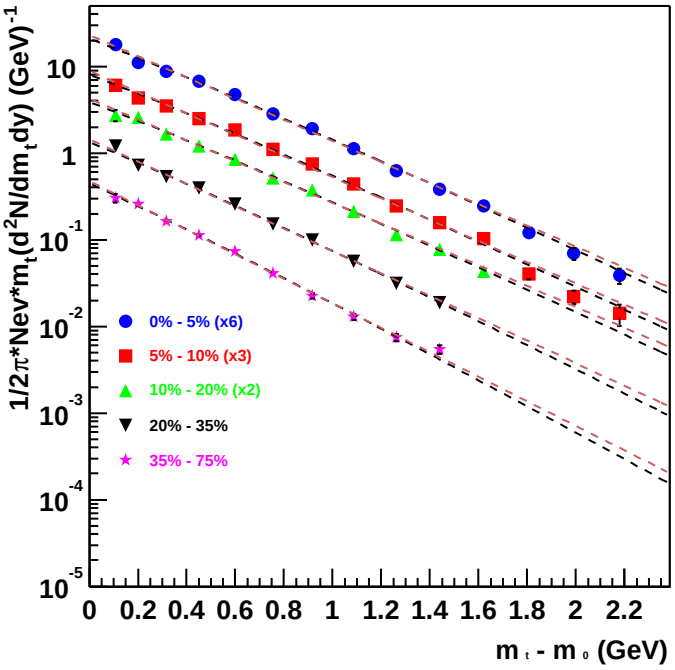

Figure 8.11: Transverse mass distributions of the $\overline{\Lambda}$, plotted for various centralities. Centrality bins I, II and III have been scaled for clear viewing. Both a straight line exponential (brown) and a Boltzmann function (black) have been fit to the data points.

Centrality Bin	$dN/dy_{(SLE)}$	$T_{(SLE)}$ (MeV)	χ^2/dof	$dN/dy_{(Boltz.)}$	$T_{(Boltz.)}$ (MeV)	χ^2/dof
I	12.58±0.35	356±7	1.79	12.29±0.26	301±4	1.34
II	9.67±0.32	354±8	1.85	9.46±0.23	300±5	1.39
III	7.11±0.18	359±8	1.08	6.95±0.16	302±5	0.99
IV	4.43±0.11	336±7	1.06	4.34±0.09	283±4	0.92
V	1.31±0.03	307±6	1.08	1.29±0.03	262±5	1.10

Table 8.5: The extracted yields, inverse slopes and χ^2/dof for the two different fits to the $\overline{\Lambda}$ spectra, in the different centrality bins.

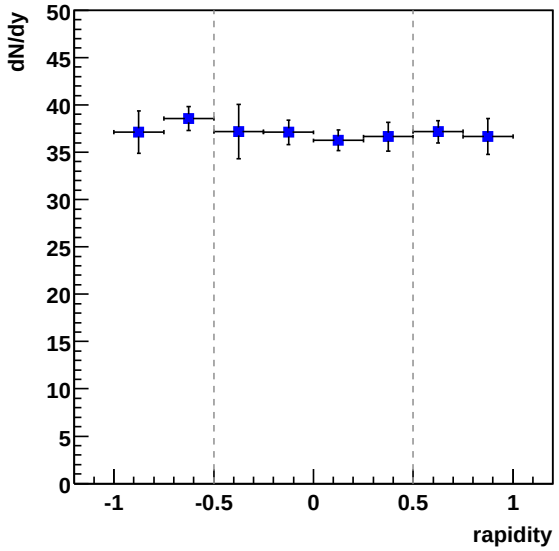

Figure 8.12: The dN/d**y** of the K^0_s as a function of rapidity for the most central bin.

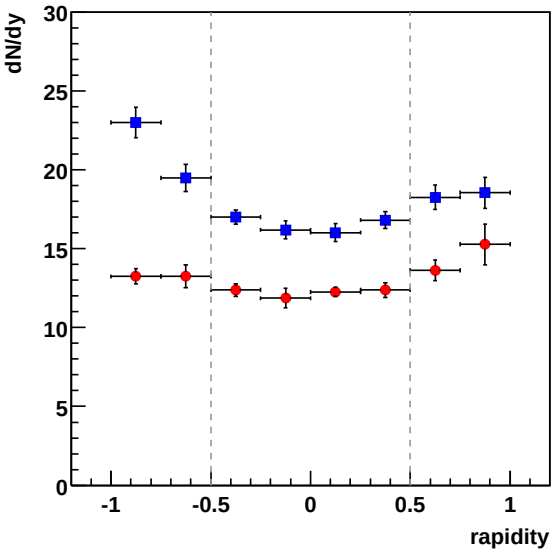

Figure 8.13: The dN/d**y** of the Λ (blue) and $\overline{\Lambda}$ (red) as a function of rapidity for the most central bin. The grey lines represent the range of rapidities used in the analysis.

8.2.3 Rapidity Distributions

The total integrated yields for the K^0_S, Λ and $\overline{\Lambda}$, presented in Tables 8.3 - 8.5 were measured in the rapidity interval -0.5 < y < 0.5. As the acceptance of all three particle species extends to approximately | y |<1.2 (shown in Figure 7.11), the dN/dy was calculated as a function of y in the range | y |<1. These distributions are shown in Figure 8.12 and Figure 8.13.

It is evident from this that there is no significant deviation from a flat distribution for the K^0_S. The errors are necessarily larger than the value given in Table 8.3 as the available statistics per bin were a factor of four smaller than used previously. On the other hand, both the Λ and $\overline{\Lambda}$ distributions show a rise at larger rapidities. It has been seen in previous experiments that as expected, all $\overline{\Lambda}$ hyperons are produced at mid-rapidity [106]. This dip therefore indicates that some unresolved problems could exist in determining the Λ and $\overline{\Lambda}$ spectra.

8.2.4 Reproducibility of the Data by the Simulation

In order to be sure that the correction factors being applied are correct, the simulation must be able to reproduce the data well. In order to assess this, several checks were made. The first method was to compare the distributions of the cut variables in the MC to those in the raw data, the next method compared how well the MC reproduced the data in different physical areas in the detector, and the final method was to perform a lifetime correction on the data, as the result in this case is known.

8.2.4.1 Comparison of Cut Variables

The cut variables should have the same distribution, in both the reconstructed MC data, as well as in the reconstructed raw data, so that when cuts are applied, they have the same effect in the MC as in the data. These cut-variable distributions are shown in Figure 8.14 for the K^0_S, Figure 8.15 for the Λ and Figure 8.16 for the $\overline{\Lambda}$. In all three figures, the blue distributions represent the raw reconstructed data, and the red distributions represent the reconstructed embedded data, and all distributions are normalised to unity.

Of all the cut distributions that were investigated, the only one which showed significant differences were the DCAs of the parent V0 to the primary vertex, though the difference was much greater for the Λ and $\overline{\Lambda}$ compared to the K^0_S. Although the hits distributions are also slightly different, the mean values are only different by 1 hit, with the real data tracks having more hits that the reconstructed embedded tracks. As the cut is placed on the tail of the hit distributions, then the difference that this offset in the distributions makes is small.

Unlike the K^0_S, both the Λ and $\overline{\Lambda}$ particles that are measured are not necessarily primary particles. The Λ may also originate from decays of the Ξ^-, Ξ^0 and Ω^-, whilst the $\overline{\Lambda}$ may come from $\overline{\Xi^+}$, $\overline{\Xi^0}$ and $\overline{\Omega^+}$ decays, and these secondary particles are known as feed-down particles. In the cases of the charged parent particles, the primary particles will bend in the magnetic field and will decay away from the primary vertex with a mean lifetime of 4.91 cm in the cases of the Ξ^- and $\overline{\Xi^+}$, and 2.46 cm for the Ω^- and $\overline{\Omega^+}$. This, combined with a momentum kick in the decay which comes from the mass differences between the parent and daughter particles, means that the secondary Λ and $\overline{\Lambda}$ will have a different DCA distribution at the primary

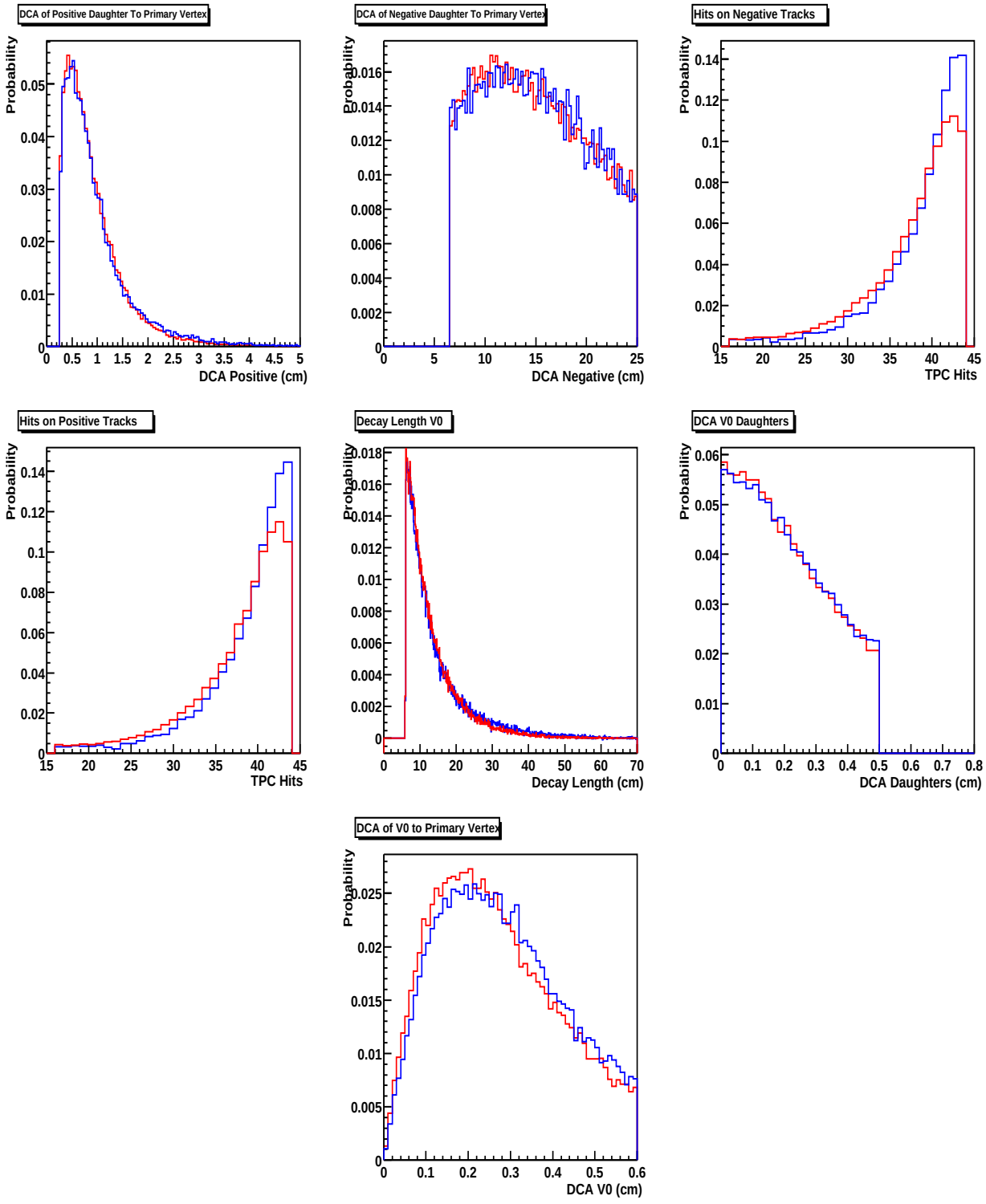

Figure 8.14: Distributions of the various cut variables for the K^0_S. The blue distributions represent the reconstructed raw data, the red distributions are for the reconstructed MC data.

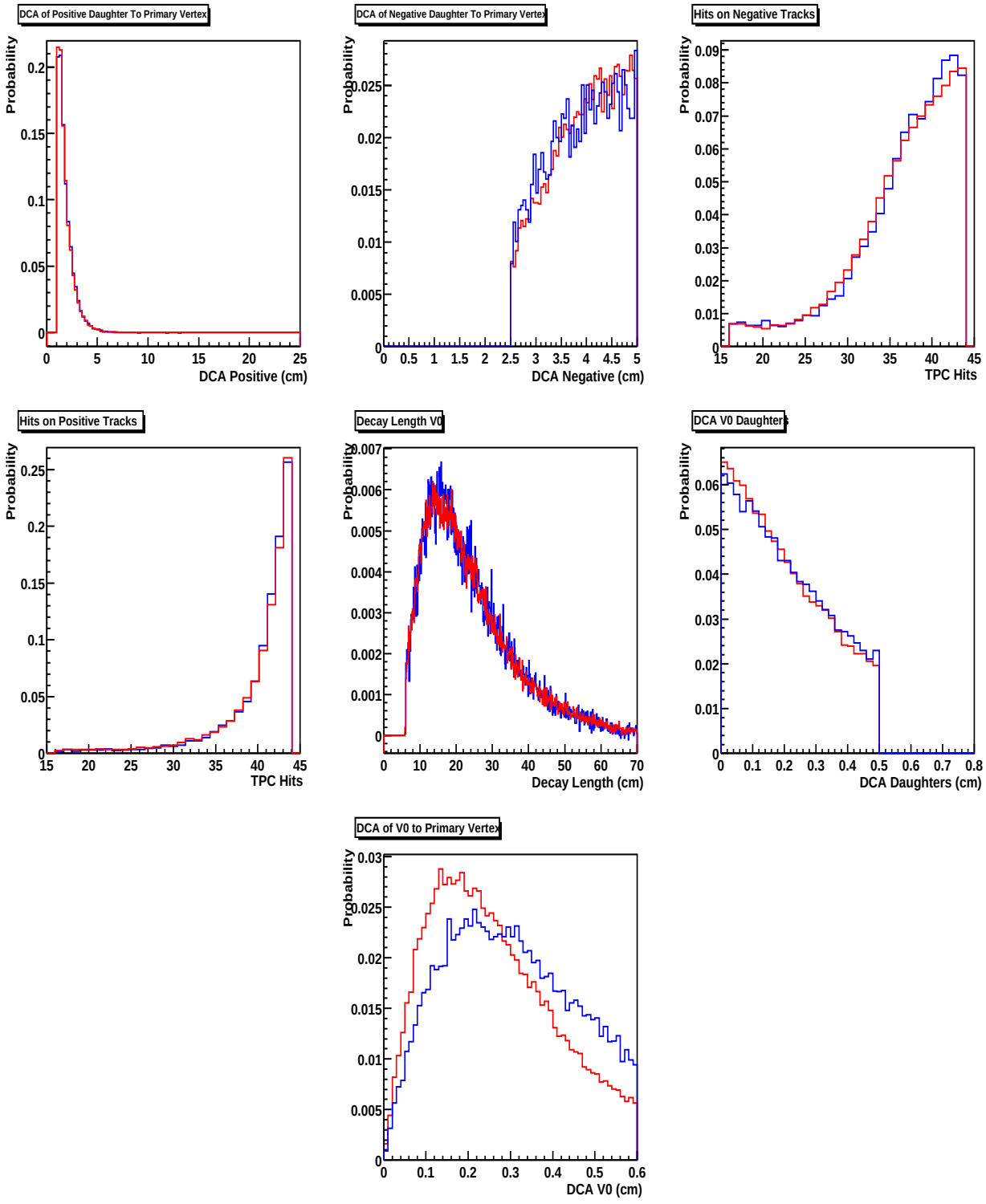

Figure 8.15: Distributions of the various cut variables for the Λ. The blue distributions represent the reconstructed raw data, the red distributions are for the reconstructed MC data.

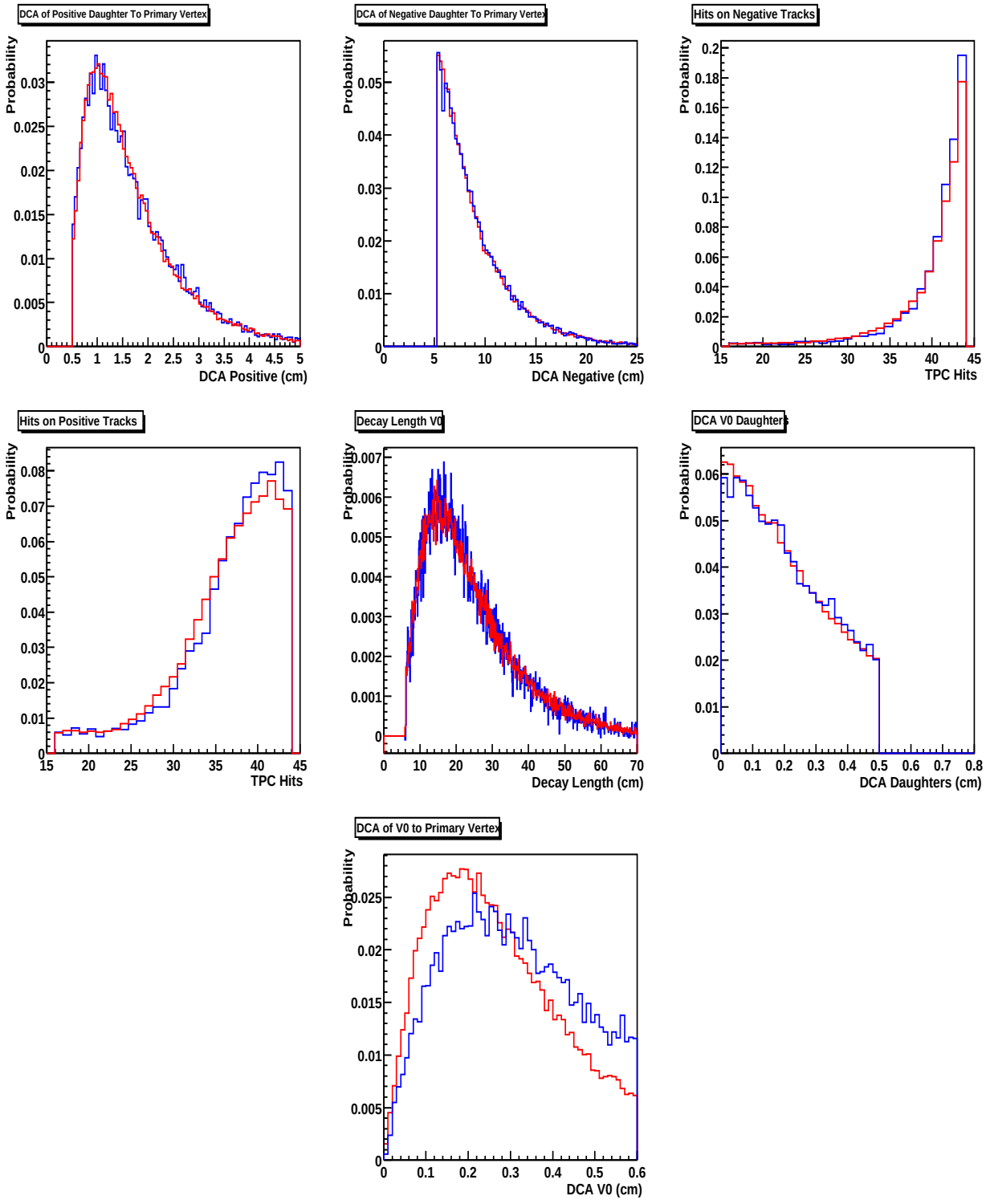

Figure 8.16: Distributions of the various cut variables for the $\overline{\Lambda}$. The blue distributions represent the reconstructed raw data, the red distributions are for the reconstructed MC data.

vertex. The momentum kick in the decay of the neutral Ξ^0 and $\overline{\Xi^0}$, which do not bend in the magnetic field, also means that the secondary Λ and $\overline{\Lambda}$ from these decays do not point back to the primary vertex. The effect of secondary contamination in the raw Λ ($\overline{\Lambda}$) yield is highlighted in Figures 8.15 and 8.16, because while the raw data distributions include secondary Λ and $\overline{\Lambda}$, the embedding only contains primary Λ and $\overline{\Lambda}$.

Figure 8.17 shows how the DCA distribution of the Λ to the primary vertex compares between what is seen in the raw data, and those from Λ, Ξ^-, Ξ^0 and Ω^- embedding.

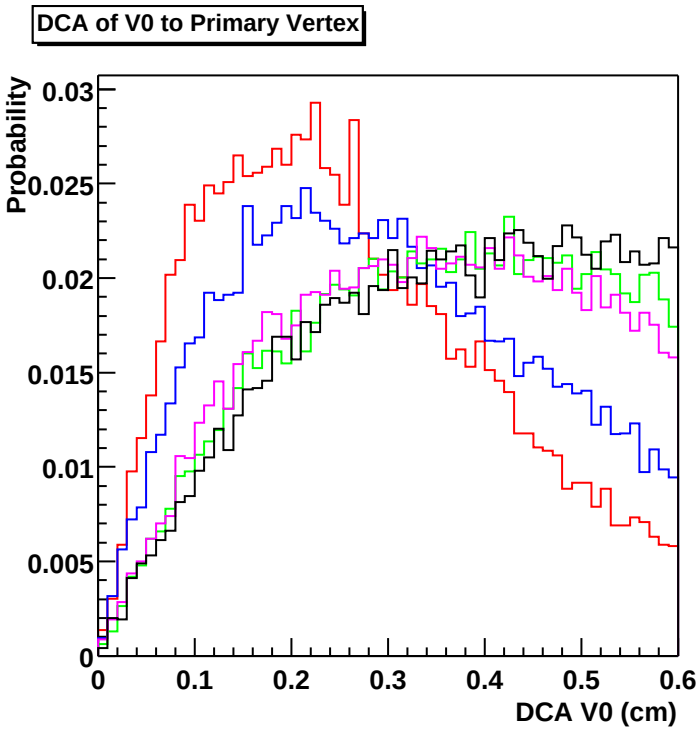

Figure 8.17: Distributions of the DCA of the Λ to the primary vertex. The blue distribution represent the reconstructed raw data, the red distribution is for the reconstructed primary Λ embedding data, the green, black and magenta distributions represent reconstructed Λ from Ξ^-, Ξ^0 and Ω^- embedding respectively.

It can be seen that the magnitude of the broadening of the measured distribution in the raw data is dependent upon the number of reconstructed primary and secondary Λ and $\overline{\Lambda}$. It is therefore not a systematic error and is simply a feed-down effect. This is discussed in more detail in section 8.2.6.

8.2.5 Comparison of MC and Data in Azimuth

Any differences between the MC and the data due to different detector effects can be seen when plotting particle yields as a function of the azimuthal angle, ϕ. By doing this, and by splitting the data into positive and negative z values, 24 different phi bins can be selected which correspond to each of the individual super-sectors of the TPC, (see section 5.2.1.1). A comparison can be made between the raw particle yields in each phi bin, and the yields of reconstructed and associated particles from the embedding data, which are used to correct the raw yields. Figure 8.18 shows these distributions for the K^0_S, Λ and $\overline{\Lambda}$ respectively, where the embedding data (black) was scaled so that the data in bin 1 corresponded to the same value as the raw yield point (red).

On the whole, the two datasets match well, but there are areas where this is not the case (differences $\sim 20\%$). The probable reason for the discrepancies that are visible is hardware failures in the TPC. At times during the data-taking period, some read-out boards failed and were removed from the data-acquisition, however, the simulation did not take these into account. In order to determine the effect on the yield these differences have, the dN/dϕ was calculated as a function of ϕ. Due to limiting statistics, a correction corresponding to the most central 10% of the data was applied, and the data was split into 8 different ϕ bins. Figures 8.19 and 8.20 show the results of this for the K^0_S and the Λ and $\overline{\Lambda}$ particles respectively.

It can be seen that the dN/dϕ distributions of the K^0_S and the $\overline{\Lambda}$ are approximately flat as a function of ϕ, whilst the Λ distribution is also approximately flat, apart from one bin which is $\sim 20\%$ higher than the others.

Although in the case of the Λ the dN/dy in one ϕ bin is greater than the rest, the distributions on the whole are consistent with being flat. It is therefore assumed that they do not make any contribution to the systematic error.

As seen in the analysis of the uncorrected $\overline{\Lambda}$ /Λ ratio, one possible source of a systematic error is the fact that the two halves of the TPC are in essence separate detectors. Table 8.6 shows the values of dN/dy for the K^0_S, Λ and $\overline{\Lambda}$ when only considering vertices in each half of the detector. The values in the final column are what was presented earlier.

The discrepancies that existed in the case of the $\overline{\Lambda}$ /Λ ratio are no longer seen

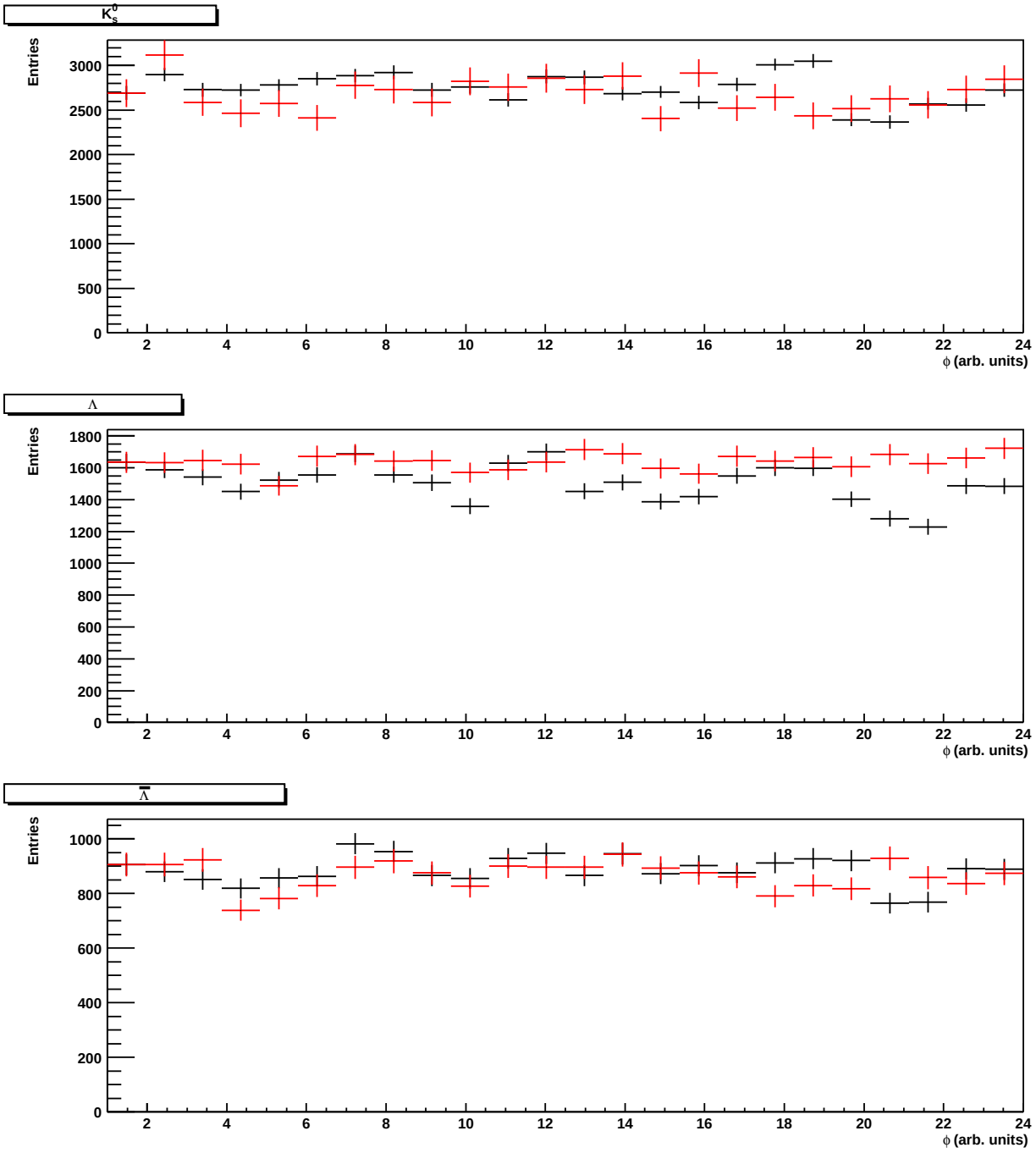

Figure 8.18: The variation in the yield as a function of ϕ for both the raw data (black) and the reconstructed and associated embedding data (red) in the case of the K^0_S (top), Λ (middle) and $\overline{\Lambda}$ (bottom). The embedding data has been scaled so that the data in bin 1 agree.

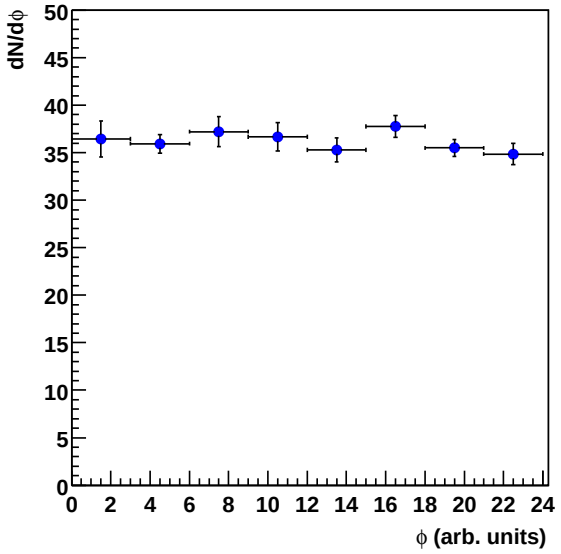

Figure 8.19: dN/dϕ as a function of ϕ for the K^0_S.

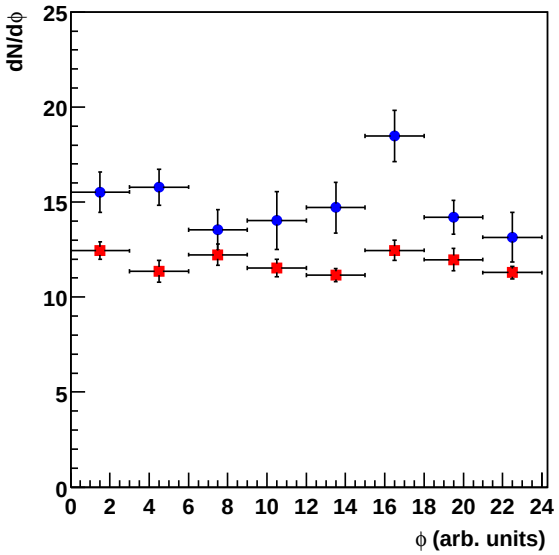

Figure 8.20: dN/dϕ as a function of ϕ for Λ (blue) and $\overline{\Lambda}$ (red).

Particle	Negative z	Positive z	All z
K^0_S	36.00 $\pm$ 0.88	35.58 $\pm$ 0.73	35.22 $\pm$ 0.73
Λ	17.15 $\pm$ 0.45	16.51 $\pm$ 0.38	16.85 $\pm$ 0.35
$\overline{\Lambda}$	12.37 $\pm$ 0.33	12.19 $\pm$ 0.26	12.29 $\pm$ 0.26

Table 8.6: The yields of the K^0_S, Λ and $\overline{\Lambda}$ as a function of the z position of the primary vertex.

when calculating the corrected yield of each particle, and hence this does not contribute to the systematic error.

Apart from systematically varying the cut values and recalculating the yield which leads to errors of $<0.2\%$, the only other source or systematic errors comes from the raw signal extraction. Although the Gaussian fits did not describe the Λ and $\overline{\Lambda}$ data well, the bin counting method that was employed relies on the assumption that the background around the peak is linear. In order to calculate the error from this, the standard deviation of all the different methods of signal extraction (Gaussian, Double Gaussian and bin counting) was calculated in each p_t bin. The means of these values were then assumed to represent the systematic errors, and

these are listed in Table 8.7.

Particle	Systematic Error on Yield
K^0_S	10.5 %
Λ	5.4 %
$\overline{\Lambda}$	5.1 %

Table 8.7: The systematic errors determined on the dN/d**y** for the K^0_S, Λ and $\overline{\Lambda}$ respectively.

8.2.5.1 Lifetime Calculation

Another consistency check between the data and the simulation that can be performed is a lifetime calculation. This involves a full correction for acceptance and efficiency and has the advantage that the mean lifetimes of all the particles are known [2]. In order to perform the correction, the data and the correction factors were divided into momentum-lifetime bins. The correction was done in two-dimensions as the measured decay length of a particle depends on the momentum. To have made the correction in only one dimension would have required that the MC and the real data had the same momentum distribution. The two dimensional correction is independent of the momentum distribution used in the MC. The lifetime of each particle is calculated using the relationship in equation 8.10,

$$c\tau = m * \frac{l}{p} \tag{8.10}$$

where $c\tau$ is the mean lifetime of the particle (measured in cm), m the mass, l the decay length and p the total momentum. Both l and p are determined experimentally, and the correct value of the mass (i.e., not the measured value) is used (taken from [2]).

In the lifetime calculation for all 3 particles, the bin counting method was used to extract the raw yield in each p-$c\tau$ bin. This was necessary in the case of the K^0_S as the statistics in each bin were too small to allow a reliable fit, due to the number of bins used.

Figure 8.21 shows the background subtracted yield per event distribution in p-$c\tau$ bins, for all collision centralities. It shows that for all particles, the data was concentrated at lower values of both p and $c\tau$, though the ranges covered by the K^0_S and $(\overline{\Lambda})\Lambda$ were different.

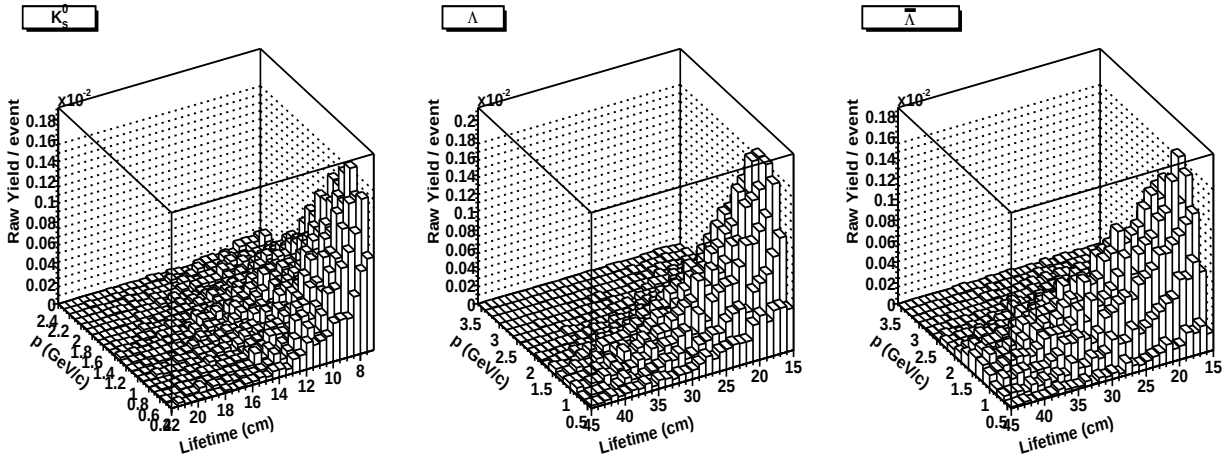

Figure 8.21: Distribution of raw data in p-$c\tau$ bins for the K^0_S, Λ and $\overline{\Lambda}$.

The combined acceptance and efficiency corrections that were applied to this are shown in Figure 8.22, again in the same p-$c\tau$ bins, where the correction is defined in equation 7.8.

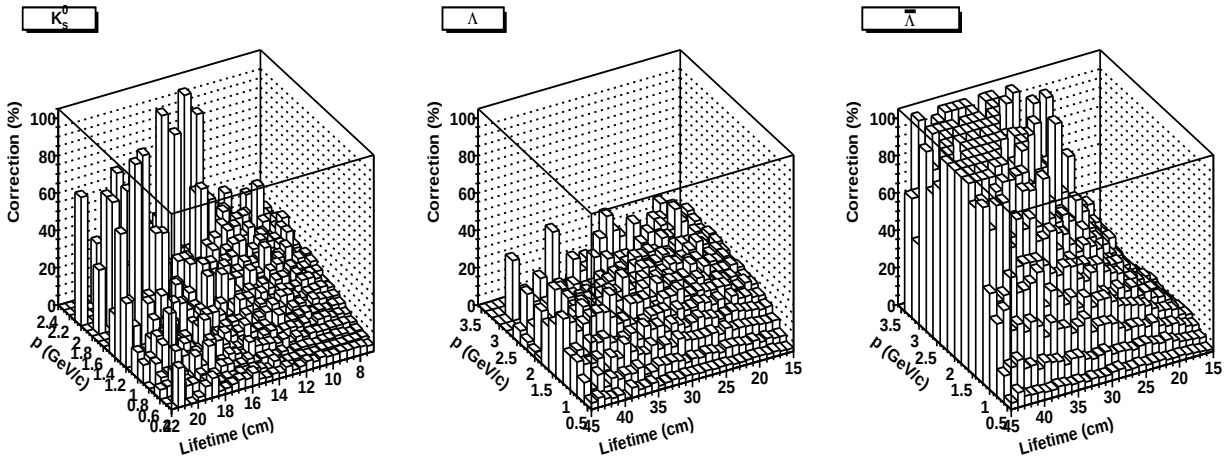

Figure 8.22: Total correction factors in the relevant p-$c\tau$ bins for the K^0_S, Λ and $\overline{\Lambda}$.

The corrected yield in each bin was obtained by dividing the data in Figure 8.21 by the correction factor in Figure 8.22. At this point, a projection was made over all

the momentum bins, onto the lifetime axis. Once this had been done, the data was fit with an exponential decay formula, as given in equation 8.11.

$$N(\tau) = N_0 * e^{-\tau/\tau_0} \tag{8.11}$$

where N_0 represents the initial number of particles, τ the lifetime, and τ_0 the mean lifetime, the constant whose determination is the aim of this particular analysis. The corrected lifetime distributions, along with the respective fits for the K^0_S, Λ and $\overline{\Lambda}$, are shown in Figure 8.23, whilst the values of the mean lifetime, obtained from the fits are given in Table 8.8.

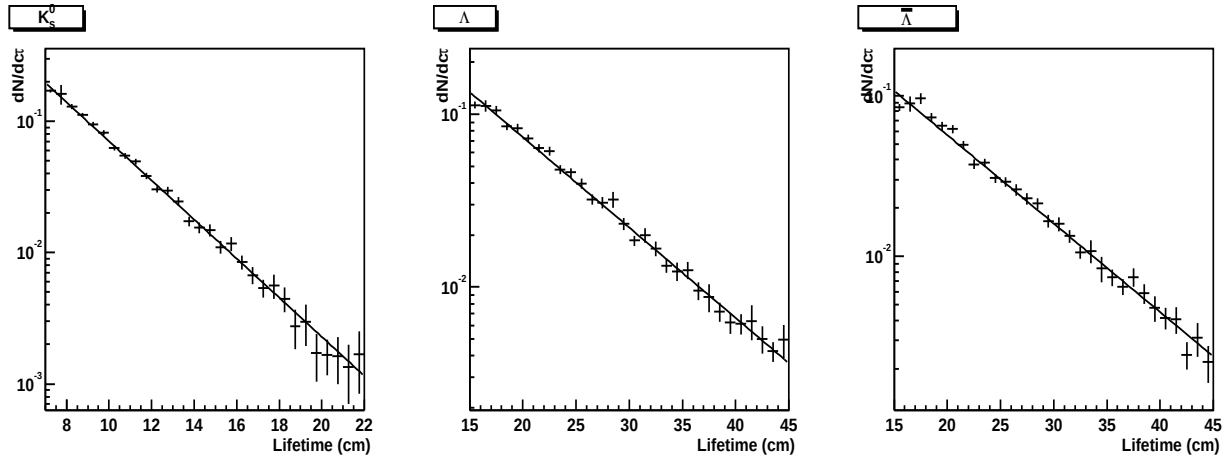

Figure 8.23: The corrected $c\tau$ distributions for the K^0_S, Λ and $\overline{\Lambda}$, along with a fit to equation 8.11

Particle	Measured $c\tau$	Expected $c\tau$
K^0_S	(2.82 $\pm$ 0.03) cm	2.68 cm
Λ	(8.03 $\pm$ 0.11) cm	7.89 cm
$\overline{\Lambda}$	(7.79 $\pm$ 0.12) cm	7.89 cm

Table 8.8: The measured and expected values of $c\tau$ for the K^0_S, Λ and $\overline{\Lambda}$.

As can be seen, the measured values of the lifetime do not agree completely with the expected value, though the large errors on the Λ and $\overline{\Lambda}$ correction mean that the results are within 2 and 1 σ of the expected value respectively. The differences in the

measurements highlight the fact that the MC does not exactly reproduce the data. Another factor that needs to be taken into account for the Λ and $\overline{\Lambda}$ measurement is the effect of secondary particles. The raw data contains Λ and $\overline{\Lambda}$ from multi-strange particle decays, whilst the simulation only contains primary Λ and $\overline{\Lambda}$, and therefore some discrepancy is expected, unless the primary and secondary Λ and $\overline{\Lambda}$ have the same momentum distributions.

8.2.6 Feed-down Correction

As discussed in section 8.2.4.1, when noting the differences in the DCA of the V0 to the primary vertex distributions between the MC and raw data, the measured yields of Λ and $\overline{\Lambda}$ hyperons that are quoted in Tables 8.4 and 8.5 do not represent all primary particles as some of them come from feed-down contributions in weak decays of multi-strange (anti)baryons. Therefore, whenever quoting measured yields or measuring particle ratios, it is important that the size of the feed-down contribution is taken into account.

The contribution of the secondary Λ hyperons in the measured yields can be categorised by equation (8.12), where N_{Λ}^{T} is the total number of Λ as given in Table 8.4, ϵ_{Λ}^{p} is the efficiency for finding a primary Λ, N_{Λ}^{p} the number of primary Λ, ϵ_{Λ}^{s} the efficiency for finding a secondary Λ, and N_{Λ}^{s} is the number of secondary Λ.

$$\mathrm{N}_{\Lambda}^{T} = \frac{\epsilon_{\Lambda}^{p}\mathrm{N}_{\Lambda}^{p} + \epsilon_{\Lambda}^{s}\mathrm{N}_{\Lambda}^{s}}{\epsilon_{\Lambda}^{p}} \tag{8.12}$$

In order to calculate the number of primary Λ, equation (8.13) can be used, which is just a manipulation of equation (8.12).

$$\mathrm{N}_{\Lambda}^{p} = \frac{\epsilon_{\Lambda}^{p}\mathrm{N}_{\Lambda}^{T} - \epsilon_{\Lambda}^{s}\mathrm{N}_{\Lambda}^{s}}{\epsilon_{\Lambda}^{p}} \tag{8.13}$$

As the factors $\epsilon_{\Lambda}^{p}\mathrm{N}_{\Lambda}^{T}$ and ϵ_{Λ}^{p} are known, only $\epsilon_{\Lambda}^{s}\mathrm{N}_{\Lambda}^{s}$ needs to be determined in order to calculate N_{Λ}^{p}. It is relatively straightforward to calculate the factor $\epsilon_{\Lambda}^{s}\mathrm{N}_{\Lambda}^{s}$ by examining embedding data for both Ξ^{-} and Ξ^{0}, which both decay via a Λ. Although another source of secondary Λ comes from the triply strange Ω^{-}, this is assumed to be negligible in this analysis, as at CERN energies the Ω^{-} yield was found to be approximately one tenth of the Ξ^{-} yield [104]. By applying the final Λ finding cuts to the embedding data, and by only counting the reconstructed Λ that are matched with

a MC Λ, a p_t distribution of secondary Λ can be obtained. By scaling the mean Ξ^- and Ξ^0 yields per event in the embedding data by the value of the corrected measured Ξ^- yield, a realistic distribution of secondary Λ can be obtained. The only measurement of the Ξ^- yield undertaken so far has been for the top 14 % of the cross-section (dN/dy = 3.07 $\pm$ 0.13 [107]), due to limited statistics, therefore the feed-down correction can only be reliably calculated for this particular centrality bin.

The results obtained from this method, presented in Table 8.9 for the most central 14 % collisions in the rapidity interval |y | $<$ 0.5, show that the feed-down effect is quite significant, at a value of (22.3 $\pm$ 2.3) %.

System	dN/dy
N_Λ^T	14.52 $\pm$ 0.24
N_Λ^p	11.28 $\pm$ 0.23
N_Λ^s	3.24 $\pm$ 0.33

Table 8.9: The secondary contamination of the measured Λ yields.

Note that this estimate is only for contributions from Ξ^- and Ξ^0 and there will necessarily be a contribution from the triply strange Ω^-, which decays through the $\Lambda + K^-$ channel with a branching ratio of 68 %, and the rest of the time through the Ξ^- and Ξ^0. However, as there has as yet been no measurement of Ω^- yields at this energy, the process applied to determine the Ξ^- and Ξ^0 contributions cannot be performed for the Ω^-. However, making the assumption that $\Omega^-/\Xi^- \simeq \Xi^-/\Lambda$, as was the case at SPS energies [104], then the Ω^- contribution to the feed-down would be approximately 2 %. It can be shown that the contribution to the primary Λ yield from Ω^- is small by examining once again the DCA of the Λ to the primary vertex distributions from Figure 8.17. If the primary Λ only and the secondary Λ from Ξ^- decays are suitably scaled and summed, it can be shown that this distribution now approximates well to the distribution observed in the raw data, as shown in Figure 8.24. The small discrepancy between the distributions can be attributed to the feed-down contribution from Ω^- which has not been calculated.

As no embedding has been performed for the $\overline{\Xi^+}$ or $\overline{\Xi^0}$, then the feed-down contribution to the $\overline{\Lambda}$ yield can not be calculated explicitly. However, as the distribution of the DCA of the $\overline{\Lambda}$ to the primary vertex is approximately the same as that of the Λ

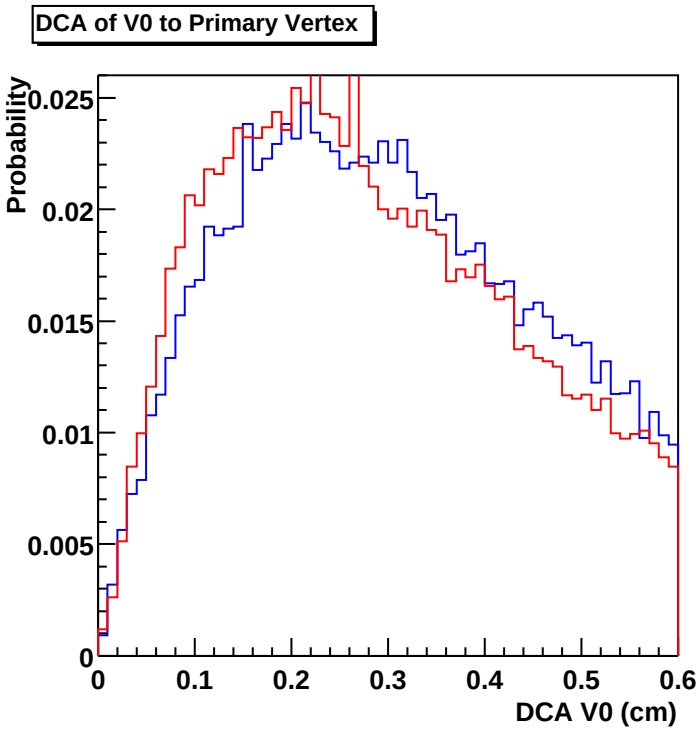

Figure 8.24: Distributions of the DCA of the Λ to the primary vertex. The blue distribution represent the reconstructed raw data, the red distribution is for the suitably scaled and summed primary Λ embedding and Λ from Ξ^- embedding.

(Figures 8.15 and 8.16 respectively), the feed-down contamination can be assumed to be approximately the same as the Λ. The only caveat with this is that the $\overline{\Xi^+}/\Xi^-$ ratio is different to the $\overline{\Lambda}/\Lambda$ ratio. However, as this difference is small (~ 0.87 [107] compared to ~ 0.74), the effect of the feed-down contribution to the $\overline{\Lambda}/\Lambda$ ratio is expected to be small.

Chapter 9

Discussion of Results

9.1 $\overline{\Lambda}/\Lambda$ Ratio

As discussed in section 8.1, the value of the anti-baryon/baryon ($\overline{B}$/B) ratios are determined by the amount of baryon stopping in the collision. From these ratios, the fugacities and hence the value of the baryo-chemical potential (μ_B) can be extracted, as detailed in section 4.2.

A thermal analysis of all RHIC $\overline{B}$/B ratios, as well as other particle ratios, has shown that μ_B = 46 $\pm$ 5 MeV, and the chemical freeze-out temperature (T) = 174 $\pm$ 7 MeV [108]. A separate thermal analysis has been conducted which finds μ_B = 41 $\pm$ 5 MeV and T = 165 $\pm$ 7 MeV [109], which is in agreement with the previous result. These chemical freeze-out temperatures are only slightly higher than what was observed at the CERN SPS (T = 168 $\pm$ 5 MeV), whilst μ_B has decreased from $\sim$ 270 MeV [110]. These results are plotted on Figure 9.1, which shows that in the higher energy collisions, the fireball region that is created is close to being net-baryon free.

The $\overline{B}$/B ratio is expected to increase with increasing strangeness content of the baryon, as the number of valence quarks in the baryon that have to be created, increases. This is observed in STAR when measuring the $\overline{p}/p$ (|S|=0), (0.65 $\pm$ 0.08) [112], $\overline{\Lambda}/\Lambda$ (|S|=1), (0.736 $\pm$ 0.03) and the $\overline{\Xi^+}/\Xi^-$ (|S|=2), (0.87 $\pm$ 0.04) [113] ratios at mid-rapidity. The ratios are measured for the most central 11 $\%$ of the cross-section but are not corrected for feed-down. As discussed in section 8.2.6, the feed-down contribution to the ratios is expected to be small. These values are represented on Figure 9.2. Also shown are the $\overline{p}/p$ ratios from the NA44 [114] and NA49 [60]

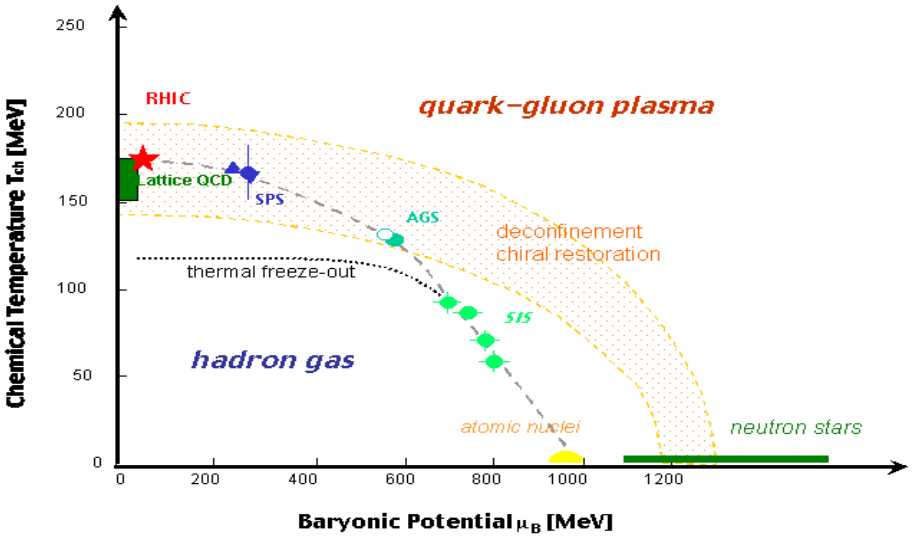

Figure 9.1: The Phase diagram of nuclear matter, plotting the baryonic chemical potential (μ_B) against Temperature. The results of a thermal analysis of RHIC (red) and SPS (blue) data are plotted on the figure (modified from the figure in [111]).

CERN experiments, and the $\overline{\Lambda}/\Lambda$ and $\overline{\Xi^+}/\Xi^-$ results from WA97 [67], all from mid-rapidity and at the lower energy of $\sqrt{s_{NN}}$ = 17.3 GeV.

An interesting feature of Figure 9.2 is that there is a linear increase in the ratios, as the strangeness content of the baryons increase. This can be described in terms of quark coalescence models [71] [115], which predict that the ratios are proportional to the number of produced quarks of a given flavour within the fireball. Using this relationship, one can simply count the available quarks in the $\overline{\text{B}}$/B ratios, and obtain predictions for the K^+/K^- ratio, as given in equation (9.1), where D_c is defined as the coalescence parameter.

$$D_c = \frac{u\overline{s}}{\overline{u}s} = \frac{K^+}{K^-} = \frac{\overline{\Lambda}(\overline{u}\overline{d}\overline{s})}{\Lambda(uds)} \times \frac{p(uud)}{\overline{p}(\overline{u}\overline{u}\overline{d})} = \frac{\overline{\Xi^+}(\overline{d}\overline{s}\overline{s})}{\Xi^-(dss)} \times \frac{\Lambda(uds)}{\overline{\Lambda}(\overline{u}\overline{d}\overline{s})} \tag{9.1}$$

Therefore by using measured experimental values for the $\overline{\Xi^+}/\Xi^-$, $\overline{\Lambda}/\Lambda$ and $\overline{\text{p}}$/p ratios, estimates of the D_c parameter can be made. In equation (9.2), the large error in the $\frac{\overline{\Lambda}/\Lambda}{\overline{p}/p}$ ratio comes from the systematic uncertainty in the $\overline{p}/p$ ratio.

$$D_c = \frac{\overline{\Lambda}/\Lambda}{\overline{p}/p} = 1.13 \pm 0.15 \tag{9.2}$$

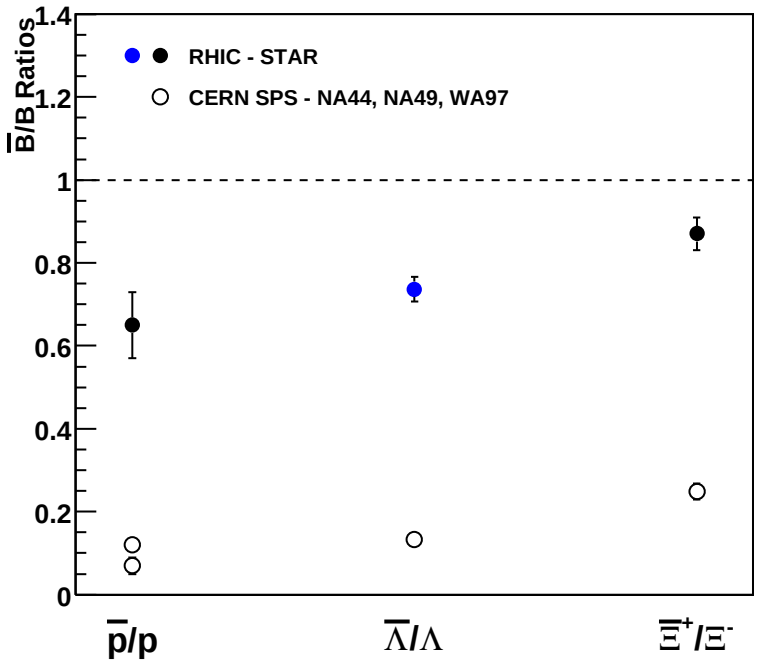

Figure 9.2: The $\overline{\text{B}}$/B ratios for baryons with increasing |S| at mid-rapidity both in STAR at $\sqrt{s_{NN}}$ = 130 GeV, and from various experiments at CERN energies of $\sqrt{s_{NN}}$ = 17.3 GeV. The blue data-point represents the $\overline{\Lambda}/\Lambda$ ratio from this thesis.

$$D_c = \frac{\overline{\Xi^+}/\Xi^-}{\overline{\Lambda}/\Lambda} = 1.18 \pm 0.07 \tag{9.3}$$

These predictions can be compared to the K^+/K^- ratio measured by STAR, in the same acceptance region as the other measurements. In an independent analysis, the K^+/K^- ratio was found to be 1.14$\pm$0.02$\pm$0.05 [113].

The good agreement between the measured K^+/K^- ratio and the prediction of D_c obtained from the measured $\overline{\text{B}}$/B ratios means that this simple quark counting, or coalescence, method describes and predicts the ratios well. It has also been shown that this method of quark counting cannot be used to describe data from p+Pb collisions at the CERN SPS [115]. However, it is important to note that the coalescence model does not assume an equilibrated system, nor does it make an assumption as to how the quark matter, prevalent prior to hadronisation, is formed.

Within a thermal model approach, where an equilibrated system is assumed to have formed, the double ratios are also expected to be constant. The coalescence

parameter, D_c, can then be formulated in terms of the quark fugacities, and is given in equation (9.4). From these fugacities, the baryo-chemical potential (μ_B), strangeness chemical potential (μ_s) and temperature (T) can be determined.

$$\begin{aligned} D_c &= \lambda_u^2.\lambda_s^{-2} \\ &= \exp\left[(2\mu_B - 6\mu_s)/3\mathrm{T}\right] \end{aligned} \tag{9.4}$$

Using the assumption of local strangeness conservation, μ_s can be assumed to be zero. Therefore, substituting the values for μ_B and T given earlier, D_c can be calculated and is found to be approximately 1.19 and 1.18 respectively.

As the relationships between the ratios are predicted equally well in both coalescence and thermal models, they cannot be used to distinguish between the different models.

9.2 Corrected Spectra

9.2.1 Inverse Slopes

The inverse slopes of the corrected particle yields, outlined in Tables 8.3, 8.4 and 8.5, show two phenomena. The inverse slope of the K_S^0 is approximately 50 MeV lower than the slopes of the Λ and $\overline{\Lambda}$, whose slopes are the same within the stated errors. For all three particle species, the inverse slope is approximately constant for the four most central bins (0 to 35% of the cross-section), and then falls off significantly in the most peripheral bin, as shown in Figure 9.3.

The difference of $\sim$ 50 MeV between the measured inverse slopes of the K_S^0, compared to the slopes of the Λ and $\overline{\Lambda}$ is consistent with what was measured at the SPS. Figure 9.4 shows a comparison between inverse slopes measured at the SPS [116] [65] [117] and those measured at RHIC [118] [119] [107]. Therefore when the K_S^0, Λ and $\overline{\Lambda}$ slopes are coupled with the rest of the data, the observed mass dependence of the inverse slopes can be interpreted as being due to a significant amount of radial flow build up during the collision, and is independent of whether a partonic phase is produced or not.

The drop in the inverse slope parameter with decreasing centrality for a particular particle species is in itself difficult to explain. However, this is a common feature

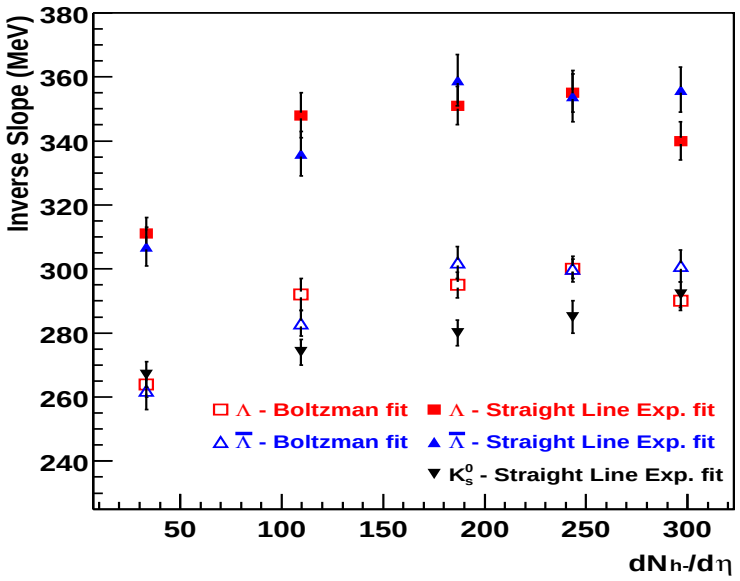

Figure 9.3: The inverse slope parameters of the K^0_S, Λ and $\overline{\Lambda}$ as a function of centrality. Both the Boltzmann and straight line exponential points are shown for the Λ and $\overline{\Lambda}$.

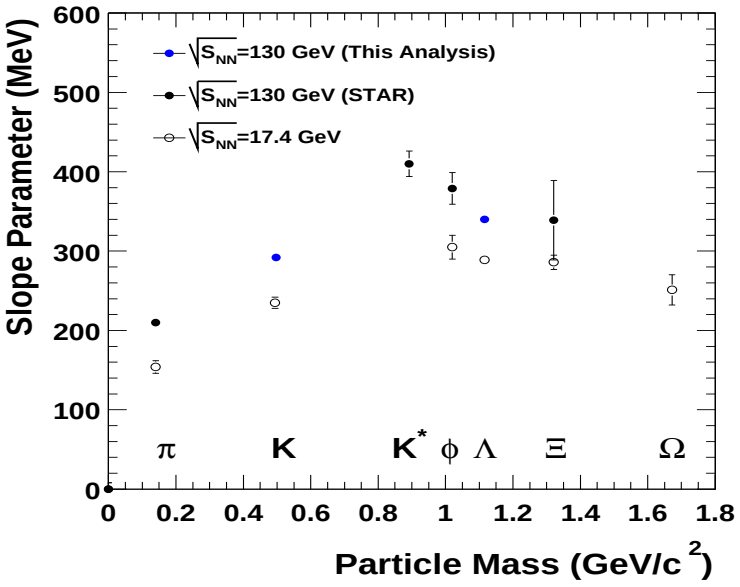

Figure 9.4: Inverse slopes of data from Pb+Pb collisions at the SPS and Au+Au collisions at RHIC. The slopes from this analysis are shown by blue points. For consistency, all errors shown are statistical only.

for the Λ, $\overline{\Lambda}$ and K^0_S in this analysis, as well as the measured $\overline{p}$ spectra in STAR [120]. Therefore it may be an indication of reduced collective radial flow in the more peripheral collisions, assuming that the freeze-out temperature remains constant. This is an intuitive picture as it would be expected that smaller pressure gradients would be built up in the more peripheral collisions due to the smaller volume, as well as the reduced number of participating nucleons and produced particles.

9.2.2 Particle Yields

The value of the $\overline{\Lambda}/\Lambda$ ratio for the efficiency corrected data can be calculated as a function of centrality from Tables 8.4 and 8.5, and this is presented in Figure 9.5.

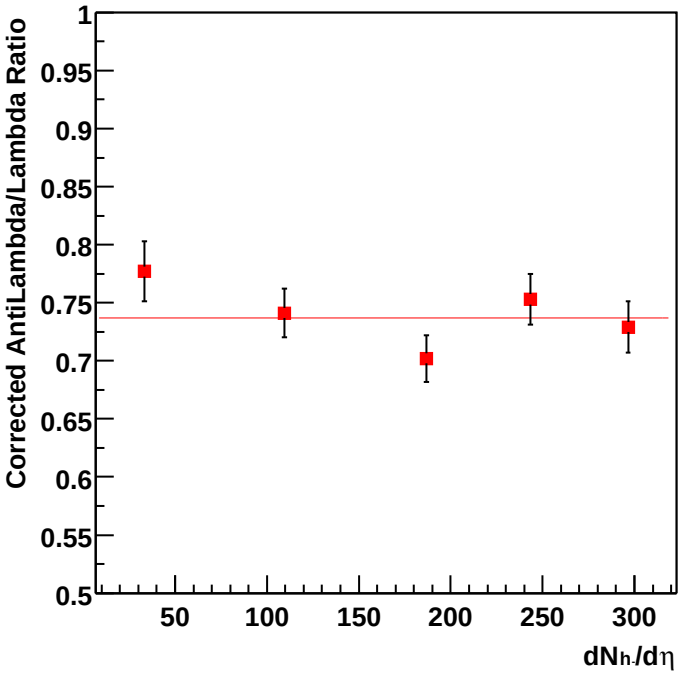

Figure 9.5: The corrected value of the $\overline{\Lambda}/\Lambda$ ratio as a function of centrality. The horizontal line is a fit to the data.

The ratio is flat within the calculated errors, and a linear fit to the data gives an integrated ratio of 0.737 ± 0.010, as given in Table 9.1. The average values of the corrected and uncorrected ratios are in excellent agreement with each other, which justifies the earlier assumption that apart from any absorption effects, the correction factors for the $\overline{\Lambda}$ and Λ should be equal.

	$\overline{\Lambda}/\Lambda$ Ratio
Uncorrected	0.736 ± 0.008
Corrected	0.737 ± 0.010

Table 9.1: The average values of the $\overline{\Lambda}/\Lambda$ ratio when uncorrected and corrected for efficiency, but not for feed-down.

The expected increase of the K^0_S, Λ and $\overline{\Lambda}$ yields with increasing collision centrality is observed in all cases, and is presented graphically in Figure 9.6. The yield has been divided by the average yield per unit pseudo-rapidity (η) (in the range $|\eta|$ <0.5 of all negative primary particles, (the π^-, $\overline{p}$ and K^-), denoted as h^-, measured in the same centrality bins [101]. The reason that η - which is defined in Appendix A - is used instead of y, in the case of the h^-, is that only the charge and momentum of the particles are known, and therefore their energies cannot be calculated.

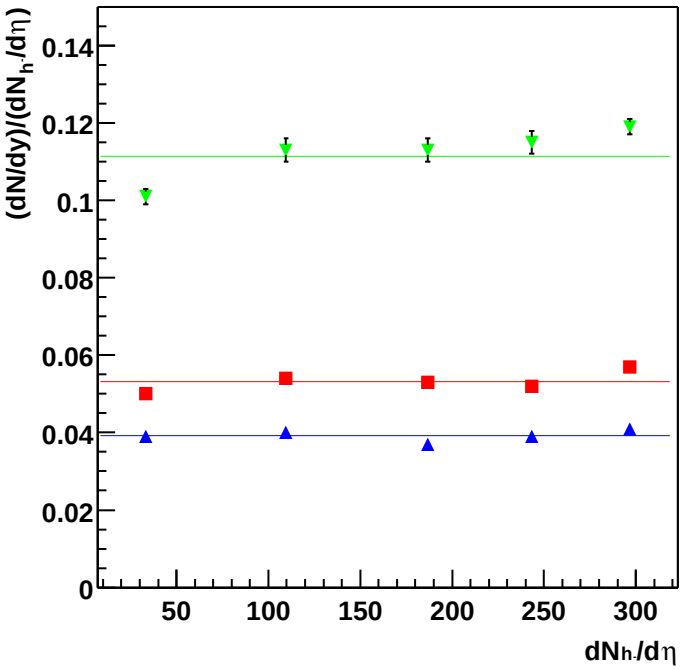

Figure 9.6: The ratio of the measured dN/dy of K^0_S (green), Λ (red) and $\overline{\Lambda}$ (blue) to the measured h^- $dN/d\eta$ for the five centrality bins. The error bars include the calculated systematic errors.

The presented ratios are flat with increasing h^- yield, although there is a slight suggestion of an increase over and above the constant trend in the most central collisions, most notably for the K^0_S. This leads to the suggestion that strangeness production is proportional to the volume of the system, and no clear change in this is observed. The average relationships between the yields are given in Table 9.2, and compared to published data from Pb+Pb collisions ($\sqrt{s_{NN}}$ = 17.3 GeV) at the SPS, taken at mid-rapidity, which are corrected for feed-down [104].

Particle	$\frac{dN_{V0}/d\mathbf{y}}{dN_{h-}/d\eta}$		
	Uncorrected	Corrected	SPS data
K^0_S	$(0.112 \pm 0.001)h^-$		$(0.138 \pm 0.013)h^-$
Λ	$(0.053 \pm 0.001)h^-$	$(0.041 \pm 0.002)h^-$	$(0.086 \pm 0.005)h^-$
$\overline{\Lambda}$	$(0.039 \pm 0.001)h^-$	$(0.030 \pm 0.001)h^-$	$(0.011 \pm 0.001)h^-$
K^0_S +Λ +$\overline{\Lambda}$	$(0.204 \pm 0.002)h^-$	$(0.183 \pm 0.002)h^-$	$(0.235 \pm 0.014)h^-$

Table 9.2: The relationship between the average K^0_S, Λ and $\overline{\Lambda}$ yields and the h^- yield, presented from this analysis and compared to published data from the SPS. Values for the ratios are given before and after the feed-down correction is applied using the assumption that the feed-down correction is the same for the Λ and the $\overline{\Lambda}$.

When making a comparison to the SPS data, it is observed that the Λ /h^- is lower, whilst the ratio of $\overline{\Lambda}$ /h^- is much greater. This can be explained by the fact that μ_B, the baryo-chemical potential which is a measure of the net-baryon density, has decreased significantly in going from SPS to RHIC energies. Therefore, at the lower energies, baryon production is strongly favoured over anti-baryon production. When combining the Λ, $\overline{\Lambda}$ and K^0_S yields, it is seen that there is a significant decrease ($\sim$ 20$\%$) in the $<\Lambda + \overline{\Lambda} + K^0_S>$ /h^- ratio when going from SPS to RHIC.

Although this suggests that the strangeness production has fallen at the higher energy, the $<\Lambda + \overline{\Lambda} + K^0_S>$ /h^- ratio is only representative of three strange particles. It is observed in STAR that there is a significant increase in the yields of the Ξ^- and $\overline{\Xi^+}$ [107], ϕ [119] and K* [121] when comparing RHIC results with SPS. Therefore, in order to get a measure of the strangeness production, it is necessary to make a full measurement of all the strange particles, whereas at lower energies, a measurement of the kaons, Λ and $\overline{\Lambda}$ were a good approximation to the total strangeness yield.

9.2.2.1 Λ /π^+ Ratio

Braun-Munzinger $et.\ al.$ have calculated the dependence on the energy of the collision of the Λ /π^+ ratio [122]. It is more desirable to compare with pions as opposed to h^-, as for example, the h^- contains both baryons and mesons and is therefore dependent on the amount of baryon stopping, rather than just volume effects. For $\sqrt{s_{NN}}$ = 130 GeV, the prediction is Λ /$\pi^+ \simeq$ 0.038. Preliminary results for the corrected π^- yield (dN/dy) exist in STAR, but only results which correspond to the three most central bins in the Λ analysis are available [98]. The Λ /π^+ ratio can be calculated in this analysis using the π^- yield, under the assumption that π^- /$\pi^+ \sim$ 1 at RHIC, which is consistent with the value measured by the PHOBOS collaboration (π^- /π^+ = 1.00 $\pm$0.01$\pm$0.02) [123]. The mean value of the Λ /π^+ ratio in the three most central bins is 0.059 $\pm$ 0.001, with no obvious dependence on centrality, which reduces to 0.046 $\pm$ 0.002 after the feed-down correction has been applied. This is approximately 18 $\%$ higher than the model prediction.

Even though the measured ratio does not agree with the model prediction exactly, the general trend that is predicted of a decrease in the ratio between the SPS data and the new RHIC data is observed. The reason for this trend is due to the variation of μ_B, as in the case of the Λ /h^- ratio. The fact that the $\overline{\Lambda}$ /h^- (or $\overline{\Lambda}$ /π^+) yield rises with energy is then a natural consequence of the lowering of the value of μ_B, which means that the production of anti-baryons is less suppressed with increasing energy.

As well as thermal models, the quark coalescence model also makes predictions for the value of Λ /π^+, which is 0.08 [124]. This is approximately 74 $\%$ greater than the feed-down corrected value, as is shown in Table 9.3.

It is therefore observed that while both thermal and quark coalescence models predictions for the identical species ratios (e.g. $\overline{\Lambda}$ /Λ) agree with experimental values, neither model agrees with the experimental Λ /π^+ ratio, and therefore describes all of the data. It therefore appears that it is these non-identical particle ratios that are more powerful when discriminating between models. This is exemplified by the Ξ^- /π^+ ratio, where the Braun-Munzinger thermal model under-predicts the data by a factor of 2, whilst the quark coalescence model over-predicts the data by only 10 $\%$ [107] [125] [126]. This becomes even more apparent as the system evolves to a more baryon free state at higher energies, all the identical species ratios will be

Dataset	$\frac{dN_\Lambda/dy}{dN_{\pi^+}/dy}$
This analysis - no feed-down correction	(0.059 ± 0.001)
This analysis - with feed-down correction	(0.046 ± 0.002)
Thermal model	0.038
Coalescence model	0.08

Table 9.3: The Λ/π^+ ratios from this analysis and predictions from thermal and quark coalescence models, where the π^+ yield in this analysis was approximated by the π^- yield.

driven towards 1. The experimental error bars will then be too large to discriminate between model predictions.

9.2.2.2 Transverse Momentum Dependence of the $\overline{\Lambda}$ Yield

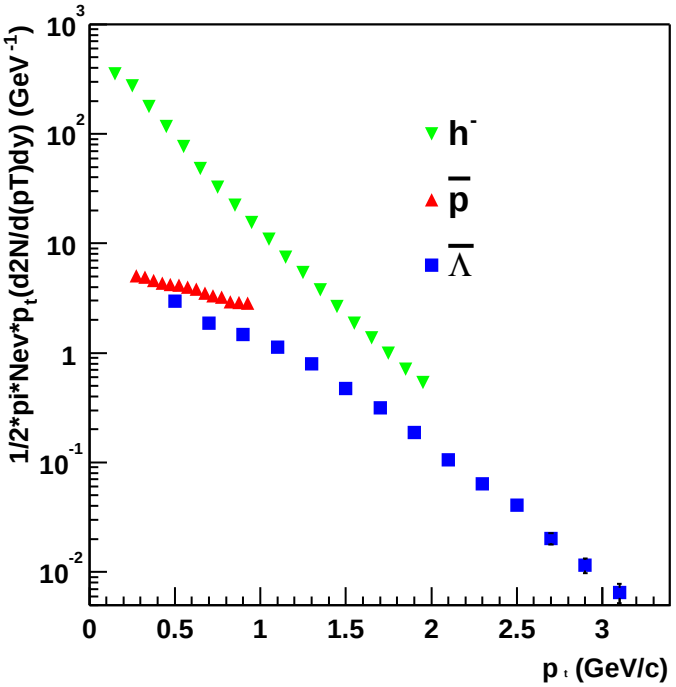

Figure 9.7: Comparison of measured p_t distributions for h^-, $\overline{p}$ and $\overline{\Lambda}$. There is clear evidence that the fraction of baryons to mesons increases at higher values of p_t.

Other interesting data pertaining to the $\overline{\Lambda}$ spectra are the yields as a function of p_t. If these yields are compared to h^- and $\overline{p}$ yields, so that a comparison is being made between anti-baryons and mesons, then it is clear that the anti-baryon to meson ratio increases as a function of increasing p_t. This trend is illustrated in Figure 9.7.

Although the p_t coverage of the $\overline{p}$ doesn't extend past 1 GeV/c, which therefore makes it difficult to extrapolate the distribution to higher momentum, the data from the $\overline{\Lambda}$ tentatively suggests that the anti-baryon yield is greater than the meson yield at moderately high p_t ($>$ 2 GeV/c), if one bears in mind that the h^- yield contains a contribution from the $\overline{p}$. This is an interesting observation which has also been reported by the PHENIX collaboration [127].

There are currently two different theoretical interpretations of this high-p_t phenomenon. The first interpretation is that it is simply a natural consequence of the radial expansion of the fireball [128]. This is observed in the mass dependence of the inverse slopes, where the more massive particles are observed to have a larger inverse slope and hence larger $<p_t>$. The data can also be explained by invoking the mechanism of jet quenching [129] [130] [85] and baryon junctions [131] [132] [133] with a small effect from radial flow. Jet quenching occurs as the jets, which are produced in the initial interactions (their production rate described by pQCD calculations), lose energy as they traverse the fireball due to interactions primarily with the gluons in the dense deconfined phase of matter. As jets will normally fragment into mesons, a suppression of mesons at higher p_t with respect to p+p collisions leads to a larger baryon/meson ratio. This suppression of mesons themselves at high p_t has been observed separately by both PHENIX [134] and STAR [101]. However, this quenching of jets will also lead to a suppression in the baryon yield at high-p_t. In order to explain the baryon yield, the method of baryon junctions are invoked. The assumption of baryon junctions is that the valence quarks do not each carry one third of the baryon number, but this is instead carried by a 'junction' of gluons inside the baryon, each connected to a valence quark and the junction. As each quark interacts, and produces more quarks via string fragmentation, there will always be one baryon formed from the three valence quarks. It is believed that in high energy A+A interactions, these baryon junction mechanisms are important for transporting baryon number over $\sim$ 5 units of rapidity to mid-rapidity [132], and they also lead to an enhancement of baryons at higher p_t [131].

This quenching of jets cannot happen if the fireball remains hadronic, as the gluon density is not large enough. This phenomena was not observed in collisions at the SPS, which suggests that either a deconfined phase was not formed, or that it was sufficiently short-lived so as not to affect the energy of the produced jets [135].

Currently, experimental data cannot distinguish between the two models. However, at higher p_t, differences in the models are predicted. For the thermal expansion model, as the mean-p_t of the baryons has been increased greater than that of the mesons due to their larger mass, the distributions cross once and at higher p_t, the baryon/meson ratio should remain greater than 1. In the jet quenching approach, it is predicted that the spectra cross again at $p_t \sim 5$ GeV/c, and the ratio decreases below 1, as particle production is dominated by the quenched jets compared to the baryon junction mechanism.

9.3 Conclusions

Although the full results from the first year of data taking at RHIC, involving Au+Au collisions at $\sqrt{s_{NN}}$ = 130 GeV have not emerged, enough data has been presented to provide a consistent picture of what is happening at this new energy. Data on $\overline{\Lambda}/\Lambda$ ratios describe the system which is created is almost baryon free. Fits to the data provide a baryon chemical potential of $\mu_B \simeq 46$ MeV and a freeze-out temperature of $\simeq 174$ MeV [108] [109].

As was the case at the SPS, the inverse slopes of the measured hadrons can be used to indicate the existence of radial flow in the collision. Figure 9.4 shows a comparison of inverse slope parameters extracted from a simple exponential fit (to aid comparison) from data at the SPS and at RHIC. The slopes at the SPS and RHIC are in good agreement, with the RHIC slopes being generally higher, which could indicate that the radial flow component is larger assuming a constant freeze-out temperature, which is indicated by the thermal analyses. The flattening off of the spectra for the higher mass strange particles is also observed within the stated error bars, though a measurement of Ω^- at this energy is not yet possible due to lack of statistics. The data presented in this thesis shows that the inverse slopes decrease (and hence the radial flow decreases) as a function of decreasing centrality of the collision, which indicate that the amount of the radial flow is a function of the centrality

of the collision.

The ratios of K^0_S /h^-, Λ /h^- and $\overline{\Lambda}$ /h^- are all flat as a function of increasing h^- yield. This is a continuation of the general trend observed at the SPS and suggests that the same production mechanisms of strangeness occur for all centralities under consideration (the 75% most central collisions). The comparisons of these ratios with model predictions show that the Λ /π^+ ratio is under-predicted ($\sim$ 20 %) by a thermal model, but over-predicted ($\sim$ 80 %) by a quark coalescence model, even though both models agree with the experimentally measured $\overline{\mathrm{B}}$/B ratios, which suggests that the models are too simplistic.

The data on yields of the $\overline{\Lambda}$ as a function of p_t shows a phenomena that isn't observed at lower energies, namely that the ratio of baryons to mesons exceeds 1 at high-p_t ($\geq$ 2 GeV/c). The current data lacks statistics at high p_t to be able to distinguish between simple radial flow and jet quenching. If experimental data follows the prediction of jet quenching at higher-p_t, in that the baryon to meson ratio falls below 1 again at $p_t \simeq$ 5 GeV/c, then this is an exciting result as jet quenching is a phenomena that $requires$ a deconfined nuclear medium.

The study of strangeness with respect to Quark-Gluon Plasma formation is motivated by its role as a plasma signature. Any enhancement in the yield must be with respect to a 'normal' yield, where a QGP isn't formed. This is usually taken to mean suitably scaled p+p and p+A collisions, where the volume of the system created is too small for a QGP to occur. As there are currently no data on p+p or p+A collisions at $\sqrt{s_{NN}}$ = 130 GeV, no statement can be made from the data in this thesis on any observed enhancement. This data can be used to study any enhancement effects, however, as soon as the reference data has been fully analysed.

9.4 Outlook

9.4.1 STAR

The data presented in this thesis was taken in the summer of 2000. Since that time, RHIC has provided Au+Au collisions at the top design energy of $\sqrt{s_{NN}}$ = 200 GeV. STAR has recorded $\sim$ 4 million central events and $\sim$ 5 million minimum bias events and has added extra detectors. Initial preliminary results at the higher energy sug-

gest that the net baryon density is even lower still ($\mu_B \sim 26.7$ MeV) [125]. The Silicon Vertex Tracker (SVT) [136], which comprises 3 layers of silicon between the beam pipe and the inner radius of the TPC has been installed, along with 2 forward TPCs, which extend the η coverage of STAR out to $\pm$ 4. The SVT in particular will help improve vertex resolution, both primary and secondary, which should make Ω^- reconstruction easier. With the volume of data taken in the latest Au+Au run, a full measurement of the Ω^- p_t spectrum should be possible, as well as increasing the p_t coverage of the Λ and $\overline{\Lambda}$ spectra, also helped by increasing the magnetic field strength by a factor of 2. This may allow the p_t spectra to reach out to 5 GeV/c and beyond, which is in the regime that the jet quenching models predict the baryon/meson ratio to turn over and fall below 1 again. Over the next few years, a full barrel electro-magnetic calorimeter will be installed, as well as a time-of-flight system which can aid with particle identification.

9.4.2 RHIC

At the end of the Au+Au data taking in November 2001, the collider started a programme of p+p collisions. These can be utilised in STAR as heavy-ion reference data, and used in particular in strangeness studies to determine the value of any enhancement that is observed.

Over the next few years, RHIC will be able to provide heavy-ion and proton beams for an estimated 37 weeks of the year, in principle providing large volumes of data to enable precision measurements of rare observables such as the Ω^- and the J/Ψ. This planned long running time can be utilised to perform an energy scan from $\sqrt{s_{NN}}$ = 17 GeV, which overlaps with CERN SPS energies, up to the top energy of $\sqrt{s_{NN}}$ = 200 GeV for heavy ions and $\sqrt{s_{NN}}$ = 250 GeV for protons, a process which has already begun. This will mean that data can be used to accurately describe a transition in detail, as well as providing p+p and p+A collisions for reference.

9.4.3 Future accelerators : Large Hadron Collider (LHC)

In approximately 2007, the LHC will begin operations at CERN, and whilst ostensibly a p+p collider, it will be utilised for approximately 4 weeks of the year to accelerate heavy ion beams to $\sqrt{s_{NN}} \sim 6$ TeV, more than an order of magnitude greater

then what can be achieved at RHIC [137]. With these higher energies the deconfined state may live for a long time, with high initial temperatures, perhaps high enough so that the temperature is comparable to the mass of the c quark. If this happens, then charm can be produced thermally, and charm production assumes the role of strangeness production at lower energies. These higher initial temperatures can also lead to a melting of the Υ ($b\overline{b}$) family of mesons, in an analogous way to the melting of the J/Ψ and the charmonia [138].

Appendix A

Terminology

Particles produced in Relativistic Heavy Ion collisions are classed in terms of variables which define where in the momentum space of the collision they were produced.

Rapidity (y) is a measure of the momentum of a particle in the longitudinal direction of the incident beam(s), and is given by equation (A.1).

$$\mathrm{y} = \frac{1}{2}\ln\left(\frac{\mathrm{E} + p_{||}}{\mathrm{E} - p_{||}}\right) \tag{A.1}$$

Here, E is the energy of the particle and $p_{||}$ is its momentum component in the longitudinal direction. It is a particularly useful quantity in that it is Lorentz additive, so distributions in rapidity do not change shape when changing from the laboratory frame to the Centre of Mass frame. By measuring the rapidity of a particle, one can determine where in momentum space within the fireball the particle was created. It is defined so that a particle created at rest in the centre of mass frame will have a rapidity of 0. A particle created by interactions among the primary beam particles will have a rapidity value close to that of the beam.

Other useful relations relating to rapidity are given in equations A.2 and A.3

$$p_{||} = m_t sinh\mathrm{y} \tag{A.2}$$

$$E = m_t cosh\mathrm{y} \tag{A.3}$$

where $p_{||}$ and E are the energy and momentum in the beam direction respectively. m_t is the transverse mass of the particle, and is defined in equation (A.4),

$$m_t = \sqrt{p_t^2 + m_0^2} \tag{A.4}$$

where m_0 represents the particle's rest mass and p_t is the momentum component of the particle perpendicular to the beam direction.

An analogous quantity to rapidity is pseudo-rapidity (η), which is defined in equation (A.5), where p is the total momentum of the particle.

$$\eta = \frac{1}{2} \ln \left(\frac{\mathrm{p} + p_{||}}{\mathrm{p} - p_{||}} \right) \tag{A.5}$$

$$= \ln(\cot \frac{\theta}{2}) \tag{A.6}$$

As it depends only on the kinematics of the particle, pseudo-rapidity is used as an alternative to rapidity when the mass of the particle is not known.

Appendix B

Papers

In line with the University of Birmingham regulations, it has to be shown that ...

”The Ph.D. thesis must contain an element which, if not already published, has been written to a standard and in the style judged suitable for publication in a medium appropriate to the discipline, which is of acceptable quality.”

To satisfy this regulation, I have included two papers over the next few pages. The first paper is a copy of the paper the author has submitted to the Journal of Physics G, which represents the proceedings of the plenary talk the author gave of his work at the Strangeness In Quark Matter 2001 conference. The second paper is the final draft of a paper on Λ and $\overline{\Lambda}$ production within STAR, which will be submitted to Physical Review Letters. This paper represents the analysis in this thesis and as such, the author of this thesis was one of the principal authors of the paper.

Bibliography

[1] M. Gell-Mann, Phys. Lett. **8**, 214 (1964).

[2] C. Caso *et al.*, Eur. Phys. J. C **3**, 1 (1998).

[3] D. H. Perkins, *Introduction to High Energy Physics (3rd Edition)* (Addison Wesley, 1987).

[4] D. J. Gross and F. Wilczek, Phys. Rev. Lett. **30**, 1343 (1973).

[5] H. D. Politzer, Phys. Rev. Lett. **30**, 1346 (1973).

[6] W. E. Burcham and M. Jobes, *Nuclear and Particle Physics* (Longman Scientific and Technical, 1995).

[7] A. C. Benvenuti *et al.*, Phys. Lett. B **223**, 490 (1989).

[8] S. Hahn, Nucl. Phys. B (Proc. Suppl.) **74**, 12 (1999).

[9] J. C. Collins and M. J. Perry, Phys. Rev. Lett. **34**, 1353 (1975).

[10] T. A. Yates, PhD Thesis, The University of Birmingham (unpublished) (1998).

[11] I. J. R. . Aitchison and A. J. G. Hey, *Gauge Theories in Particle Physics* (Adam-Hilger, 1989).

[12] K. G. Wilson, Phys. Rev. D **10**, 2445 (1974).

[13] F. Karsch, E. Laermann and A. Peikert, Preprint hep-lat/0012023 (2000).

[14] F. Karsch, Nucl. Phys. B (Proc. Suppl.) **83-84**, 14 (2000).

[15] F. Karsch, Nucl. Phys. A **698**, 199 (2002).

[16] S. Gottlieb *et al.*, Phys. Rev. D **47**, 3619 (1993).

[17] C.-Y. Wong, *Introduction to High-Energy Heaby-Ion Collisions* (World Scientific, 1994).

[18] A. Chodos *et al.*, Phys. Rev. D **9**, 3471 (1974).

[19] B. Muller, *The Physics of the Quark-Gluon Plasma* (Springer-Verlag, 1985).

[20] F. Karsch, Preprint hep-lat/9903031 (1999).

[21] I. R. Kenyon, *Elementary Particle Physics* (Routledge and Kegan Paul, 1987).

[22] T. Banks *et al.*, Preprint hep-ph/9403203 (1994).

[23] A. C. Irving *et al.*, Preprint hep-lat/01070323 (2001).

[24] J. D. Bjorken, Phys. Rev. D **27**, 140 (1983).

[25] T. Alber *et al*, (NA49 Collaboration), Phys. Rev. Lett. **75**, 3814 (1995).

[26] P. Carruthers and M. Duong-van, Phys. Rev. D **8**, 859 (1973).

[27] L. Ahle *et al.*, Phys. Rev. C **59**, 2173 (1999).

[28] B. B. Back *et al.*, J. Phys. G: Nucl. Part. Phys. **27**, 301 (2001).

[29] J. Bachler *et al*, (NA35 Collaboration), Phys. Rev. Lett. **72**, 1419 (1994).

[30] H. Appelshauser *et al*, (NA49 Collaboration), Phys. Rev. Lett. **82**, 2471 (1999).

[31] R. Hagedorn, Riv. Nuovo Cimento **6**, 1 (1983).

[32] B. Muller and P. Braun-Munzinger, http://www.cern.ch/HIPS .

[33] E. Schnedermann, J. Sollfrank and U. Heinz, Phys. Rev. C **48**, 2462 (1993).

[34] H. van Hecke *et al.*, Phys. Rev. Lett. **81**, 5764 (1998).

[35] J. Alam *et al.*, Phys. Rep. **273**, 243 (1996).

[36] F. D. Steffen and M. H. Thoma, Phys. Lett. B **510**, 98 (2001).

[37] M. M. Aggarwal *et al*, (WA98 Collaboration), Phys. Rev. Lett. **85**, 2595 (2000).

[38] P. Aurenche *et al.*, Eur. Phys. J. C **9**, 107 (1999).

[39] D. Y. Peressounko and Y. E. Pokrovsky, Preprint hep-ph/0009025 (2001).

[40] P. Huovinen, Preprint nucl-th/0111052 (2001).

[41] G. Domokos and J. I. Goldman, Phys. Rev. D **23**, 203 (1981).

[42] G. Akachiev *et al.*, Phys. Rev. Lett. **75**, 1272 (1995).

[43] B. Lenkeit for the CERES Collaboration, Nucl. Phys. A **661**, 23c (1999).

[44] G. E. Brown and M. Rho, Phys. Rev. Lett. **66**, 2720 (1991).

[45] S. Scherer *et al.*, Prog. Part. Nucl. Phys. **42**, 279 (1999).

[46] R. Rapp and J. Wambach, Preprint hep-ph/9909229 (1999).

[47] W. Cassing *et al.*, Phys. Rev. C **57**, 916 (1998).

[48] C.-Y. Wong and Z.-Q. Wang, Phys. Lett. B **367**, 50 (1996).

[49] T. Matsui and H. Satz, Phys. Lett. B **178**, 416 (1986).

[50] M. C. Abreu *et al*, (NA50 Collaboration), Phys. Lett. B **477**, 28 (2000).

[51] S. Gavin and R. Vogt, Phys. Rev. Lett. **78**, 1006 (1997).

[52] N. Armesto *et al.*, Nucl. Phys. A **698**, 583 (2002). (2001).

[53] R. L. Thewes *et al.*, J. Phys. G: Nucl. Part. Phys **27**, 715 (2001).

[54] J. Rafelski and B. Mueller, Phys. Rev. Lett. **48**, 1066 (1982).

[55] P. Koch *et al.*, Phys. Rep. **142**, 169 (1986).

[56] E. Shuryak, Phys. Rev. Lett. **68**, 3270 (1992).

[57] O. Hansen, Comments Nucl. Part. Phys. **20**, 1 (1991).

[58] L. Ahle *et al.*, Phys. Lett. B **476**, 1 (2000).

[59] J. C. Dunlop and C. A. Ogilvie, Phys. Rev. C **61**, 031901 (2000).

[60] F. Sikler *et al.* (NA49 Collaboration), Nucl. Phys. A **661**, 45c (1999).

[61] L. Ahle *et al.*, Phys. Rev. C **58**, 3523 (1998).

[62] C. Bormann for the NA49 Collaboration, J. Phys. G: Nucl. Part. Phys **23**, 1817 (1997).

[63] E. Anderson *et al*, (WA97 Collaboration), Phys. Lett. B **449**, 401 (1999).

[64] I. Bearden *et al*, (NA44 Collaboration), Phys. Lett. B **471**, 6 (1999).

[65] F. Antinori *et al*, (WA97 Collaboration), Eur. Phys. J. C **14**, 633 (2000).

[66] T. Susa for the NA49 Collaboration, Nucl. Phys. A **698**, (2001).

[67] R. Caliandro for the WA97 Collaboration, J. Phys. G: Nucl. Part. Phys **25**, 171 (1999).

[68] A. Bialas, M. Bleszynsky and W. Czyz, Nucl. Phys. B **111**, 461 (1976).

[69] D. K. Srivastava and K. Geiger, Phys. Lett. B **422**, 39 (1998).

[70] E. G. Ferreiro *et al.*, Phys. Lett. B **422**, 314 (1998).

[71] T. S. Biro *et al.*, Phys. Lett. B **347**, 6 (1995).

[72] M. Bleicher *et al.*, J. Phys. G: Nucl, Part. Phy **25**, 1859 (1999).

[73] J. Sollfrank and U. Heinz, *Quark Gluon Plasma 2* (World Scientific, 1995).

[74] U. Heinz, J. Phys. G. **25**, 263 (1999).

[75] F. Mandl, *Statistical Physics* (John Wiley and Sons, 1988).

[76] J. Cleymans, Preprint nucl-th/9704046 (1997).

[77] J. Sollfrank, J. Phys. G: Nucl. Part. Phys **23**, 1903 (1997).

[78] J. Rafelski, Phys. Lett. B **262**, 333 (1991).

[79] F. Becattini *et al.*, Eur. Phys. J. C **5**, 143 (1998).

[80] F. Becattini *et al.*, Preprint hep-ph/0011322 (2000).

[81] F. Becattini and U. Heinz, Z. Phys. C **76**, 269 (1997).

[82] P. Braun-Munzinger *et al.*, Phys. Lett. B **465**, 15 (1999).

[83] J. Rafelski and J. Letessier, Preprint nucl-th/9903018 (1999).

[84] U. Heinz and M. Jacob, Preprint nucl-th/0002042 (2000).

[85] X. N. Wang, Phys. Rev. C **58**, 2321 (1998).

[86] J. Ashman *et al.*, Phys. Lett. B **206**, 364 (1988).

[87] J. W. Harris, in *Quantum Chromodynamics* (World Scientific, 1999).

[88] B. Back for the PHOBOS Collaboration, Nucl. Phys. A **661**, 690 (1999).

[89] J. Lajoie for the PHENIX Collaboration, J. Phys. G: Nucl. Part. Phys. **27**, 645 (2001).

[90] S. Afanasiev *et al*, (NA49 Collaboration), Nucl. Instrum. Meth. A **430**, 210 (1999).

[91] The STAR Collaboration, Conceptual Design Report for the Solenoidal Tracker at RHIC, LBL (unpublished) (1992).

[92] H. Wieman *et al*, (STAR Collaboration), IEEE Trans. Nucl. Sci. **44** 671 (1997).

[93] K. H. Ackermann *et al.*, Nucl. Phys. A. **661**, 681c (2001).

[94] S. Klein *et al.*, IEEE Transactions on Nuclear Science **43**, 1768 (1996).

[95] T. Alber *et al.* (NA49 Collaboration), Eur. Phys. J. A **2**, 383 (1998).

[96] K. Kleinknecht, *Detectors for Particle Radiation* (Cambridge University Press, 1998).

[97] R. Bock *et al.*, *Data Analysis Techniques in High Energy Physics Experiments* (Cambridge University Press, 1990).

[98] M. Calderon de la Barca Sánchez, PhD Thesis, Yale University (2001).

[99] R. Brun and F. Rademakers, Nucl. Inst. Meth. Phys. Res. (see also http://root.cern.ch) **A389**, 81 (1997).

[100] R. Brun *et al.*, GEANT user guide, CERN Report DD/EE/84-1 (1987).

[101] C. Adler *et al*, (STAR Collaboration), Phys. Rev. Lett. **87**, 112303 (2001).

[102] P. Koch, Z. Phys. C **38**, 269 (1988).

[103] I. G. Bearden *et al*, (The BRAHMS Collaboration), Phys. Rev. Lett. **87**, 112305 (2001).

[104] F. Antinori for the WA97 Collaboration, Nucl. Phys. A **661**, 130c (1999).

[105] J. R. Taylor, *An introduction to error analysis: the study of uncertainties in physical measurements* (Sausalito: University Science, 1997).

[106] J. Bartke *et al*, (NA35 Collaboration), Z. Phys. C **48**, 191 (1990).

[107] J. Castillo for the STAR Collaboration, Proceedings of SQM2001, (to be published in J. Phys. G) (2002).

[108] P. Braun-Munzinger *et al.*, Phys. Lett. B **518**, 41 (2001).

[109] W. Florkowski, W. Broniowski and M. Michalec, Preprint nucl-th/0106009 (2001).

[110] P. Braun-Munzinger *et al.*, Phys. Lett. B **465**, 15 (1999).

[111] P. Braun-Munzinger, Nucl. Phys. A **681**, 119c (2001).

[112] C. Adler *et al.* (STAR Collaboration), Phys. Rev. Lett. **86**, 447 (2001).

[113] C. Adler *et al.* (STAR Collaboration), to be submitted to Phys. Rev. Lett.

[114] M. Kaneta *et al.* (NA44 Collaboration), J Phys. G **23**, 1865 (1997).

[115] A. Bialas, Phys. Lett. B **442**, 429 (1998).

[116] I. Bearden *et al.* (NA44 Collaboration), Phys. Rev. Lett. **78**, 2080 (1997).

[117] S. V. Afanasiev *et al.*, (NA49 Collaboration), Phys. Lett. B **491**, 59 (2000).

[118] C. Adler *et al.* (STAR Collaboration), to be submitted to Phys. Rev. Lett.

[119] C. Adler *et al.* (STAR Collaboration), Phys. Rev. C **65**, 041901(R) (2002)

[120] C. Adler *et al.* (STAR Collaboration), Phys. Rev. Lett. **87**, 262302 (2001).

[121] P. Fachini for the STAR Collaboration, Proceedings of SQM2001, (to be published in J. Phys. G) (2002).

[122] P. Braun-Munzinger *et al.*, Preprint hep-ph/0106066 (2001).

[123] B. Back *et al*, (PHOBOS Collaboration), Phys. Rev. Lett. **87**, 102301 (2001).

[124] P. Levai, private communication (2001).

[125] G. Van.Buren. for the STAR Collaboration, Preprint nucl-ex/0201009 - Proceedings of SQM2001, (to be published in J. Phys. G) (2001).

[126] P. Levai. T. S.B̃iró and J. Zimányi, Preprint hep-ph/0112137 - proceedings of SQM2001, to be published in J. Phys. G (2001).

[127] J. Velkovska for the PHENIX Collaboration, Nucl. Phys. A **698**, 507 (2001).

[128] W. Broniowski and W. Florkowski, Preprint nucl-th/0106050 (2001).

[129] I. Vitev, M. Gyulassy, *et al.*, Preprint nucl-th/0104066 (2001).

[130] I. Vitev, M. Gyulassy, *et al.*, Preprint nucl-th/0108045, proceedings of INPC 2001 (2001).

[131] G. C. Rossi and G. Veneziano, Nucl. Phys. B **123**, 507 (1977).

[132] D. Kharzeev, Phys. Lett. B **378**, 238 (1996).

[133] M. Gyulassy. S. E. Vance and X. N. Wang, Phys. Lett. B **443**, 45 (1998).

[134] K. Adcox *et al.* (PHENIX Collaboration), Preprint nucl-th/0109003 (2001).

[135] X. N. Wang, Phys. Rev. Lett. **81**, 2655 (1998).

[136] S. Pandey for the STAR Collaboration, Nucl. Phys. A **661**, 686 (1999).

[137] A. Morsch and H. H. Gutbrod for the ALICE Collaboration, Prog. Part. Nucl. Phys. **42**, 345 (1999).

[138] P. Braun-Munzinger, Nucl. Phys. A **661**, 261 (1999).